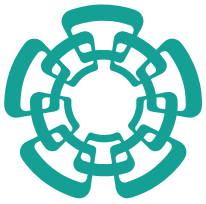

Centro de Investigación y de Estudios Avanzados
del Instituto Politécnico Nacional

Unidad Mérida

Departamento de Física Aplicada

Rotación espontánea en empaques de discos vibrados

Tesis que presenta

Gonzalo Gaudencio Peraza Mues

para obtener el Grado de

Doctor en Ciencias

en la Especialidad de

Física Teórica

Director de la Tesis

Dr. Cristian Fernando Moukarzel Rodríguez

Mérida, Yucatán, México **Noviembre de 2018**

B

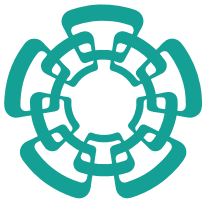

Centro de Investigación y de Estudios Avanzados
del Instituto Politécnico Nacional

Unidad Mérida

Departamento de Física Aplicada

Spontaneous rotation in vibrated disk packings

Tesis que presenta

Gonzalo Gaudencio Peraza Mues

para obtener el Grado de

Doctor en Ciencias

en la Especialidad de

Física Teórica

Director de la Tesis

Dr. Cristian Fernando Moukarzel Rodríguez

Mérida, Yucatán, México **Noviembre de 2018**

Acknowledgments

I would like to express my gratitude to everyone who made this thesis possible.

Foremost, thanks to Dr. Cristian F. Moukarzel, my thesis director, not only for guiding me through the writing of the thesis, but, also for his patience, motivation, and immense knowledge.

Beside my advisor I would like to thanks Dr. Osvaldo Carvente for providing space in his laboratory to perform all the experiments presented in this work, as well as for his guidance in performing such experiments.

Im also grateful with all personnel from CINVESTAV-Mérida for their assistance and support.

CGSTIC-CINVESTAV is gratefully thanked for the allotment of CPU time in "Cluster híbrido de supercómputo – Xiuhcoatl". In the same manner, I also thank the team in charge of cluster "Kukulkan" for technical support and CPU time.

Thanks to CONACYT for granting me a scholarship that allow me to study my PhD.

Last but not the least, I would like to thank my family: my parents, my brother and sister, and my wife for supporting me spiritually throughout writing this thesis and my life in general.

Abstract

Under specific conditions, gently vibrated packings of frictional elastic disks self-organize onto a rotationally persistent state. In this state, most disks display a statistical tendency to rotate in a direction determined by the local contact network of each disk inside the packing.

In the present thesis, this rotational state is characterized in great detail experimentally, numerically, and analytically. Data collected from extensive numerical simulations and laboratory experiments were used to study the statistical properties of rotation in disk packings.

Additionally, by analyzing the simplest setup, consisting of a single disk supported by two contacts under gravity, we are able to show in which way the randomness in the orientation of contacts is responsible for the tendency to rotate in large packings. We also distinguish two different rotation regimes with different dynamics: (1) a regime where the disk never looses contact with the supports, and (2) a regime where the disk bounces of the supports.

Analytic predictions are obtained for the rotational velocity of one disk in both regimes, and these are successfully compared against numerical results.

Resumen

Reportamos que, en determinadas condiciones de vibración suave, un empaque de discos elásticos con fricción presenta un estado rotacional auto-organizado, en el cual los discos rotan sistemáticamente en una dirección determinada por la configuración de contactos local de cada disco dentro del empaque.

En esta tesis se caracteriza experimental, numérica y analíticamente este fenómeno de manera detallada. Utilizando datos recolectados de un gran número de simulaciones númericas y experimentos de laboratorio, hemos estudiado las propiedades estadísticas de la rotación en empaques de discos.

Adicionalmente, analizando la configuración más simple, que consta de un disco sostenido contra la gravedad por dos contactos, es posible entender de qué manera la tendencia estadística a rotar en un dado sentido se deriva del desorden en la orientación de los contactos

en un empaque. Se distinguen, también, dos regímenes de rotación con características muy distintas: (1) un regimen donde el disco nunca pierde contacto con los soportes, y (2) un regimen donde el disco se encuentra rebotando sobre los soportes.

Se obtienen predicciones analíticas para la velocidad promedio de rotación de un disco como función de diversos parámetros físicos para ambos regímenes. Estas predicciones son comparadas satisfactoriamente con resultados numéricos.

Contents

1 Introduction

Materials composed of discrete interacting elements that are not subject to thermal fluctuations are called granular materials. Each element is called a grain. Each grain is big enough so that the energy involved in its displacement is several orders of magnitude that of its thermal energy. Examples of granular materials are sand, nuts, gravel, intergalactic dust clouds, etc.

Another distinct feature of granular materials is that interactions between grains dissipate energy, in contrast to molecular gases or liquids, where interactions are elastic. Energy is transferred to internal degrees of freedom every time grains collide or move against each other. Since thermal energy is unable to affect the motion of the grains, energy is lost at each interaction, from the dynamical point of view. This means that, to maintain a granular system in motion, energy needs to be constantly injected into the system, at a rate that compensates the rate of dissipation. As soon as the energy input is turned off, the system relaxes to a meta-stable state until the next perturbation shifts the system to a new configuration. Dissipation also introduces correlations between colliding particles, that lead to violation of the assumption of molecular chaos. It can happen, then, that these correlations trigger the appearance of ordered structures and patters. Granular materials are, thus, systems out of equilibrium and, as such, exhibit rich dynamical behavior.

One way to provide the necessary energy to keep grains in motion is to vibrate a container filled with such grains. Vibrated granular matter displays a range of self-organizing phenomena such as clustering, pattern formation, segregation and convection. Some of these phenomena are qualitatively described in the next section. We refer the reader to reviews by Aranson and Tsimring [1], Kudrolli [2], and references therein, for a more exhaustive treatment.

1.1 Self organization in vibrated granular media

Figure 1.1 shows a vertically vibrating monolayer of grains. Vibration leads to a phase separation in which a solid cluster of static grains coexists with a gas like phase of rapid moving particles [3]. This clustering resembles that of a freely cooling gas of inelastic particles first described by Goldhirsch and Zanetti [4], the difference being that in the vibrated monolayer, energy is constantly being provided into the system, so we are dealing with a steady-state stable pattern.

In both a freely cooling granular gas and a vibrated monolayer, clustering is caused by dissipation from inelastic collisions. While energy dissipation considerations are enough to understand clustering in a cooling gas, to maintain the phase separation in the vibrated layer, where energy is being constantly renewed, additional mechanisms are needed. In a vibrated layer, transfer of momentum from the plate to the horizontal motion of the particles is inhibited in both the cluster and the dilute gas. In the cluster, the particles are restricted to move in the horizontal direction by their neighbors, while in the gas, the low frequency of collision also restricts the transfer of momentum.

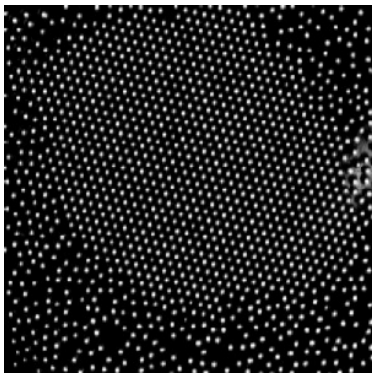

Figure 1.1: Top view of a vibrated monolayer of monodisperse granular layer of 1 mm steel balls. A dense cluster of immobile particles surrounded by a gas of moving particles. From Olafsen and Urbach [3].

Depending on the intensity of the vibrations, vibrated granular matter can behave similarly to liquids and gases. Vibrated granular matter that behaves fluid-like is said to be vibro-fluidized, and may display a range of collective behavior that is typically associated with fluids, like convection, shear flow, and surface waves. The specific dynamics depend

on the nature and intensity of the vibration, the shape of the container, and the mechanical properties of the constituent grains.

Vibrofluidized multilayers of 10 to 30 particle diameters can display many different patterns due to surface waves (Figure 1.2). The pattern that appears depends on the amplitude and frequency of vibration, shapes and sizes of the grains, shape of the container, number of layers, etc. [5, 6] Event-Driven simulations are able to reproduce most of the patterns observed experimentally, but only when friction is taken into account [7, 8].

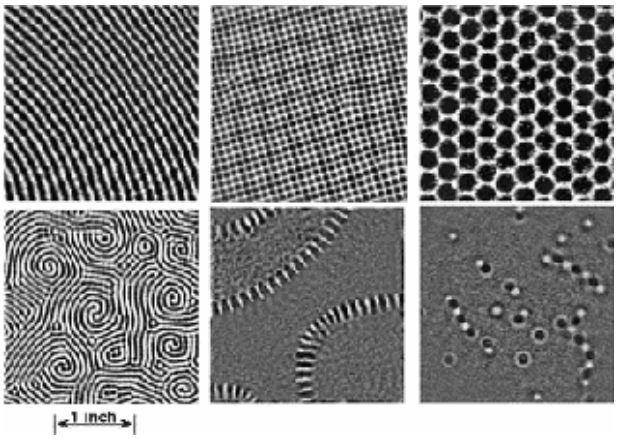

Figure 1.2: Different patterns that can appear due to surface waves in vibrated granular layers.

The last square of Figure 1.2 shows the appearance of oscillons, localized oscillations in a granular bed. Oscillons can interact with each other and appear only for specific values of the coefficient of restitution [9]. A single oscillon is depicted in Figure 1.3.

So far we have discussed granular matter composed of identical grains. As soon as one can differentiate between two or more species of grains, one of the most striking phenomena in vibrated granular matter can occur: segregation. If grain species differ in size, roughness, density, etc, species tend to segregate instead of mixing.

Size segregation occurs when species of grains of different sizes separate, as shown in Figure 1.4 (a). Rosato et al [11] proposed a geometric mechanism for size segregation in vibrated granular media in which voids, left by large particles when moving upwards, get filled by smaller particles. They employed a Monte Carlo simulations to show that a void filling mechanism leads to larger particles being on top. This type of segregation is called

Figure 1.3: Oscillon, a localized vibration in vibrated granular matter. From Umbanhowat et al [9].

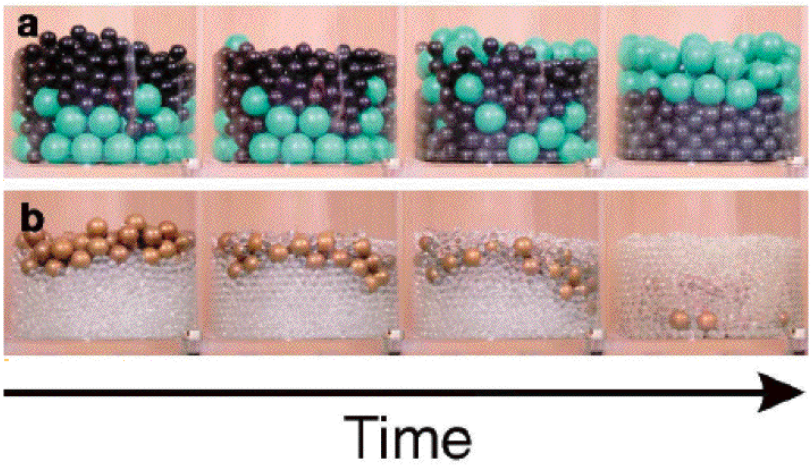

Figure 1.4: (a) 8 mm glass beads on top of 15 mm polypropylene, which show the classical Brazil nut effect (b) 10 mm bronze spheres on 4 mm glass beads showing the reverse Brazil nut effect. From Breu et al. [10]

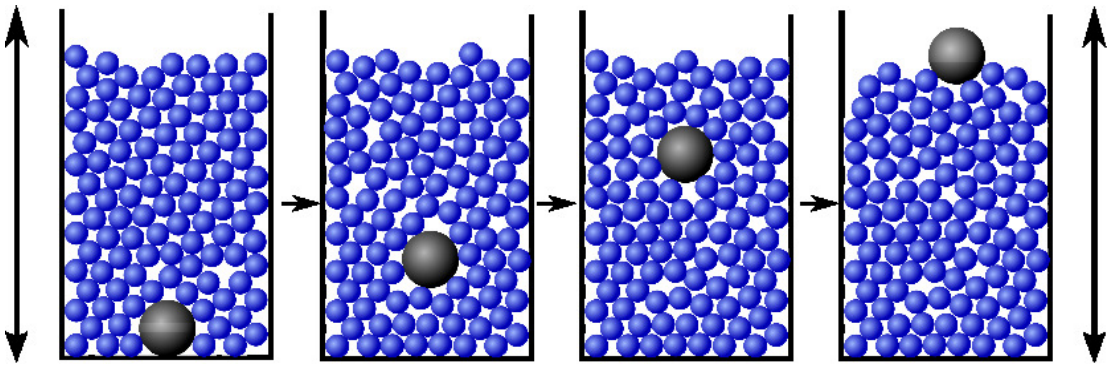

Figure 1.5: The Brazil-nut effect. Image from Wikipedia.

the Brazil-nut effect, and is often demonstrated by having a single large particle rise to the top in a container filled with smaller ones (see Figure 1.5).

A reverse segregation, where large particles sink to the bottom, has also been identified, and deemed the reverse Brazil-nut effect [10, 12] (Figure 1.4 (b)). If the diameter ratio is smaller than the inverse of the density ratio, the particle mixture should show the Brazil-nut effect, but if the diameter ratio is larger than the inverse of the density ratio, the particle mixtures should show the reverse Brazil nut effect.

Convection is also a segregation mechanism in granular media. When vibrated, the interaction of the grains with the side walls can induce convection currents whose direction depends on the shape of the container [13], see Figure 1.6. Grossman [14] found that the direction of the convective roll depended on when the peak in density occurred in relation to the velocity of the side walls, which in turn was influenced by the angle of inclination of the side walls. When particles are more compressed, the friction from the contact with the side walls increases, while it decreases when the particle density lowers. In a cylindrical container, when the container moves up, particles compress and the ones near the wall stick to it while the center particles keep moving upward, this creates a void in the bottom of the container that is subsequently filled by the side particles. Knight et al. [15] found that convection of the grains influences the motion of the large particle in the Brazil-nut effect and reverse Brazil-nut effect.

Shinbrot argues that many features of pattern formation in granular matter can be understood by considering only two mechanisms; chaotic scattering due the convex surface

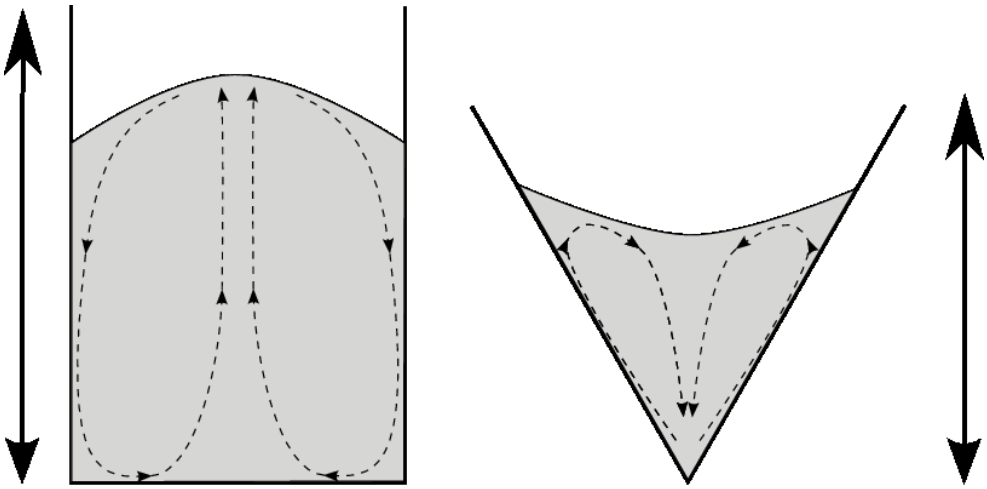

Figure 1.6: Granular convection in vibrated granular matter. A cylindrical container (left) induces a type of convection where grains move upward through the center and downward at the sides. A conic container (right) reverses the convection current. Image from Wikipedia.

of the grains, and energy dissipation due to inelastic collisions [16]. Let's see how a stripe pattern can appear in a vibrated granular monolayer. In Figure 1.7 (a) at $t = 0$ grains are arranged in stripes. A strike from the bottom plate will make them scatter in random directions. Collision in the direction parallel to the stripes will quickly dissipate gained momentum and the particles will move mainly in a perpendicular direction. At about half distance they will collide with particles from neighboring stripes, dissipate their kinetic energy and form new stripes. This process then repeats periodically. A similar argument holds for square patterns as those in Figure 1.7 (b).

1.2 Simulation techniques for vibrated granular media

Simulation techniques have proven an invaluable tool in the study of granular matter, for which a comprehensive analytic theory does not yet exist. By setting up numerical experiments in the computer, which reproduce experimental findings, one can isolate and identify the importance of the different parameters that influence the outcome. In this thesis we have used two different numerical algorithms to study 2D granular packings:

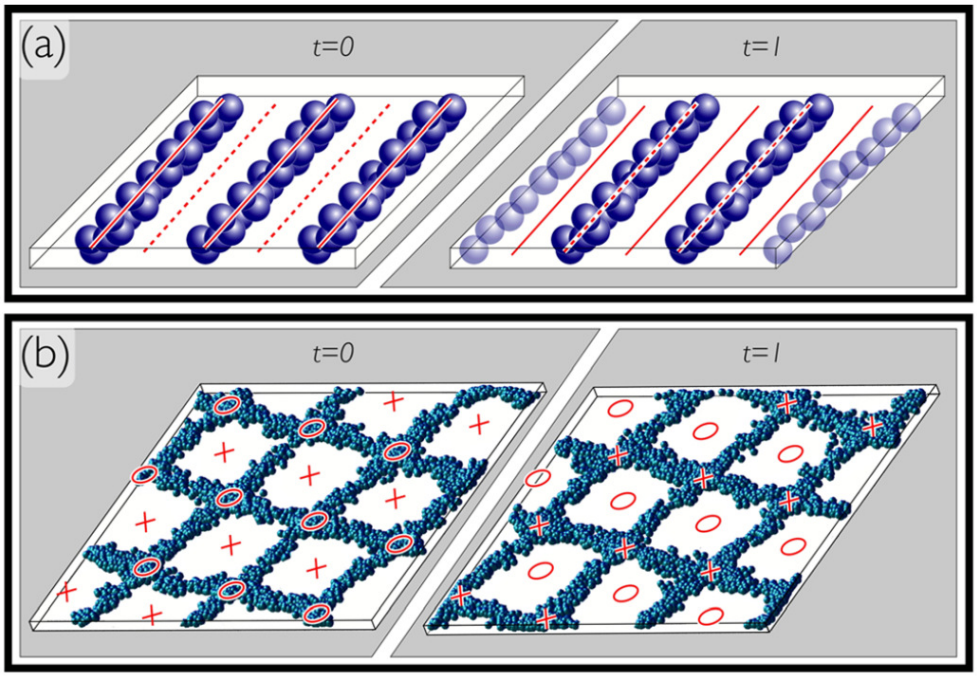

Figure 1.7: Illustration of the fact that combining chaotic scattering with inelastic collisions can lead to pattern formation. (a) Initially parallel lines of particles ($t = 0$; particles aligned with solid red lines) struck from below so that they chaotically scatter outward will collide inellastically with one another to produce new lines ($t = 1$: particles now aligned with broken red lines). If they then are again struck from below, the cycle will repeat to reinforce the parallel line state. (b) Similarly, square arrays of particles that scatter outward ($t = 0$: square centers at x's, vertices at o's) will collide to produce a new array ($t = 1$: centers and vertices have changed places). From Shinbrot [16].

Molecular Dynamics algorithms (MD), also called the Discrete Element Method (DEM) and Event-Driven (ED) algorithms. We will briefly review each of these methods in this section. A good introduction and review to the numerical simulation techniques for granular materials can be found in the book by Pöschel and Schwager [17]. There exist other methods, such as Monte Carlo simulations [11], cellular automaton algorithms [18] and the Contact-Dynamics method. These will not be discussed here [19].

1.2.1 Molecular Dynamics

Molecular Dynamics methods where originally developed to study interacting systems of many atoms or molecules. The dynamics of the system are determined by numerically solving Newton's equations of motion with forces between particles calculated from inter-particle potentials. Forces due to external potentials like gravity can also be included in the simulations. The methods where extended to deal with the particularities of granular matter, such as dissipative contact forces. MD simulations have helped to gain useful insight about the properties and mechanisms behind the behavior of static packings and dense granular flows, where contact forces cannot be modeled by instantaneous collisions.

In MD algorithms, grains are non-deformable, but are allowed to overlap. Contact forces are then determined from the overlap, this is, from the relative positions (and velocities) of particles in contact. Several force models have been proposed for the calculation of contact forces (see [20] for a review). One force model that yields accurate results despite its simplicity [21] is the linear-dashpot model. Here the interaction is modeled using a linear spring and a viscous dashpot, which reproduces an inelastic collision. The tangential interaction is additionally limited by the Coulomb friction force. The first ones to introduce this model for tangential forces in the context of granular matter simulations where Cundall and Strack [22]. The details of the implementation of the contact force model used in this thesis can be found in Chapter 4.

In MD methods, one must ensure that the collision is simulated accurately. This requires that the discretization time-step δt be much smaller than that typical duration of a collision. The linear-dashpot model predicts a collision time of approximately half the period of oscillation of the normal spring. This period decreases with particle stiffness. Realistic values of stiffness require time-steps δt shorter than $\sim 10^{-6}$ s [21]. This makes computation

CPU expensive unless softer particles are used, but reducing particle stiffness sometimes alters the dynamical behavior of the system [23].

1.2.2 Event-Driven simulations

Event-Driven simulations are efficient in the dilute gas regime. In this regime the grains are agitated, collisions are infrequent and of short duration in comparison with the mean flight time of a grain. Each collision can then be approximated as instantaneous [24]. The positions and velocities before the collision are mapped to new values after the collision following a set of rules. Collision rules depend on the coefficients of normal and tangential restitution (see Chapter 6). Between collisions, the trajectory of each grain can be calculated analytically, a calculation that is computationally fast.

The central idea behind this technique is to build a list of possible collisions calculating the times at which particle trajectories will intersect. One then chooses the collision (event) that will happen earlier, and advances all positions and velocities in the simulation to that point. New positions and velocities are calculated for the colliding pair of particles following the collision rules and the method is iterated again.

Computation times of simulations using Event-Driven algorithms can be several orders of magnitude shorter than those using the MD approach if the particle density, and thus the rate of collisions, is low. As the particle density increases, and the time between collisions shortens, the efficiency of the method is greatly reduced. For small values of the normal coefficient of restitution, dissipation can lead to clustering and an infinite number of collisions in finite time [25] effectively halting the simulation.

1.3 Rotation in disk packings

In this thesis we describe the observation of sustained rotations in vibrated two dimensional packings of disks. Disks in vibrated polydisperse packings will spontaneously start to rotate systematically, each in a given direction. This rotation was first observed numerically using Molecular Dynamics simulations of disks under gravity, with a careful implementation of tangential forces. An example of such packing is found in Figure 1.8. In the figure, each

disk is colored according to its direction of rotation: red for clockwise rotation and blue for anti-clockwise rotation. The packing is composed of 60 disks, 20 disks with a 3 cm diameter, 20 with a 4 cm diameter and 20 with a 5 cm diameter. A corresponding plot of the angular path each disk takes over time is found in the same figure. Each disk i rotates in a random direction with a random mean rotational velocity $\bar{\omega}_i$. The rotational velocity $\bar{\omega}$ depends on the local configuration of contacts of each disk, and changes if the packing structure changes. The same packings are also simulated using Event-Driven algorithms (Figure 1.9).

The bottom of the container is vibrated sinusoidally with a defined amplitude A_b and frequency ω_b. Perturbations are then propagated throughout the packing via contact forces between disks. Vibration must be strong enough to allow contacts between disks to overcome tangential friction forces and slide, and/or to allow contacts to open and close repeatedly. At the same time, vibration must not be so strong as to lead to excessive reorganization of the packing, since such reorganization will change the local arrangements of contacts of each disk. Since the rotational velocity depends strongly on this contact network, an unstable packing will lead to fluctuating velocities of near zero mean.

A careful analysis of the MD simulations showed a transition between two dynamical regimes as the amplitude of the vibration A_b increases. This transition is reflected in the functional dependence of the mean squared rotational velocity $\langle\bar{\omega}^2\rangle$ on the amplitude of vibration, $\langle\bar{\omega}^2\rangle$ being the average of individual disk velocities $\bar{\omega}^2$ over an ensemble of simulated packings. Over a certain amplitude threshold, $\langle\bar{\omega}^2\rangle$ transitions from growing proportionally A_b^4 to a linear growth in A_b. It is shown in Chapter 3 that, at this transition, the system goes from a state dominated by persistent contacts, to a state dominated by disk collisions. ED simulations are well suited in the regime of frequent collisions, and, since they avoid step by step integration, display better performance than MD simulations. Given that they exclude the possibility of lasting contacts, they allow the study of the contribution of collisions to rotation without the influence of permanent contacts among disks. Details of the implementation of MD and ED simulations are given in Chapter 2.

To be sure that this self-organized rotational response is real, and not just an artifact of the simulations, we performed several laboratory experiments with real packings. The phenomenon of sustained rotation was observed for disks of different materials and sizes.

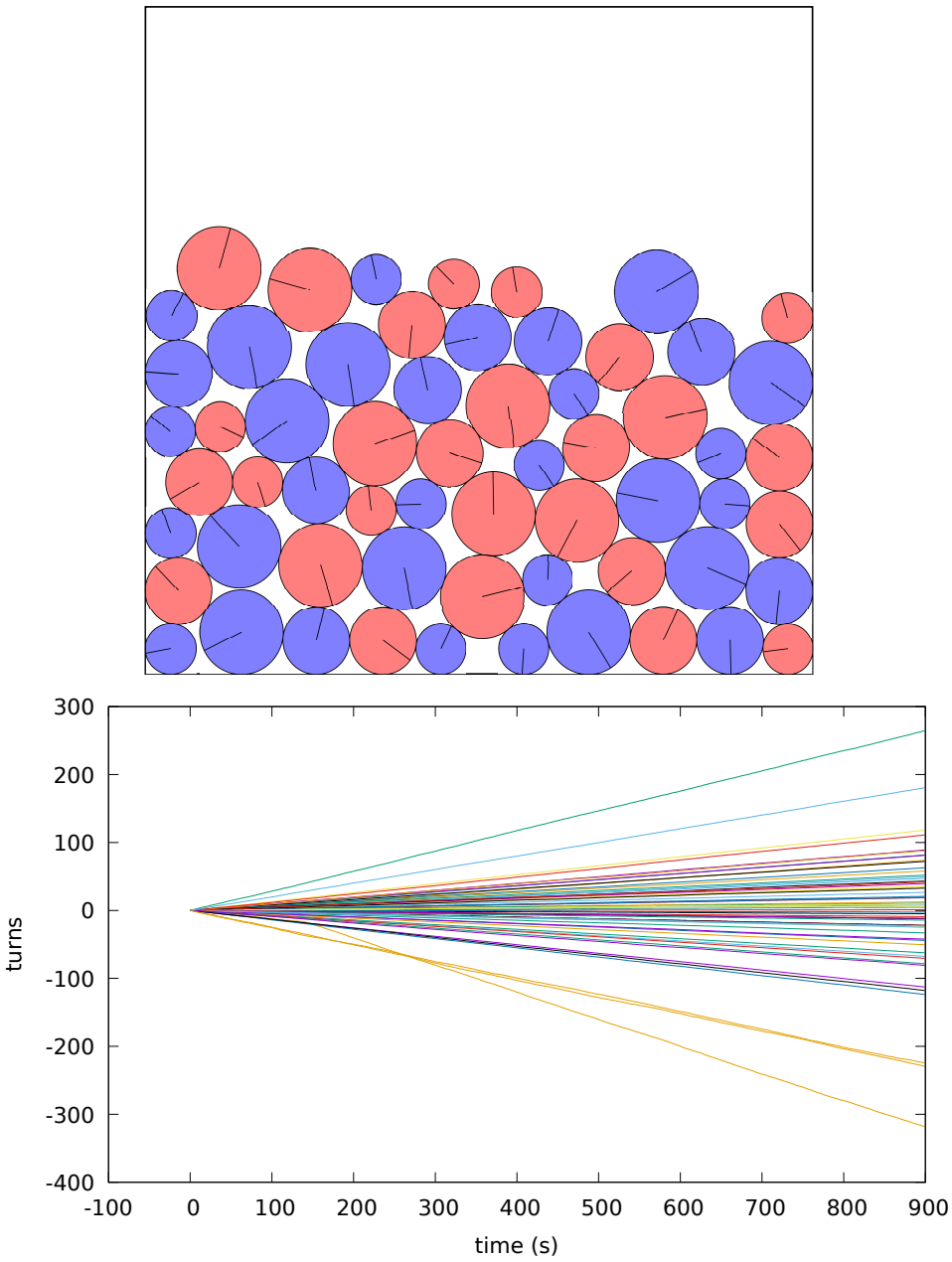

Figure 1.8: Top: A typical two dimensional packing of disks under gravity inside a rectangular container. This packing was studied using time driven Molecular Dynamics simulations. Upon vibration of the bottom wall, spontaneous rotations of the disks are observed. Blue disks are rotating counter-clockwise, red disks are rotating clockwise. Bottom: Angular paths described by the disks of the packing.

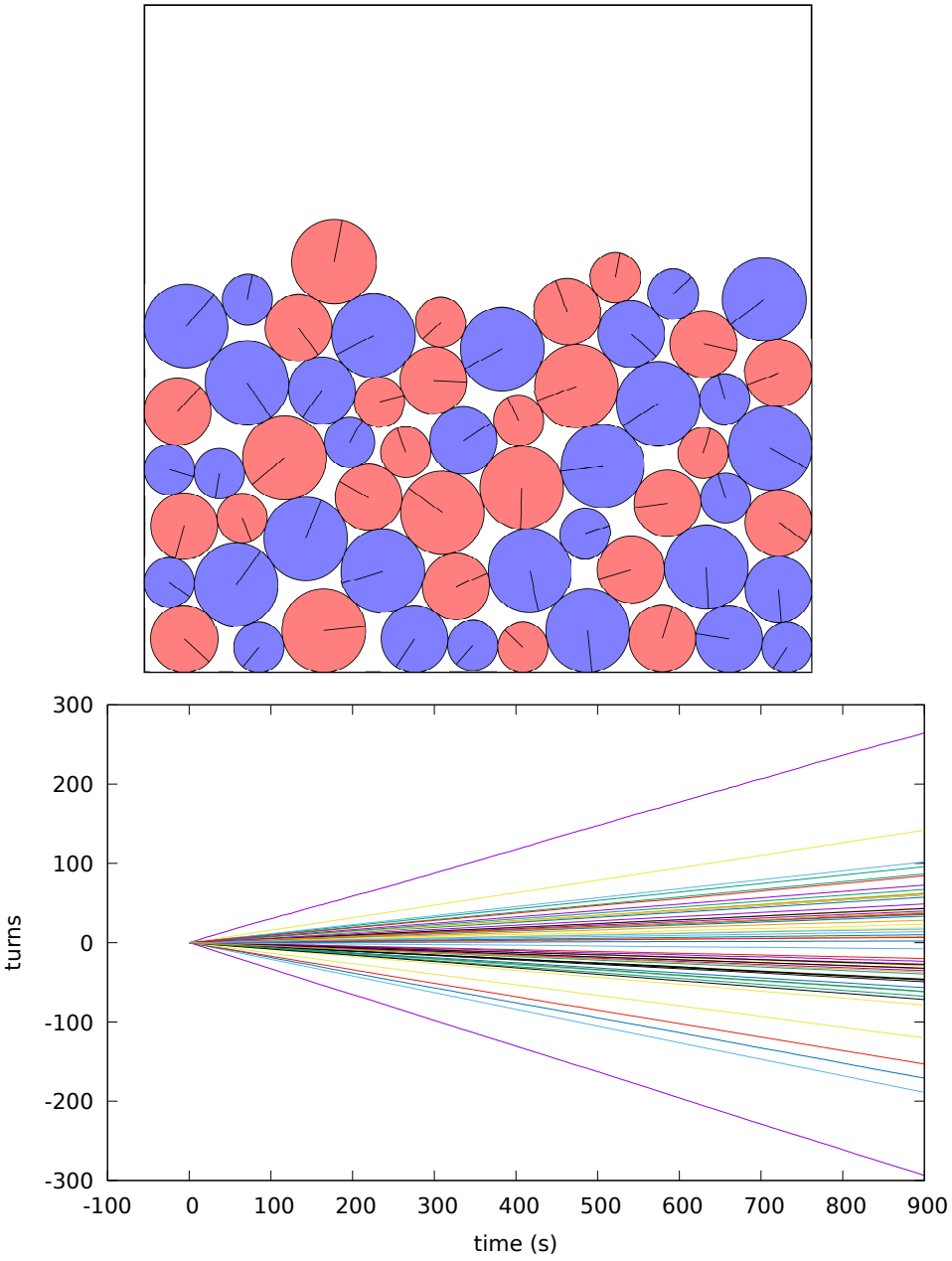

Figure 1.9: Top: The same aggregate as in Figure 1.8 studied using Event-Driven simulations. The difference in packing structure is due to reorganization of contacts during the simulation. Blue disks are rotating counter-clockwise, red disks are rotating clockwise. Bottom: Angular paths described by the disks of the packing.

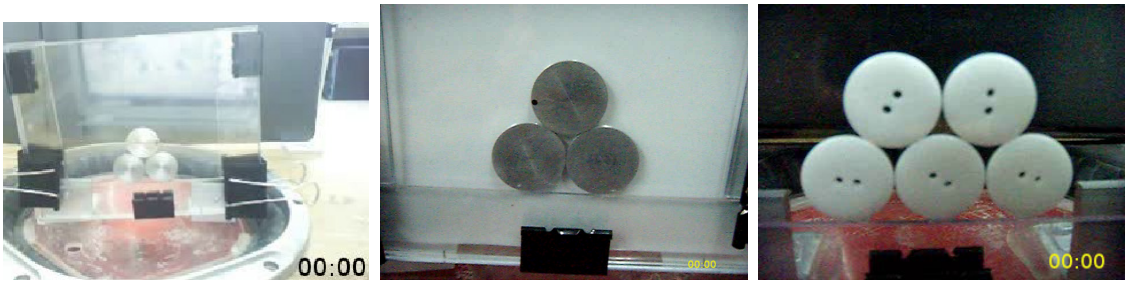

Figure 1.10: Three simple experiments that show sustained rotation under vibration. Left: A minimal 3 disk packing of thin aluminum disks tilted in order to introduce asymmetry. Middle: A minimal 3 disk packing of 1 cm thick steel disks, also tilted. Right: A small packing of plastic buttons. In all three setups disks of the bottom row are fixed.

Figure 1.10 shows three different small packings made with 1) thin disks of aluminum, 2) thick disks of steel, and 3) plastic buttons. In all three cases the packing was encased between two sheets of acrylic and attached to a loudspeaker that supplied the vibration. In these 3-disk systems, tilting the setup introduces the required asymmetry for rotation, as discussed later in this section. The button packings are already asymmetric for zero tilt since top buttons have a single neighbor on the top layer.

A much better crafted set of experiments was made for packings with the same radii distribution used in numerical simulations. 60 disks made from 3 mm acrylic sheets where encased between two sheets of tempered glass. Special markings were made on each disk to track rotations using a camera. The bottom wall of the container is able to move, and is attached to a loudspeaker that drives the wall in a piston-like manner. A snapshot from one of these experiments is shown in Figure 1.11 top. The angular paths of each disk are plotted in the same figure, bottom. We can appreciate that the qualitative behavior is similar to the packings simulated using both MD and ED algorithms. A detailed analysis of numerical and experimental results is presented in Chapter 3, while a description of the experimental setup is given in Chapter 2.

The fact that these rotations have never been reported in the literature, despite numerical and experimental studies with vibrated granular being common, may be due the narrow limit of excitation intensity required for stable dense packings, coupled to the computational cost of a careful implementation of the frictional forces in numerical simulations.

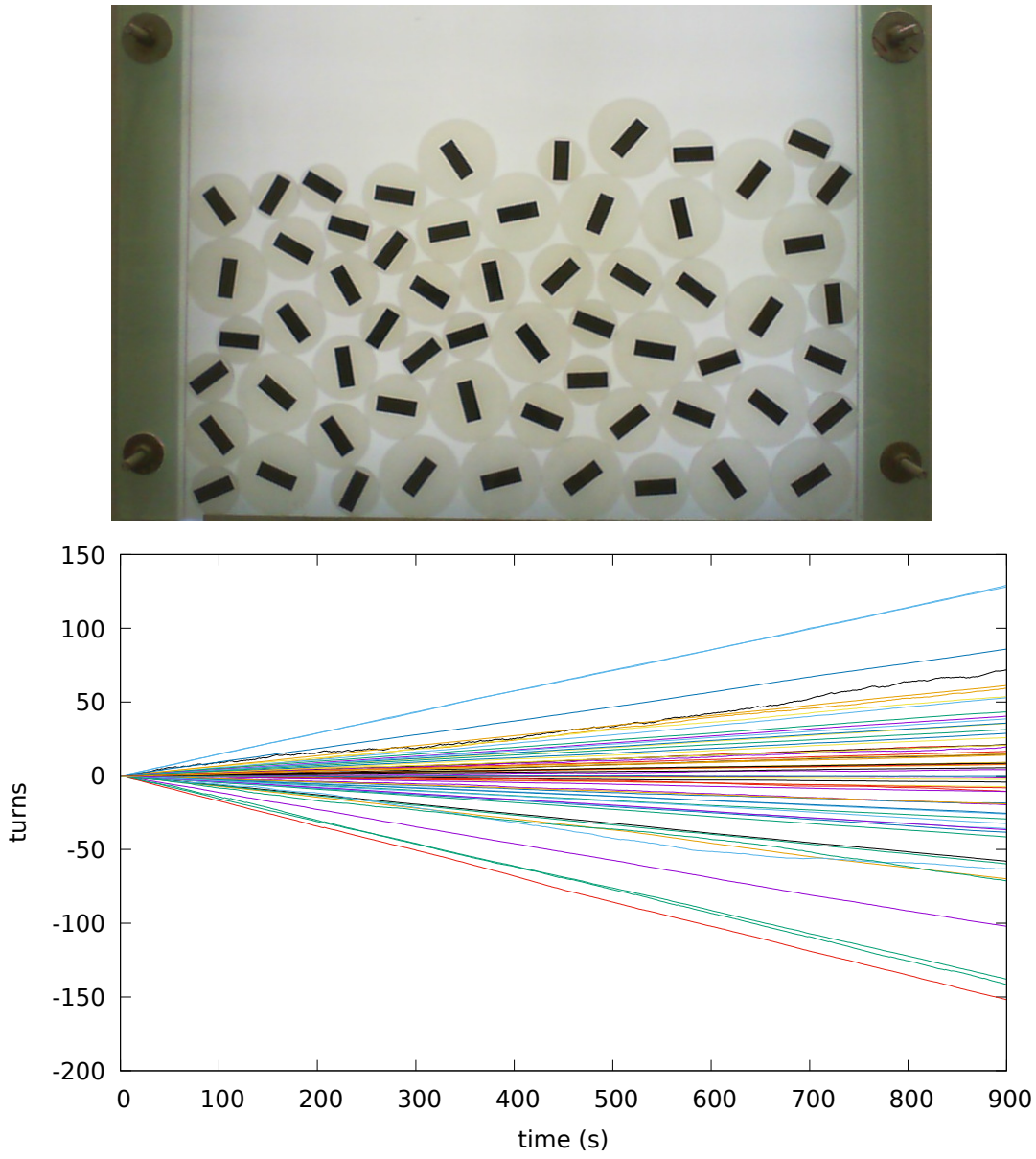

Figure 1.11: Top: Snapshot of an experiment of a 2D packing under similar conditions as the simulated packing from Figure 1.8. Bottom: Angular paths described by the disks of the packing.

Friction forces in simulations are usually taken into account at most approximately. Most such programs are usually oriented towards following the collisional dynamics of particles that only come into contact sporadically, or else because these are in a regime of complete repose, where friction forces are constant. In the regime we are analyzing, disks are most of the time in contact with each other, but the total kinetic energy is large enough to allow for the systematic breaking of frictional constraints. Therefore, a careful implementation of friction is important to accurately reproduce the rotational response of the packing.

A sinusoidally vibrating bottom is implemented numerically because such setup is the simplest to reproduce experimentally in the laboratory. This allows for a better comparison between numerical and experimental results. Although most of the results presented in this thesis were obtained using a sinusoidally vibrating bottom, the onset of rotation is not restricted to this type of excitation. In fact, many different types of vibration were also implemented in numerical simulations. For example, a layer of bottom disks are set to vibrate randomly around their equilibrium positions, their center restricted to move inside a circle of radius ϵ. Rotation under this type of excitation was qualitatively similar to that of the case of a sinusoidally driven bottom. We can say, then, that, in general, a noisy input is being rectified. The system is self organizing in a way that it responds to random vibrational motion by generating a persistent rotation for each disk.

Clearly, a necessary ingredient for the appearance of sustained rotation is the breakdown of reflection symmetry. While the statistical properties of the whole packing must necessarily be symmetric under reflections, those of a single disk need not be. In a disordered packing the local configuration of contacts for each disk is random. This disordered contact network, that is persistent over long timescales, allows for rotation. Because of the statistical reflection symmetry of the packing, the distribution of rotational velocities over all disks must necessarily be symmetric and of zero mean, something that was experimentally and numerically verified.

As a first step towards understanding the possible microscopic origins of the rotational organization described above, we also performed numerical and analytic analysis on a simpler arrangement, or toy model, for which some mechanisms for rotation can be readily determined. The minimal setup to study spontaneous rotation consists of three disks of the same radius R, as shown in Figure 1.10, left and center. The setup consists of one

upper disk supported against gravity by two vibrating "supporting" disks.

This simple arrangement is described in detail in Chapter 4 and studied experimentally and numerically in Chapters 5 and 6. It is found that, when subjecting the supporting disks to vibration, the upper disk rotates steadily if the whole system is tilted, i.e. if the left-right symmetry is broken. We can distinguish the same two states observed in large packings in the 3 disk packing. For mild vibration, contacts between disks are never broken, but the upper disk rotates steadily without ever loosing contacts with its supports, because frictional forces saturate and sliding occurs. This regime is studied in detail in Chapter 5. The high vibration intensity regime, where the upper disk is bouncing on top of the supports, is dominated by binary collisions, and is studied in Chapter 6. The analysis of a 3-disk packing in the bouncing regime was also discussed in [26].

2 Methods and Tools

We have performed numerical simulation using tree different algorithms, namely: (1) Time Driven Molecular Dynamics (also called the Discrete Element Method in the context of granular media simulations), (2) Event-Driven Dynamics, and (3) a Discrete Map. The first two algorithms were used to simulate packings of disks, while the map was developed to simulate a disk on a wedge, a simple system that also displays rotation. The map is equivalent to an Event-Driven simulation, where the equations describing the change of variables between collisions can be calculated analytically.

In the following sections we describe the implementation of each algorithm, justify its usage, and explain within which approximations each algorithm is applicable. We also describe the experimental procedure and apparatus used in the experiments with real packings.

2.1 Packing initialization

A problem in all simulations of dense granular media is that of generating a suitable starting condition for the simulation. A simple approach is to place particles one by one at random positions. When a newly inserted particle overlaps one or more previously placed particles, the placement is rejected and a new attempt is made with a new random position. The simulation is then allowed to evolve to a stable configuration before starting to record data.

While simple to implement, this approach has several disadvantages. If an attempt is made to generate a dense packing, the rejection rate will be very high, greatly increasing the time required to generate a packing. If the size of the available space is increased in order to decrease density, it may take the simulation a lot of time to reach a stable configuration.

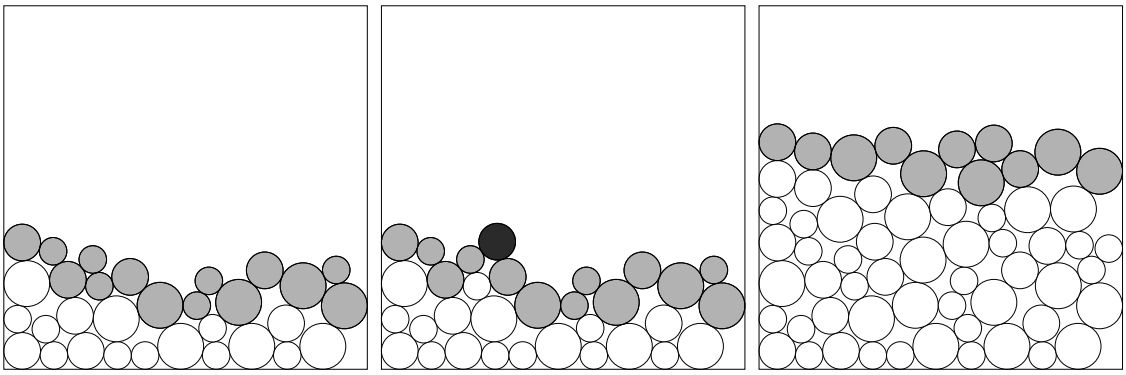

Figure 2.1: This figure illustrates the advancing front algorithm to construct disk packings. On the left, the current front is colored in gray. On the middle, a new disk is placed (dark) and the front is updated. On the right, a complete 60 disks packing is shown.

To avoid such problems, we have implemented the advancing front algorithm described in [27] to fill a rectangular container with disks. In this algorithm, the advancing front is defined to be the top layer of disks plus the walls. The packing is built incrementally, by placing a new disk such that it touches exactly two elements of the front without overlapping any other previously placed disk. The front is then updated to include the new disk and to remove disks no longer in the top layer. This process is iterated until all disks have been placed. The front is advancing in the sense that it moves towards the top as the container is filled with disks. A disk placement step is illustrated in figure 2.1.

2.1.1 Advancing front packing construction

To place a new disk i on top of two disks, a and b, on the front, the following constraints must hold for the (x, y) coordinates of disks' centers.

$$(x_i - x_a)^2 + (y_i - y_a)^2 = R_{ia}^2, \tag{2.1}$$

$$(x_i - x_b)^2 + (y_i - y_b)^2 = R_{ib}^2. \tag{2.2}$$

Where R_{ij} is the sum of the radii of disks i and j, $R_{ij} = R_i + R_j$.

This system of equations has two solutions for the coordinates (x_i, y_i) of the new disk.

One solution places the disk in the bulk of the packing, the other, places the disk at the top. We are only interested in the later, the solution being

$$x_i - x_a = \frac{1}{2L^2}\left[(L^2 + R_{ia}^2 - R_{ib}^2)(x_b - x_a) - \sqrt{\left[L^2 - (R_{ia} - R_{ib})^2\right]\left[(R_{ia} + R_{ib})^2 - L^2\right]}(y_b - y_a)\right], \tag{2.3}$$

$$y_i - y_a = \frac{1}{2L^2}\left[(L^2 + R_{ia}^2 - R_{ib}^2)(y_b - y_a) + \sqrt{\left[L^2 - (R_{ia} - R_{ib})^2\right]\left[(R_{ia} + R_{ib})^2 - L^2\right]}(x_b - x_a)\right], \tag{2.4}$$

where $L = \sqrt{(x_a - x_b)^2 + (y_a - y_b)^2}$ is the distance between the centers of disks a and b.

If the portion of the front where we are trying to place disk i contains a wall w and a disk d, then the solution becomes

$$x_i - x_d = (n_x\Delta x + n_y\Delta y + R_i)n_x \mp \sqrt{R_{id}^2 - (R_i + n_x\Delta x + n_y\Delta y)^2}n_y, \tag{2.5}$$

$$y_i - y_d = (n_x\Delta x + n_y\Delta y + R_i)n_y \pm \sqrt{R_{id}^2 - (R_i + n_x\Delta x + n_y\Delta y)^2}n_x, \tag{2.6}$$

where $\Delta x = x_w - x_d$ and $\Delta y = y_w - y_d$. n_x and n_y are the components of the normal versor to the wall. Since the container walls are either vertical or horizontal, n_x and n_y cannot be non zero at the same time. For the bottom wall, $n_y = 1$ and $n_x = 0$. For the left wall, $n_y = 0$ and $n_x = 1$. For right wall, $n_y = 0$ and $n_x = -1$.

Once built, the packing is used as the initial condition for the MD and ED algorithms described next.

2.2 Molecular Dynamics Simulations

Also called the Discrete Element Method, a Molecular Dynamics (MD) simulation considers each particle as a discrete entity, and integrates the equations of motion of the system using small time steps δt.

Each particle is affected by external forces imposed on the system, such as gravity, and

by the forces exerted on it by its interaction with other particles, and walls, if present.

In our MD simulations, the entire packing rests under gravity inside a rectangular container. The walls of the container are treated as special particles. Walls can be fixed or can be made to move in a certain way, independently of the forces exerted on them.

Whenever two disks are in contact, i.e. whenever their inter-center distance is smaller than the sum of their radii, inter-particle forces may appear at the contact point: a repulsive normal force along the line that joins their centers, and a tangential force perpendicular to it. Normal forces are always repulsive, and they are assumed to depend linearly on the amount of overlap. In other words, we assume a linear elastic interaction among disks in the normal direction.

Tangential forces are implemented by assuming that each disk has a linear-elastic "skin" that deforms whenever two disks in contact rotate relative to each other [22]. The ensuing tangential force is assumed to be proportional to the deformation of the skin and to a tangential stiffness k_t. In other words, we assume linear elasticity for tangential interactions as well. Tangential friction forces are limited by normal forces in the same contact via a friction coefficient μ and through Amonton's condition. Amonton's condition states that the magnitude of the tangential force cannot exceed μ times the normal force at the contact. When this limit is reached, tangential forces remain constant at the value given by it, even if the disks continue to rotate. This amounts to a "slip" of the elastic skin. Inter particle forces, and their implementations, are further discussed in grater detail in Chapter 4.

In addition to normal and tangential elastic forces, disks in contact are also subject to viscous forces. Viscous forces serve the purpose of representing, in a simplified manner, several dissipative processes occurring in real systems. A force proportional to the relative velocity of the disks in contact accounts for the energy lost in deformation of real colliding disks. Bulk viscosity, whereby a force acts on the center of a moving particle, proportional to its absolute velocity, accounts for viscous drag caused by the surrounding fluid, typically air. The details of these forces follow standard practices in molecular simulations [28], and will not be discussed here.

A fifth-order predictor-corrector algorithm [29] integrates Newton's equations of motion in discrete time steps δt. The time-step for integration was set to $\delta t = 10^{-6}$ s. Run times were usually of $t = 10^3$ s, i.e., 10^9 integration steps. For the normal force stiffness k_n, and

the skin stiffness k_t, we explored values ranging from 10^4 to 10^6. Bulk viscosity was set to zero since tests showed that its effect on the dynamics was negligible. Deformation viscosity was set to $\gamma_c = 10$. Gravity was set to the standard value $g = 9.8$ m/s^2. Parameter values where chosen to try to approximate the mechanical behavior of the acrylic disks used in the experiments.

Large values of the stiffness constants cause disks in the packing to experience fast oscillations. For dense packings, depending on the strength of excitation, disks may oscillate while maintaining contact with their neighbors, or rattle in place, colliding with near disks. For the integration algorithm to be able accurately approximate the dynamics, the value of the time-step δt must be much smaller than the typical period the oscillations disks experience. The relevant timescale can be approximated using the normal modes of oscillation of a single disk on top of two others. This timescale is also applicable to binary collisions, since, under the linear-dashpot model, the duration of a collision is approximately half the period of a normal oscillation of this type. The time-step was set to be at least smaller than one hundredth of this period, hence the value $\delta t = 10^{-6}$ s.

Energy flows constantly into the packing through the motion of the bottom wall of the container. The bottom wall is imposed to move vertically following a sine function with frequency f_b and amplitude A_b. The frequency was set to $f_b = 80$ Hz to match the frequency used in the experiments with real packings. The control parameter for the vibration is the dimensionless acceleration of the bottom wall $\Gamma = A_b(2\pi f_b)^2/g$, which measures the ratio of the peak acceleration of the bottom wall $A_b(2\pi f_b)^2$ to the gravitational acceleration g.

2.3 Event-Driven Simulations

An algorithm is said to be Event-Driven (ED) when the time in the system advances from one collision event to the next, instead of advancing in fixed time increments. Between events, the solution to the equations of motion for all particles can be given analytically, such as free linear motion or parabolic flight in a gravitational field. At an event, the velocities and positions of the particles change discontinuously, and have to be calculated from a set of rules that depend on the state of the system at the moment at which the event takes place. Events are idealized processes, taken to be instantaneous, such as collisions

between particles.

Event-Driven simulations are justified in the regime where the duration of a collision is much shorter than the mean flight-time of a particle. Under such conditions, collisions can be approximated as instantaneous events. The state of the system is given by the values of all positions and velocities for the disks in the packing. For a particular state, the time until the next collision is analytically calculated from the equations of motion for a particle in a constant gravitational field. Positions and velocities are then updated up to this time using the solutions to this same equations of motion. The velocities of the colliding pair of particles are then changed according to the collision rule derived in Section 2.3.1. The time for the next collision is again calculated and the process is repeated.

It is important to remember that, in ED simulations, interactions among particles are always through instantaneous collisions between pairs of disks. Only one such collision can take place at any given time. Collisions that involve more than two disks are impossible, as are persistent contacts. This makes ED simulations unsuited to study static packings, or packings experiencing quasi static deformation.

We have implemented most of the ED algorithm for disk packings following standard practices [17]. The important details of our implementation are: the derivation of the collision rules (Section 2.3.1), the calculation of collision times (Section 2.3.2), and the implementation of an energy exchange mechanism with the oscillating bottom wall (Section 2.3.3). Details of the implementation of an ED simulation, as well as the discussion of several techniques to improve simulation time, can be obtained in [17] and references therein.

2.3.1 Collision rules

A collision rule specifies how velocities change as a result of a collision. It can be derived analytically by integrating the equations of motion during a collision. By employing a collision rule, there is no need to simulate the dynamics during a collision, instead we just calculate the velocities after the collision from the velocities of the disks at the beginning of the collision.

To obtain the collision rule, we have assumed that normal forces act independently of tangential forces, changes in the normal velocities of colliding disks do not depend on

the tangential velocities. Independence of the dynamics in the normal direction is also a property of the linear-dashpot model employed in the MD simulations. Furthermore, we also assume that the displacement of disks during a collision is negligible, thus the vector that joins the centers of colliding disks is taken to be constant. One last assumption is that gravitational forces are much smaller in magnitude than the contact forces involved in a collision, and gravity can be safely ignored. All these assumptions were tested by comparing collisions in packings simulated by both MD and ED algorithms. We found that collision rules reproduce post-collision velocities obtained in MD simulations when the maximum dimensionless acceleration of the vibrating bottom Γ is larger than 1.

Collision rules are written in terms of the normal and tangential coefficients of restitution e_n and e_t. These coefficients are defined as the ratio of the post-collision velocities to the pre-collision velocities. During the derivation of the collision rules in this section we assume that e_n are e_t are known quantities. Employing the coefficients e_n and e_t allows us to obtain expressions for the collision rules that are independent of the force model employed in the simulations. The details of the force model are encoded into the expressions for calculating e_n and e_t. Coefficients of restitution are obtained for the linear-dashpot model in Section 4.5. Let u_n and u_t be the normal and tangential relative velocities at the point of contact before a collision, and let the primed variables u'_n and u'_t be the post-collision relative velocities. We write the coefficients of restitution as

$$e_n = -\frac{u'_n}{u_n}, \tag{2.7}$$

$$e_t = \frac{u'_t}{u_t}. \tag{2.8}$$

The normal coefficient of restitution takes values between $e_n = 0$ and $e_n = 1$. The value $e_n = 0$ corresponds to a completely inelastic collision, while the value $e_n = 1$ corresponds to an elastic collision. The tangential coefficient of restitution takes values between $e_t = -1$ and $e_t = 1$. The value $e_t = 1$ corresponds to a frictionless collision, while the value $e_t = -1$ corresponds to a complete reversal of the relative tangential velocity. If $e_t = 0$, disks end the collision with zero relative tangential velocity.

The collision rule for the normal velocities v^n of colliding disks i and j can be obtained

from equation (2.7) and conservation of momentum as

$$v'^n_i = v^n_i - \frac{m_{eff}}{m_i}(1+e_n)u_n, \tag{2.9}$$

$$v'^n_j = v^n_j + \frac{m_{eff}}{m_j}(1+e_n)u_n, \tag{2.10}$$

where m_{eff} is the effective mass, and the absolute normal velocity of disks i (v^n_i) and j (v^n_j) is related to the relative normal velocity though $u_n = v^n_i - v^n_j$.

If a disk i collides with a massive wall j with constant normal wall velocity v^n_b, we can take the limit $m_j \to \infty$. In this limit $m_{eff} = m_i$ and $v'^n_j = v^n_j = v^n_b$. The collision rule takes the form

$$v'^n_i = -e_n v^n_i + (1+e_n)v^n_b. \tag{2.11}$$

Note that this collision rule does not conserve momentum.

The relative tangential velocity u_t is measured at the contact point of colliding disks. It includes contributions from both the velocity of the center of mass v^t, and from each disk's rotational velocity ω,

$$u_t = v^t_i - v^t_j + R_i\omega_i + R_j\omega_j, \tag{2.12}$$

where R_i is the radius of disk i.

The following quantities can be derived from conservation of angular momentum around the point of contact:

$$m_i R_i \left(v'^t_i - v^t_i\right) = I_i\left(\omega'_i - \omega_i\right), \tag{2.13}$$

$$m_j R_j \left(v'^t_j - v^t_j\right) = -I_j\left(\omega'_j - \omega_j\right), \tag{2.14}$$

where I_i is the moment inertia of disk i.

The collision rules for tangential and rotational velocities can be obtained from equa-

tions (2.13), (2.14) and (2.8) as

$$v'^t_i = v^t_i - \frac{m_{eff}}{m_i}\frac{(1-e_t)u_t}{1+m_{eff}\left(\frac{R_i^2}{I_i}+\frac{R_j^2}{I_j}\right)}, \tag{2.15}$$

$$v'^t_j = v^t_j + \frac{m_{eff}}{m_j}\frac{(1-e_t)u_t}{1+m_{eff}\left(\frac{R_i^2}{I_i}+\frac{R_j^2}{I_j}\right)}, \tag{2.16}$$

and

$$w'_i = w_i - \frac{R_i m_{eff}}{I_i}\frac{(1-e_t)u_t}{1+m_{eff}\left(\frac{R_i^2}{I_i}+\frac{R_j^2}{I_j}\right)}, \tag{2.17}$$

$$w'_j = w_j - \frac{R_j m_{eff}}{I_j}\frac{(1-e_t)u_t}{1+m_{eff}\left(\frac{R_i^2}{I_i}+\frac{R_j^2}{I_j}\right)}. \tag{2.18}$$

Plugging the moment of inertia for disks, $I = mR^2/2$, into equations (2.15) through (2.18), the collision rules for tangential and rotational velocities become

$$v'^t_i = v^t_i - \frac{m_{eff}}{m_i}\frac{(1-e_t)u_t}{3}, \tag{2.19}$$

$$v'^t_j = v^t_j + \frac{m_{eff}}{m_j}\frac{(1-e_t)u_t}{3}, \tag{2.20}$$

$$w'_i = w_i - \frac{2m_{eff}}{R_i m_i}\frac{(1-e_t)u_t}{3}, \tag{2.21}$$

$$w'_j = w_j - \frac{2m_{eff}}{R_j m_j}\frac{(1-e_t)u_t}{3}. \tag{2.22}$$

If the collision is between a disk i and a massive wall j, moving with constant tangential wall velocity $v^t_b = v'^t_j = v^t_j$, and with zero wall rotational velocity $\omega_j = 0$, the following collision rules can be derived for the velocities of disk i

$$v'^t_i = v^t_i - \frac{(1-e_t)u_t}{3}, \tag{2.23}$$

$$w'_i = w_i - \frac{2(1-e_t)u_t}{3R_i}. \tag{2.24}$$

The collision rules derived in this section do not depend on the force model employed in the simulations. They are generally applicable, provided we specify how to calculate the coefficients of restitution e_n and e_t. One advantage of doing things this way, is that we can try different force models, using the same ED algorithm, by changing only the functions that calculate the coefficients of restitution. In Section 4.5, we give details for the calculation of the coefficients of restitution using the linear-dashpot model, which is the model we implemented in our simulations for disk packings. We purposely delay the derivation of the coefficients of restitution to Chapter 4, after the detailed discussion of the force model given in that chapter.

2.3.2 Detection of events

An integral part of the ED algorithm is the calculation of collision times required for event scheduling [17]. Scheduling requires knowledge about which collision, out of all possible future collisions, will occur next.

Given a state of the system at time t, the time Δt until the next collision of a pair of disks i and j can be solved from the equation

$$r_{ij}(t + \Delta t) = R_{ij}, \tag{2.25}$$

where $r_{ij}(t)$ is the distance between disk centers at time t, and $R_{ij} = R_i + R_j$ is the sum of their radii. Equation (2.25) is just the condition that, at time $t + \Delta t$, disks are touching without overlapping.

We can rewrite equation (2.25) with the aid of the equation of motion for the center of a disk in a constant gravitational field, namely

$$\vec{r}_i(t + \Delta t) = \vec{r}_i(t) + \vec{v}_i(t)\Delta t + \frac{\vec{g}\Delta t^2}{2}, \tag{2.26}$$

where $\vec{r}_i(t)$ is the position vector of the center of disk i at time t, $\vec{v}_i(t)$ is the velocity vector, and $\vec{g}$ is the constant gravitational acceleration vector, of magnitude g, that always points down.

The relative position vector of disk i with respect to disk j, $\vec{r}_{ij} = \vec{r}_i - \vec{r}_j$, at time $t + \Delta t$,

can be written, from equation (2.26), as

$$\vec{r}_{ij}(t+\Delta t) = \vec{r}_{ij}(t) + \vec{v}_{ij}(t)\Delta t, \tag{2.27}$$

where $\vec{v}_{ij} = \vec{v}_i - \vec{v}_j$ is the relative velocity vector. The magnitude squared of the vector $\vec{r}_{ij}(t+\Delta t)$ is

$$r_{ij}^2(t+\Delta t) = v_{ij}^2(t)\Delta t^2 + 2\vec{r}_{ij}(t)\cdot\vec{v}_{ij}(t)\Delta t + r_{ij}^2(t). \tag{2.28}$$

Using equation (2.28), equation (2.25) becomes a quadratic equation for Δt

$$0 = v_{ij}^2(t)\Delta t^2 + 2\vec{r}_{ij}(t)\cdot\vec{v}_{ij}(t)\Delta t + r_{ij}^2(t) - R_{ij}^2. \tag{2.29}$$

For equation (2.29) to have positive solutions for Δt, it is required that disks are approaching each other, i.e., $\vec{r}_{ij}(t)\cdot\vec{v}_{ij}(t) < 0$.

Out of the two possible solutions to equation (2.29), we are interested in the smallest value $\Delta t > 0$ that leads to a collision. This solution is

$$\Delta t = \frac{r_{ij}^2 - R_{ij}^2}{-\vec{r}_{ij}\cdot\vec{v}_{ij} + \sqrt{\left(\vec{r}_{ij}\cdot\vec{v}_{ij}\right)^2 - v_{ij}^2(r_{ij}^2 - R_{ij}^2)}}. \tag{2.30}$$

We have written equation (2.30) in a form that avoids catastrophic cancellation (see [30]) to avoid numerical issues in the simulation.

When the collision involves a disk and a wall, we first define the distance from the wall to disk i as

$$r_{i,wall}(t+\Delta t) = \vec{r}_{ij}(t+\Delta t)\cdot\hat{n}, \tag{2.31}$$

where $\vec{r}_{ij}$ is a vector from a reference point j on the wall to the center of the disk, and $\hat{n}$ is a normal versor to the wall that always points towards the inside of the container. We can rewrite equation (2.31), using equation (2.26), as

$$r_{i,wall}(t+\Delta t) = \vec{r}_{ij}(t)\cdot\hat{n} + \left(\vec{v}_{ij}(t)\cdot\hat{n}\right)\Delta t - \frac{gn_y}{2}\Delta t^2, \tag{2.32}$$

where n_y is the y-component of the versor $\hat{n}$.

Using equation (2.32), we write the condition for a collision with a wall, $r_{i,wall}(t+\Delta t) = R_i$, as

$$(\vec{r}_{ij}(t)\cdot\hat{n} - R_i) + (\vec{v}_{ij}(t)\cdot\hat{n})\,\Delta t - \frac{gn_y}{2}\Delta t^2 = 0. \tag{2.33}$$

The solutions to equation (2.33) are (again written as to avoiding catastrophic cancellation)

$$\Delta t_1 = \begin{cases} \frac{\vec{v}_{ij}(t)\cdot\hat{n} - \sqrt{(\vec{v}_{ij}(t)\cdot\hat{n})^2 + 2gn_y(\vec{r}_{ij}\cdot\hat{n} - R_i)}}{gn_y} & \vec{v}_{ij}(t)\cdot\hat{n} < 0, \\ \frac{-2(\vec{r}_{ij}\cdot\hat{n} - R_i)}{\vec{v}_{ij}(t)\cdot\hat{n} + \sqrt{(\vec{v}_{ij}(t)\cdot\hat{n})^2 + 2gn_y(\vec{r}_{ij}\cdot\hat{n} - R_i)}} & \vec{v}_{ij}(t)\cdot\hat{n} > 0, \end{cases} \tag{2.34}$$

$$\Delta t_2 = \begin{cases} \frac{2(\vec{r}_{ij}\cdot\hat{n} - R_i)}{-\vec{v}_{ij}(t)\cdot\hat{n} + \sqrt{(\vec{v}_{ij}(t)\cdot\hat{n})^2 + 2gn_y(\vec{r}_{ij}\cdot\hat{n} - R_i)}} & \vec{v}_{ij}(t)\cdot\hat{n} < 0, \\ \frac{\vec{v}_{ij}(t)\cdot\hat{n} + \sqrt{(\vec{v}_{ij}(t)\cdot\hat{n})^2 + 2gn_y(\vec{r}_{ij}\cdot\hat{n} - R_i)}}{gn_y} & \vec{v}_{ij}(t)\cdot\hat{n} > 0. \end{cases} \tag{2.35}$$

Of these two solutions, the relevant one, corresponding to the smallest $\Delta t > 0$, is Δt_2. Dropping the sub-index, we write the time Δt until the next collision with a wall as

$$\Delta t = \begin{cases} \frac{2(\vec{r}_{ij}\cdot\hat{n} - R_i)}{-\vec{v}_{ij}(t)\cdot\hat{n} + \sqrt{(\vec{v}_{ij}(t)\cdot\hat{n})^2 + 2gn_y(\vec{r}_{ij}\cdot\hat{n} - R_i)}} & \vec{v}_{ij}(t)\cdot\hat{n} < 0 \\ \frac{\vec{v}_{ij}(t)\cdot\hat{n} + \sqrt{(\vec{v}_{ij}(t)\cdot\hat{n})^2 + 2gn_y(\vec{r}_{ij}\cdot\hat{n} - R_i)}}{gn_y} & \vec{v}_{ij}(t)\cdot\hat{n} > 0 \text{ and } n_y > 0 \\ \infty & (otherwise) \end{cases} \tag{2.36}$$

2.3.3 Fixed-bottom, random-phase approximation

In MD simulations, energy is injected into the system by sinusoidal vibrations of the bottom wall. In ED simulations, moving walls complicate the calculation of the collision time between disks and walls, since this calculation would require numerically solving a transcendental equation. To avoid CPU expensive numerical computations, we, instead, keep the position of the wall fixed. For each collision, a random velocity is sampled from a suitable distribution and assigned to the wall, without actually moving it. We call this the fixed-bottom, random-phase approximation. This approximation is valid in the limit of large frequency and small amplitude of vibration. Since the amplitude is assumed small,

the spatial location of a collision, and, therefore, the collision time t_{col} itself, are practically unaffected by the motion of the bottom. The maximum the bottom velocity is $v_b = A\omega_b$.

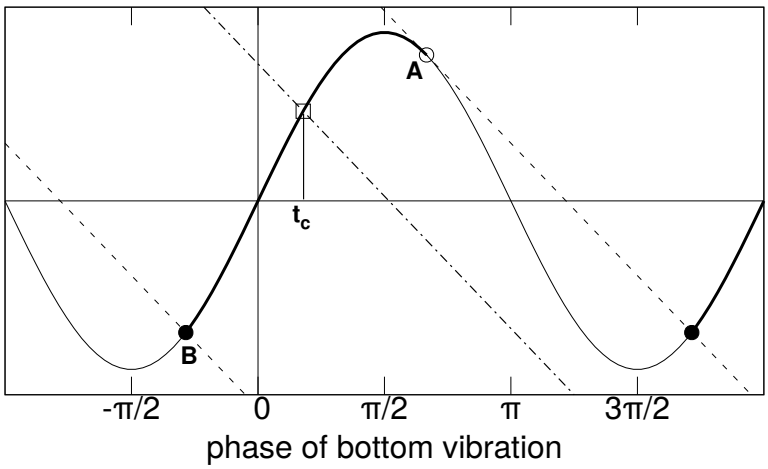

Figure 2.2: Schematic showing how the limiting points A and B are defined. The thin line is the vertical position of the bottom y_b. The dashed lines represent the y coordinate of the incoming disk, with slope v_n. The dot-dashed line depicts a random incoming trajectory, and t_c is the resulting collision phase. The collision may only occur in the region between B and A marked with a thick line.

To calculate the bottom velocity at the collision, we choose to use a "random phase" approximation, i.e. the assumption that the collision occurs at a random time. The resulting distribution of bottom velocities, nevertheless, turns out to depend on the downwards normal velocity v_n of the disk, as illustrated by Fig. 2.2, which displays the position of the vibrating bottom (full line) and of the disk (dashed line) versus the phase of the bottom vibration, $\omega_b t$. There is an "allowed region", delimited by points A and B (thick sinusoidal line), where the collision may happen. When the incoming velocity of the disk is large, points A and B merge, so the collision can happen anywhere, but the distribution of resulting collision phases still depends on the ratio v_n/v_b. We correctly take into account this dependence by generating a random incoming line with the appropriate slope v_n (dot-dashed line in Fig. 2.2) and calculating its intersection phase t_c with the sinusoidal line representing the movement of the bottom. Since the collision is inelastic, there is a set of

bottom velocities for which the collision does not cause the disk to bounce back. In these cases, the disk would continue to move downwards, past the wall and outside the container. When such a case is detected, the sampled bottom velocity is rejected, and a new velocity is sampled from the distribution until it does not present this problem. Rejection events are unusual in the regime where the validity of ED simulation holds. We call this sampling method the fixed-bottom, random-phase approximation, and we will refer to it as FBRPA from now on.

We tested a few other forms for the distribution of the bottom velocity at the time of the collision, and found that none of the results are modified qualitatively, as long as the typical bottom velocity v_b is the same. In particular, we tried a sawtooth profile for the bottom motion (instead of sinusoidal), which implies that the bottom always moves upwards with velocity v_b at any collision, no matter what the incoming velocity v_n of the disk is. For the simplified system of a disk bouncing in a wedge (Chapter 6), this case gave results that, after discounting for a constant factor, were equivalent to those obtained with sinusoidal excitation. This suggests that the observed spontaneous rotation is robust to some extent. The important parameter is the typical bottom velocity v_b, that determines the amount of energy injected into the system by one collision. The actual distribution of bottom velocities appears to be irrelevant. This universality with respect to the type of excitation could be perhaps understood by analogy with thermal physics. Within the FBRPA, wedge walls play the role of a heat bath. Every time the disk hits the wall, a wall velocity is sampled from a distribution whose typical value is $v_b = A\omega_b$, the details of which appear to be unimportant.

For the system described in Chapter 6, despite the simplifying assumptions involved in the FBRPA, we find that numerical results (e.g. rotational velocities of the upper disk) obtained from ED simulations within the FBRPA agree with those from MD simulations (no approximation) quite well. See Section 6.3.3.

Although not required to employ the FBRPA, we now give a derivation of the distribution of bottom velocities and calculate its first two moments. This results may prove useful in a future analytic treatment of rotation in disk packings.

The position and velocity of the bottom plate follow are given by

$$y_b = A\sin(\omega_b t) \tag{2.37}$$

$$v_b = A\omega_b \cos(\omega_b t) \tag{2.38}$$

The probability density function (pdf) of the bottom velocity v_b, without taking into account the incoming disk velocity v_n, is the pdf of a sine function. The pdf is proportional to the time spent around v_b, i. e., $P(v_b)dv_b \propto dt(v_b)$, and is calculated as

$$P(v_b) = \frac{1}{w\pi\sqrt{A^2\omega_b^2 - v_b^2}} \tag{2.39}$$

When sampling v_b for a collision, the pdf given by equation (2.39) applies only in the limit of a very large disk velocity, $v_n \to \infty$. A finite v_n causes a shadowing effect that makes some bottom velocities inaccessible, making it more likely that the collision occurs for positive values for v_b (see Figure 2.2).

Let $P(v_b|v_n)$ be the probability that a disk, arriving with velocity v_n, encounters a bottom velocity of v_b. To find $P(v_b|v_n)$, we build a piece-wise function for the bottom velocity that is non-zero only inside the valid region. This region is delimited by points A and B of Figure 2.2. We can find the time t_A, of point A, using the fact that, at this point, the slope of y_b becomes equal to the disk velocity v_n. The time t_B, of point B, must be found numerically or approximated somehow. We need to take into account that some velocities need to be counted twice, due to the periodicity of the sine function. Also, there is a contribution from the width x of a bundle of ray trajectories as a function of an infinitesimal time interval, dx/dt. Up to a normalization factor, we have:

$$P(v_b|v_n) = \begin{cases} 0, & \text{if } v_b < v_b(t_A) = v_n \text{ or } (v_b > v_b(t_B) \text{ and } t_B > 0) \\ 2\frac{dt}{dv_b}\frac{dx}{dt} = 2\frac{v_n - v_b}{\sqrt{A^2\omega_b^2 - vb^2}}, & \text{if } v_b > v_b(t_B) \text{ and } t_B < 0 \\ \frac{dt}{dv_b}\frac{dx}{dt} = \frac{v_n - v_b}{\sqrt{A^2\omega_b^2 - vb^2}}. & \text{otherwise} \end{cases} \tag{2.40}$$

To obtain t_B we need to solve the equation $y_b(t_B) = v(t_B - t_A) + A\sin(\omega t_A)$. Assuming

a linear relationship, we can fit the following linear equation for t_B

$$t_B = \begin{cases} \frac{3\pi}{2A\omega_b^2} v_n + \frac{\pi}{2\omega_b}, & |v| < A\omega_b \\ -\frac{\pi}{\omega_b}, & |v| > A\omega_b \end{cases} \tag{2.41}$$

This gives

$$v_b(t_B) = \begin{cases} -A\omega_b \sin(\frac{3\pi}{2} \frac{v_n}{A\omega_b}), & |v| < A\omega_b \\ -A\omega_b, & |v| > A\omega_b. \end{cases} \tag{2.42}$$

Integrating using the appropriate limits, we can now write expressions for the expected values $\langle v_b \rangle$ and $\langle v_b^2 \rangle$

$$\langle v_b \rangle = A\omega \; f\left(\frac{v}{A\omega}\right) \tag{2.43}$$

$$\left\langle v_b^2 \right\rangle = A^2\omega^2 \; g\left(\frac{v}{A\omega}\right), \tag{2.44}$$

where the functions f and g depend only on the dimensionless parameter $v_n/A\omega_b$. In the limit of high normal velocities, $\beta = |v_n|/A\omega_b > 1$, $f = 1/2\beta$ and $g = 0.5$.

$$\langle v_b \rangle = -\frac{A^2\omega_b^2}{2v} \tag{2.45}$$

$$\left\langle v_b^2 \right\rangle = \frac{A^2\omega_b^2}{2}. \tag{2.46}$$

In this limit, the entire sinusoidal profile is sampled, while in the opposite limit, of zero normal velocity, the disk will always collide with a bottom moving at its maximum bottom velocity v_b.

2.4 Description of the experimental procedure

2.4.1 The experimental setup

We performed a set of experiments on disk packings designed so that comparison between numerical and experimental results is possible. This means that conditions in both experi-

ments and simulations should be similar, such as using the same number of disks, with the same size distribution and subject to a comparable vibrational excitation. A photograph of the experimental apparatus is shown in Figure 2.3.

Sixty disks were cut from a 3 mm acrylic sheet, and a lathe was used to smooth the edges. In order to avoid spontaneous crystallization of the packing, disks were machined with three different radii: twenty disks with a 1.5 cm radius, twenty with a 2.0 cm radius and twenty with a 2.5 cm radius. Each disk is marked with a centered rectangle made from black tape (labeled M in Figure 2.4), this mark is used to track rotations, as described below. White translucent acrylic was chosen as the base material, as it lets through and diffuses light from an LED backlight, which enhances contrast in the images.

Disks are held in a container made of two panes of 6 mm thick tempered glass. The back pane is 50×50 cm and is translucent white in order to diffuse the backlight. The front pane measures 50×44 cm and is completely transparent. Both panes are bolted to a steel frame using six 1/4 inch bolts, four of which are labeled B in Figure 2.4. The fixed steel frame is in turn bolted to the laboratory floor. Between panes, at the left and right borders, two stripes of 4 mm acrylic (S in Figure 2.4) are used to provide the required spacing for disks to rotate freely. Figure 2.4 shows a packing inside the container with the backlight on.

The top and bottom of the container are left open. Disks can be introduced into the container from the top. Through the bottom opening, an aluminum profile, machined down to 3 mm thickness, acts as a mobile bottom wall (labeled P in Figures 2.3 and 2.4). This aluminum profile is restricted to move vertically by a two-rail system, as shown in Figure 2.5. Two steel rods (R in Figure 2.5), 20 cm apart from each other and 12 mm in diameter, are attached to a fixed steel frame below the glass container. On each rod, a linear bearing (B in Figures 2.3 and 2.5) is free to slide. Rigidly attached to both bearings is a rectangular aluminum profile (A in Figures 2.3 and 2.5) of 2×4 inches cross-section and 40 cm long. On top of the aluminum profile A the L-shaped profile P is attached so that it may enter the glass container from the bottom. A threaded 1/4 inch rod is bolted to the rectangular profile B centered at its bottom face. This rod connects the profile B to a loudspeaker L, where is bolted to an acrylic pane glued to the speaker. The loudspeaker vibrates and moves the bottom wall of the container P. The speaker is driven by a 1500 W signal amplifier, that is in turn connected to a computer using a standard 3.5 mm TRS

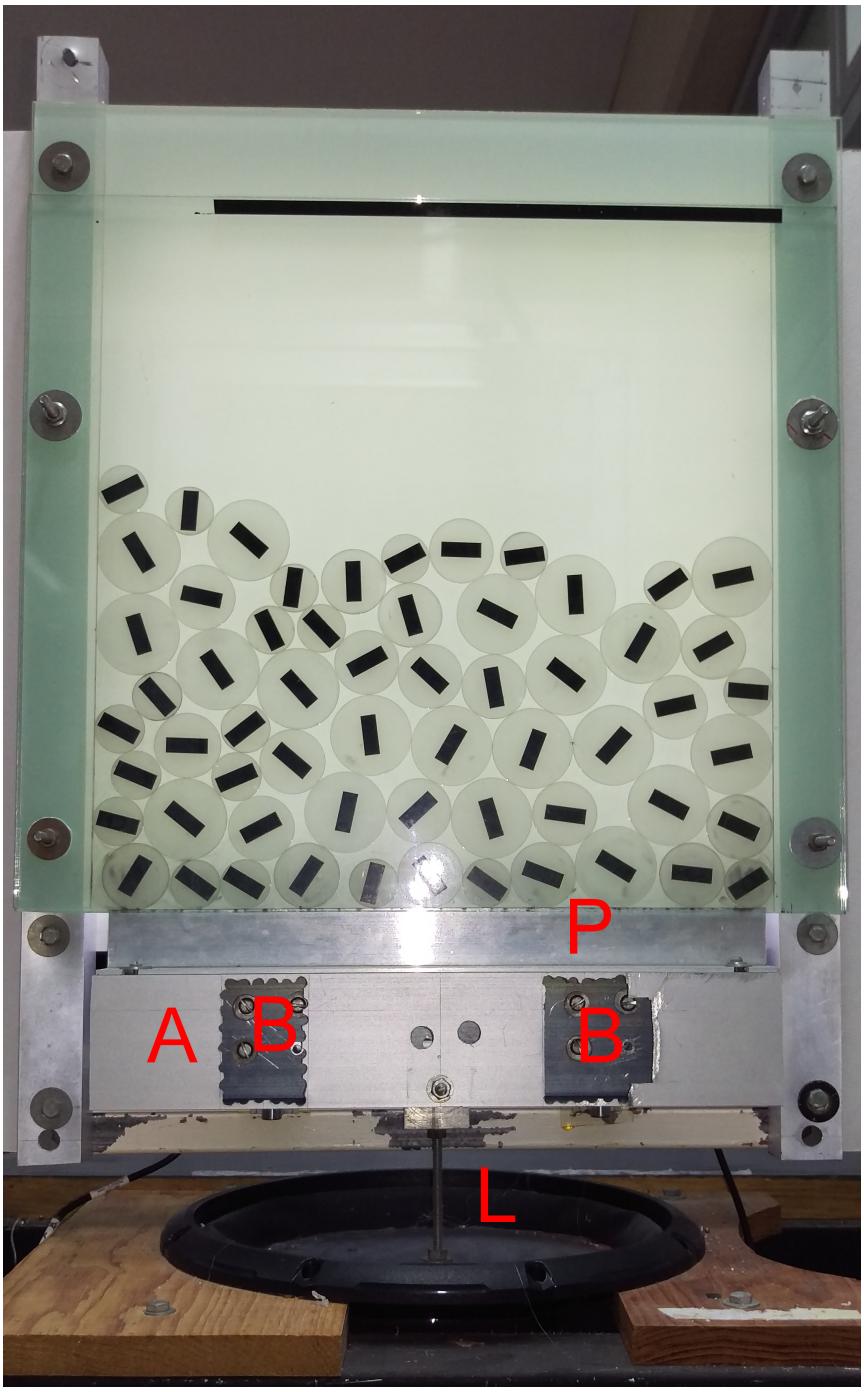

Figure 2.3: The experimental apparatus used to study rotation in disk packings. Disks are held between two glass sheets. Labels are as follows. B: Linear ball bearings. A: Square aluminum profile. P: Vibrating L-shape profile. L: Loudspeaker.

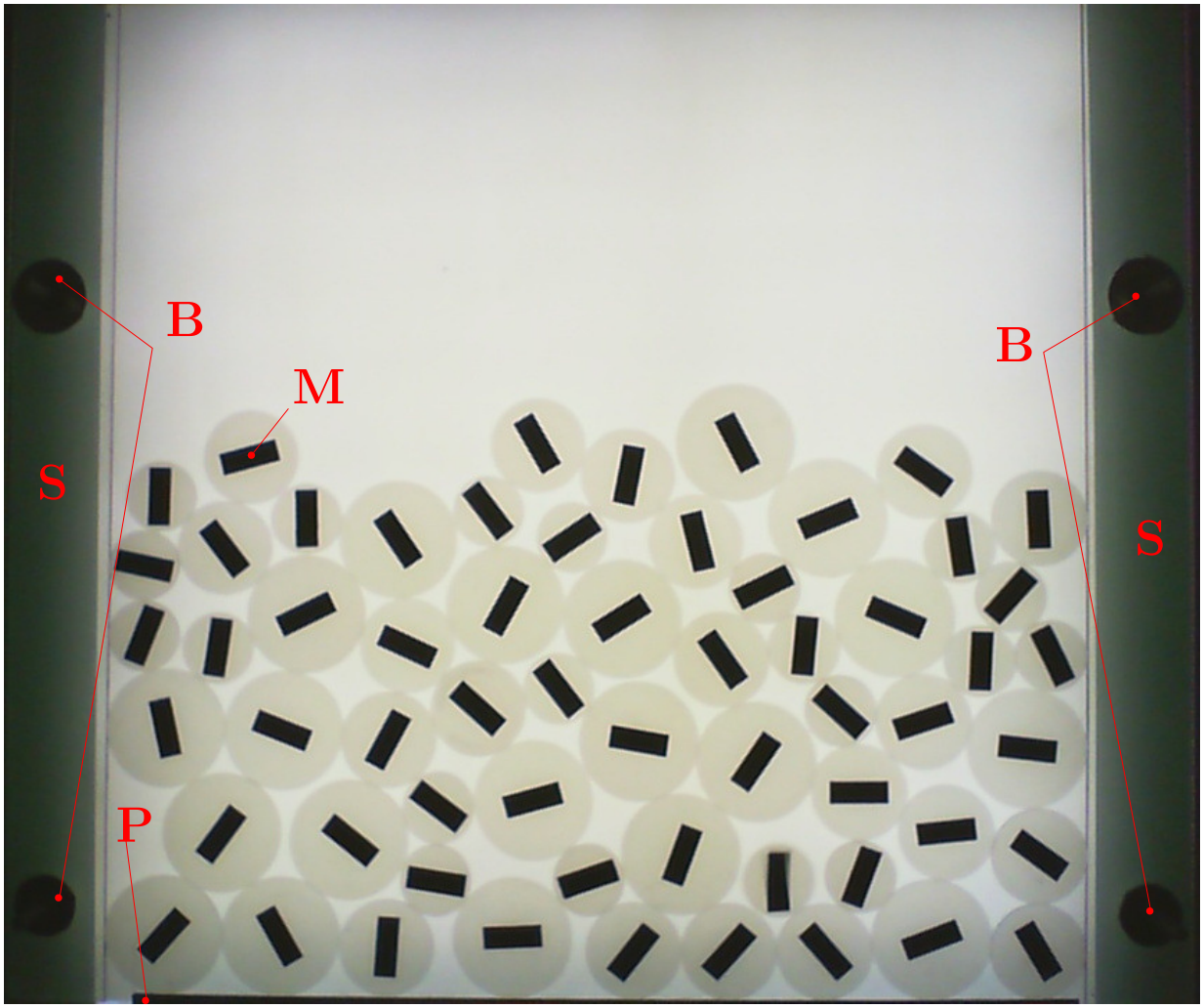

Figure 2.4: Snapshot of an experimental 60 disk packing with the backlight on. Twenty disks have 1.5 cm radius, twenty a 2.0 cm radius, and twenty a 2.5 cm radius. Labels are as follows. M: special mark to track rotations. B: 1/4 inch bolts. S: Acrylic stripes as spacers between glass panes. P: Vibrating bottom.

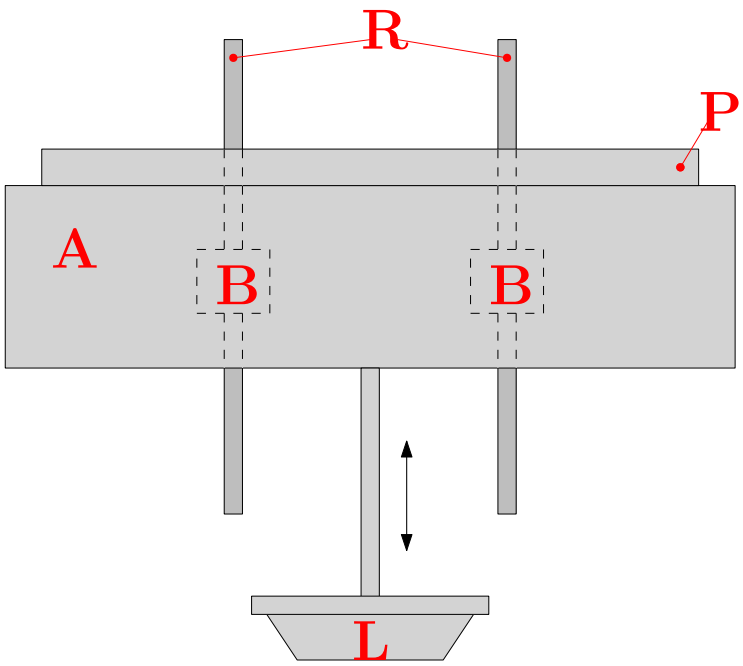

Figure 2.5: The rail system restricting the movement of the L-shape aluminum profile P. Profile P acts as a mobile bottom wall for the glass container. Labels are as follows. R: Steel rods. B: Linear ball bearings. A: Square aluminum profile. P: Vibrating L-shape profile. L: Loudspeaker.

minijack cable. The computer generates a sinusoidal waveform using a custom Python script.

2.4.2 Running an experiment

The process to run a single experiment is as follows. We start with an empty box, disks are poured into the container through the top without any particular order, the intention is to obtain a different packing for each run. After the packing is ready, a custom Python script running in a laboratory computer takes care of both the data acquisition and of generating the signal fed to the amplifier. After the script finishes, execution data is copied to an external drive for further analysis, and the container is emptied leaving it ready to start a new experiment with a different packing.

The signal amplitude A is set in the script with a number between 0 and 1. The script

starts by setting the amplitude to its maximum value $A = 1$ during 5 minutes, to allow the packing to settle in a stable configuration. At 20 minute intervals, the signal amplitude is decreased by 0.05 down to $A = 0.2$, afterwards it is decreased by 0.01 down to $A = 0.050$. No data is recorded during the first 5 minutes of each 20 minute interval. This time is used to let the packing stabilize under the new conditions of vibration. After the 5 minute period of relaxation, data acquisition starts. A webcam connected to the computer and controlled by the script takes photos at every second during the remaining 15 minutes of each 20 minute interval. The photos are used to track rotations during the data analysis step. Since the wave amplitude A of the speaker input does not give information regarding the actual amplitude of the vibrating speaker, two adxl345 acceleremoter sensors are placed in each bearing of the rail setup of Figure 2.5. These sensors measure acceleration data at a 200Hz data rate. Sensors send data to two Arduino Duemilanove prototyping boards that in turn relay the data to the computer. The script receives the data and stores in text files for further analysis.

2.4.3 Processing experimental data

After an experiment concerning a single packing is done, we are left with two sets of data to analyze: a set of snapshots containing the information of the system response, this is, rotational velocity of each disk; and acceleration data containing the information about the intensity of the vibrational excitation.

Visual data

Visual data are analyzed using the Fiji software [31]. Fiji is a collection of computer vision algorithms running under the ImageJ platform. A predefined macro (collection of automatized steps) applies the following procedure to each image of a set: First the image is converted to 8-bit gray-scale. An automatic threshold is then applied. A threshold converts a gray-scale image into a binary black and white image by taking all pixels with brightness over the threshold and making them white, while making all pixels under the threshold black. This process filters most of the image and leaves only the special markings (M) on each disk due to the sharp contrast between the markings and the rest of the image

(see Figure 2.4). The "analyze particles" feature of the Fiji software is then applied. The algorithm identifies each black rectangle (marking), fits an ellipse to it and applies a numerical label to identify each marking (1, 2, 3, etc). The fitted parameters of the ellipses contain the location of the center of mass and the angle of the major axis each ellipse makes with the x axis of the image. These fitted parameters are saved to a single text file to represent a time series with position and angular information of each disk at 1-second intervals.

Angles returned by the "analyze particles" algorithm can only take values between 0 and 180 degrees. Furthermore, the algorithm doesn't try to identify corresponding disks between images, so labels may not correspond to the same disk. A custom python script applies a last processing step. To identify a disk in the next frame, we find the disk closest to it, and assume it is the same disk, displaced a small distance. This last step works because disks maintain their position within the packing. When a packing reorganization occurs (a rare event, see 1.3) disks move slowly enough for the tracking to still work. Once disks are properly labeled, a continuous time series is built for the angles by applying the following transformation to the data. With $\theta[i]$ the angle at the second i, we find the difference $\Delta\theta = \theta[i] - \theta[i-1]$ between two consecutive frames. The series for the angle θ is supposed be continuous. This means $|\Delta\theta|$ cannot be too large. Due to the fact that the software only assigns values between 0 and 180 degrees, a value of $\Delta\theta > 90$ is taken to be caused by rotation near the value of 180 (or 0) degrees. To correct for this, we shift all angles in the series up to time $i-1$ by subtracting 180 degrees from all of them, making $\Delta\theta < 90$. If $\Delta\theta < -90$ we apply a similar correction by adding 180 degrees to the series. After running through all frames, we end up with a continuous time series for θ. The

pseudo code for this algorithm is given below:

for all i beginning with $i = 1$ **do**
  $\Delta\theta \leftarrow \theta[i] - \theta[i-1]$
  if $\Delta\theta > 90$ **then**
    for all $j < i$ **do**
      $\theta[j] \leftarrow \theta[j] - 180$
  else if $\Delta\theta < -90$ **then**
    for all $j < i$ **do**
      $\theta[j] \leftarrow \theta[j] + 180$
done

Acceleration data

Two acceleration time series, one for each accelerometer, are stored in a text file each. Each point of the series gives the instant acceleration of the bottom, as measured by the sensor. These sensors measure acceleration within a range of ± 16 g with a precision of 0.01 g. Two components of noise affect the measurements: the intrinsic error of the sensor and the impacts of the disks with the bottom of the container. Noise from both sources makes it impossible to determine the amplitude of the oscillation by visual inspection of a sensor data plot. Simply taking the maximum and minimum value as the amplitude also fails since there exists large random deviations from the mean.

The approach we took is simple. The loudspeaker is driven by a sine wave of known frequency, so we may assume that acceleration data can be modeled as a sine wave with the same frequency subject to noise. To reduce this noise, we calculate the spectral density of the acceleration signal. We then take the sum of the density in a 10 Hz frequency window centered at the known frequency of the driving signal. One can think of this procedure as applying a band pass filter, and keeping only the contributions to the variance around the desired frequency.

For a pure sine of amplitude A, the standard deviation is $SD = A/\sqrt{2}$. We take the square root of our filtered variance as an estimate of the corresponding standard deviation

of the input signal. Then the amplitude a_g can be estimated as

$$a_g = \sqrt{2} \cdot SD_{filtered}. \tag{2.47}$$

The mean from the estimations of the two sensors is taken as the value of the acceleration amplitude. For each individual sensor, the acceleration time series always averaged to $\langle a_b \rangle = -g \pm 0.01\ g$, the value of the gravitational acceleration, as it should for a noise term of zero mean.

3 Rotation in disk packings

In this Chapter we discuss the phenomenon of sustained rotation in vibrated disk packings. We start with a quantitative description of results from experiments with real packings. Next, we compare the statistical behavior of the rotational velocity in experimental and simulated packings. Finally, we analyze simulation data in detail and explore how different parameters influence the rotational velocity observed in the packings.

3.1 Laboratory experimental observations

Experiments described in this Section were performed with packings of 60 acrylic disks subject to gravity. Disk were placed inside a glass container with a movable bottom wall, as described in Section 2.4.1. The radii distribution was as follows: 20 disks with a 1.5 cm radius, 20 disks with a 2 cm radius, and 20 disks with a 2.5 cm radius. The experimental procedure described in Section 2.4.2 was applied to 25 different packings. One of such packings is shown in Figure 2.4. A vibrating loudspeaker, coupled to the bottom wall of the container, was used to inject energy into the packing. The speaker received a sinusoidal signal with frequency of $f_b = 80$ Hz. The amplitude of the vibration was varied in fixed steps during a single experiment. Data from each packing were recorded and processed according to the method described in Section 2.4.3. Both the acceleration of the bottom wall and the angle of each disk were recorded. Acceleration of the wall is reported using the dimensionless parameter Γ, defined in Section 2.4.3 as the ratio of the peak wall acceleration to gravity.

As discussed in Section 1.3, a disk's rotational velocity is presumably determined by the contact configuration with its neighbors. This configuration is part of the contact network of a packing. For disordered packings (as is the case in this study), the network can be

considered as a random realization of possible configurations. Consequently, the rotational velocity of a disk is also random in this sense.

Figure 3.1 shows plots of the angular path θ for each of the disks belonging to one of the 25 experimental packings. Velocities are symmetrically distributed around zero, as expected due to left-right symmetry. For $\Gamma = 0.24$, rotation accumulates for each disk, but angular paths are not linear in the time-scale under consideration. As the intensity of the vibration increases, the relative amplitude of the noise in each path decreases, making paths appear more linear. For $\Gamma = 2.09$ and larger, the maximum rotational velocity seems to saturate, but the typical velocity of the packing, estimated using the root mean square of the velocities (see below), grows with Γ. From the figure, this growth can be appreciated from the increased spanning of lines as Γ increases.

The mean rotational velocity $\bar{\omega}$ of each disk is calculated as the total angular excursion over time. For a disk rotating with constant angular velocity, the angular path is a line with slope $\bar{\omega}$. Most of the disks in Figure 3.1 follow approximately straight paths, which means their rotational velocity fluctuates slightly around the mean value $\bar{\omega}$. For $\Gamma = 0.91$, some angular paths change slope near time $t = 450$ s. This change implies that the value of $\bar{\omega}$ is different for the time intervals before and after the change in slope, i.e., the mean velocity of the disk is changing. The slope differences are caused by a partial reorganization of the packing. Packing reorganization is typically triggered by a change in some excitation parameter, for example, when changing Γ during the experiments, but spontaneous reorganization, without varying any parameter, does occur, as is the case for $\Gamma = 0.91$ in Figure 3.1. Spontaneous reorganizations is not frequent, but can still cause a change in velocities during a experiment. Vibrated granular matter are systems out of equilibrium, and as such, they are able to explore different states in configuration space. A few of this states will be locally stable. Transitions between stable states are possible if they lie close in configuration space. These reorganizations change the contact network of the packing in turn changing the mean rotational velocity of the disks. All observed reorganizations were limited to a small fraction of the packing, typically involving less than 10 disks. We, thus, ignore this events, and always average the rotational velocity along the full angular path of the disk.

The root of the mean squared rotational velocity $\langle \bar{\omega}^2 \rangle$ can be used to estimate the

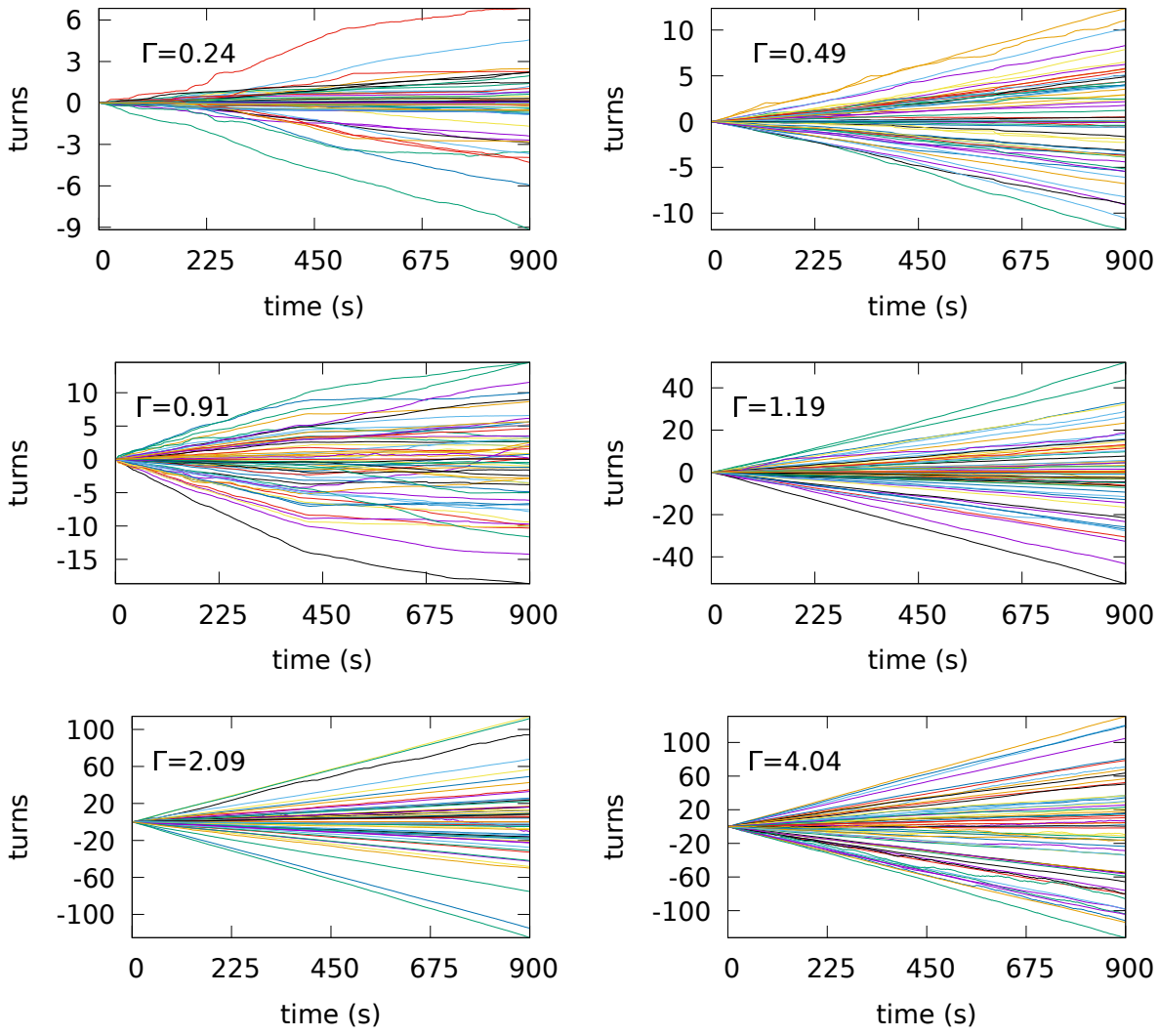

Figure 3.1: Angular paths for each of the disks of a packing studied in the laboratory. Each plot corresponds to a different bottom excitation Γ. The velocity change near $t = 450$ s for $\Gamma = 0.91$ is caused by a reorganization of the packing contact network.

magnitude of the absolute rotational velocity in disk packings. There are two different types of averaging that can be made, the mean over a packing and the mean over all packings. The mean over a single packing is easily calculated as the sum of the squared mean velocities of all disks divided by the total number of disks. For a single packing, a packing mean is calculated for each different value of vibration amplitude Γ. To obtain the mean over all packings, $\langle\bar{\omega}^2\rangle$, the straightforward way would have been to average packing mean values obtained for the same value of Γ. The problem was that recorded Γ values were different for different packings, even if the vibrating speaker was driven with the same sinusoidal signal. The different in Γ values can be attributed to the response different packing configurations have to vibration, as well as to the effect of noise in the acceleration sensors. Different packings have a different mass distribution and a different contact network. When vibrated, there exist an energy feedback into the speaker from the collisions with the disks in the packing. This feedback is different for each packing configuration. Since the speaker is not massive enough to neglect feedback effects, feedback can have a measurable influence in the effective acceleration of the bottom wall. To circumvent this problem, we employed a local regression algorithm that averages in both $\bar{\omega}$ and Γ. We have chosen to employ a K-Nearest-Neighbors (KNN) algorithm, as it is one of the simplest non-parametric regression methods available [32]. KNN is unbiased in the sense that it does not make any assumption of of the form of the function being fitted.

To obtain the mean squared rotational velocity $\langle\bar{\omega}^2\rangle$ among all packings, a KNN algorithm is applied to the data set of the previously calculated means for each packing. The number of neighbors K is set to $K = 25$, the number of different packings used in the experiments. Note that this averaging process is equivalent to applying a KNN algorithm, with $K = 1500$, to the data set of all $(\Gamma, \bar{\omega})$ data points taken from all disks, independently of the packing they belong to. The number of neighbors, $K = 1500$, is calculated as (# of disks in a packings) $\times$ (# of packings) $= 60 \times 25$. Using this last alternative we can skip the step of averaging over single packings. Each of the 25 packings was vibrated with 37 different amplitudes for a total of 55500 data points, each representing the behavior of a single disk over a 15-minute period.

Figure 3.2, top, shows a KNN regression of $\langle\bar{\omega}^2\rangle$ on the bottom acceleration Γ for disks from all experimental packings. The same regression is shown in Figure 3.2, bottom, on

log-log scale. Linear regions in the log-log graph suggest a power law scaling, of the form $\langle v^2 \rangle \propto \Gamma^k$, for each region. Least-squares was used to fit a line to both regions, these lines are shown in the log-log plot of Figure 3.2. For $\Gamma < 1$, least-squares fits an exponent $k \approx 4$ (actual fitted value of 3.94), resulting in the scaling $\langle \bar{\omega}^2 \rangle \propto \Gamma^4$. For $1.6 < \Gamma < 4.5$, least-squares fits an exponent $k = 1.00$, resulting in the scaling $\langle \bar{\omega}^2 \rangle \propto \Gamma$.

The scaling transition, from $k = 4$ to $k = 1$, is located at $\Gamma \approx 1.6$, close to the relevant threshold, for vibrated granular matter, of $\Gamma = 1$ (see Chapter 1 and reference [33]). Resembling what happens to a bouncing ball (see [34]), at $\Gamma = 1$, a packing of rigid grains will stop behaving as a solid block, and grains will start bouncing on the oscillating plate. For viscoelastic particles, the position of this threshold may shift from $\Gamma = 1$. The magnitude and direction of the shift depends on the stiffness and viscosity of the material [35]. This shift may explain why we observe a scaling transition at $\Gamma = 1.6$ instead of at exactly $\Gamma = 1$.

Returning to Figure 3.1, some randomness in the angular paths can be detected by visual inspection. We quantify the linearity of the path using two quantities. The first one is the squared correlation coefficient $\rho^2_{\theta,t}$, that measures the correlation between the angle θ and time. The second one is the adjusted standard deviation σ_a, defined as

$$\sigma_a = \frac{\sigma_{\bar{\omega}}}{|\bar{\omega}| + \sigma_{\bar{\omega}}}, \tag{3.1}$$

where $\sigma_{\bar{\omega}}$ is the standard deviation of the velocity measurements. Standard deviation $\sigma_{\bar{\omega}}$ is calculated from the angle time series, where angle values were recorded at 1-second intervals. For each 1-second interval, a mean rotational velocity is calculated as the angle difference, resulting in a new time series for the disk velocity. The standard deviation of these mean velocities is $\sigma_{\bar{\omega}}$.

The coefficient $\rho^2_{\theta,t}$ is equivalent to the R^2 coefficient of a least-squares linear regression of angle vs time. This coefficient takes the value of $\rho^2_{\theta,t} = 1$ when the path is perfectly linear, and the value of $\rho^2_{\theta,t} = 0$ for a random walk without drift (zero mean). Values in between correspond to paths with a finite mean velocity, i.e., with a fitted slope larger than zero. The variance with respect to the least-squares fitted line is quantified by $\rho^2_{\theta,t}$.

The adjusted standard deviation σ_a can take values between 0 and 1. When the velocity

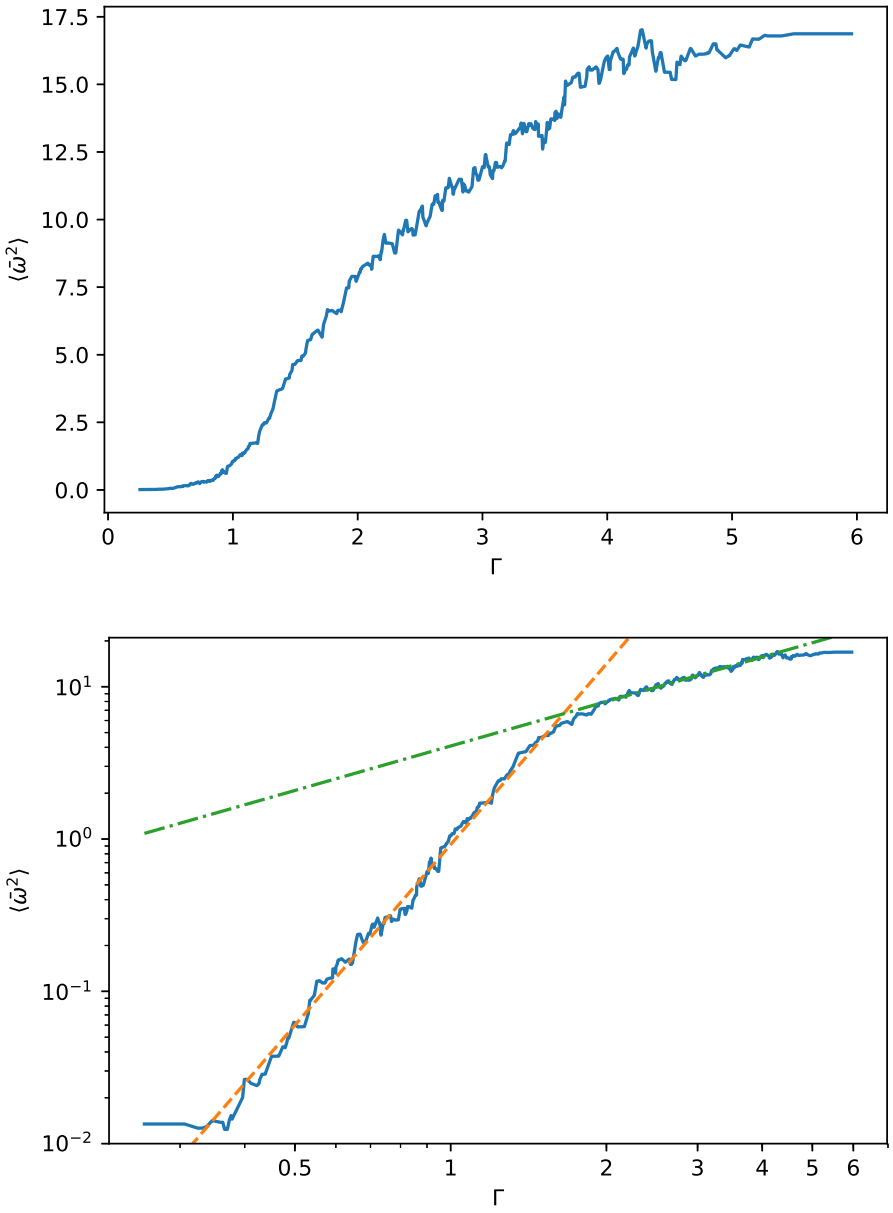

Figure 3.2: KNN regression of the mean squared rotational velocity $\langle\bar{\omega}^2\rangle$ on Γ. Top: Linear scale plot. Bottom: log-log plot. Straight lines come from least square fits on the log-log graph. The dashed line has slope 3.94 and the dot-dashed line has slope 1.00. Velocity is measured in revolutions per minute RPM.

is nearly constant and fluctuates slightly around $\bar{\omega}$, $\sigma_{\bar{\omega}} \ll \bar{\omega}$, and σ_a approaches 0. On the other limit, when fluctuations dominate, $\sigma_{\bar{\omega}} \gg \bar{\omega}$, and σ_a approaches 1.

Quantities $\left\langle \rho^2_{\theta_t} \right\rangle$ and $\langle \sigma_a \rangle$, averaged over all packings, are shown in Figure 3.3 plotted against the bottom acceleration Γ. Initially, $\langle \rho^2 \rangle_{\theta,t}$ grows and $\langle \sigma_a \rangle$ decreases with vibration amplitude. After $\Gamma \approx 1.6$, both quantities stabilize. The correlation coefficient stabilizes at around $\left\langle \rho^2_{\theta_t} \right\rangle \approx 0.95$, and the adjusted deviation at around $\sigma_a \approx 0.4$. The saturation threshold is the same at which the scaling of $\langle \bar{\omega}^2 \rangle$ changes (see Figure 3.2), supporting the hypothesis of a regime transition near $\Gamma = 1$. The evolution of $\rho^2_{\theta,t}$ and σ_a tells us that, initially, paths become, in average, increasingly linear with increasing vibration amplitude Γ. After, $\Gamma = 1.6$, this increase in linearity stops, and fluctuations and velocities increase proportionally, as to keep the mean values of $\rho^2_{\theta,t}$ and σ_a nearly constant.

Near the transition threshold, $\Gamma = 1.6$, $\left\langle \rho^2_{\theta,t} \right\rangle$ and σ_a display fluctuations larger than those far from the threshold. Remember that the Γ values are estimated from a rough statistical analysis on the acceleration data from the experiments (see Section 2.4.3). The uncertainty in the measured values of Γ may cause a mixture of regimes near the threshold, resulting in large fluctuations. In Section 3.2, we analyze simulated packings, where the uncertainty in Γ does not exist. These simulations display a cleaner transition for averaged quantities.

For the time scale under consideration, it is difficult to determine if disks with low $\rho^2_{\theta,t}$ (or high σ_a) are actually rotating systematically, albeit really slowly, or if θ behaves like a random walk, and the estimated velocity comes from the fact that we are sampling θ when the angle is away from the mean (but will eventually return to zero). We argue that the later case is more likely, and disks with low $\rho^2_{\theta,t}$ are not really rotating. If this is the case, an increase in $\left\langle \rho^2_{\theta,t} \right\rangle$ (or a decrease in $\langle \sigma_a \rangle$) means that the fraction of rotating disks within the packing is increasing. At $\Gamma = 1.6$, all disks that can rotate have begun to do so, and $\left\langle \rho^2_{\theta,t} \right\rangle$ stabilizes at a value close to 1.

The bimodal character of the distribution of $\rho^2_{\theta,t}$ indicates that we can classify disks in a packing as rotating or non-rotating, differentiating them by their $\rho^2_{\theta,t}$ value. Figure 3.4 shows two probability density histograms for the $\rho^2_{\theta,t}$ value of disks from 25 experimental packings closest to a particular value of Γ (the nearest neighbors). The one with $\Gamma = 0.3$ is characteristic of all acceleration values below the threshold $\Gamma = 1.6$. It shows that most

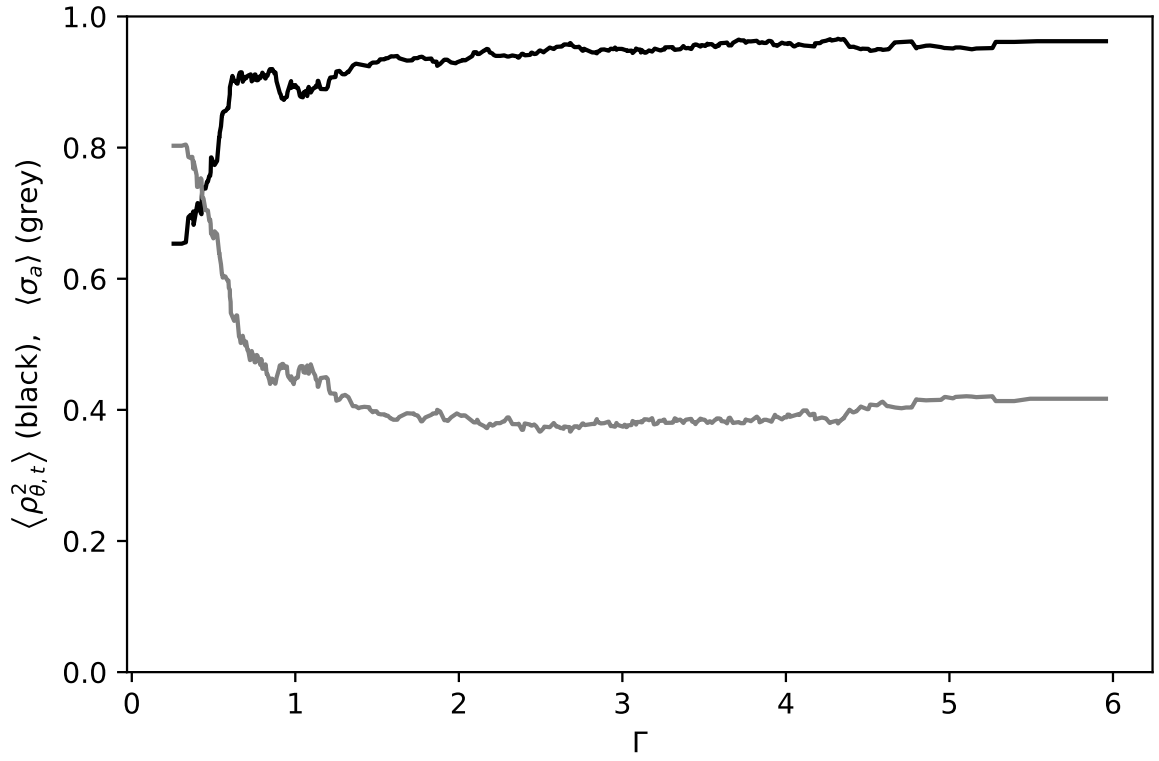

Figure 3.3: The mean correlation coefficient $\langle \rho^2_{\theta,t} \rangle$ in black, and the adjusted standard deviation σ_a in gray, averaged from all experimental packings using k-nearest neighbors regression. The increase (decrease) of $\langle \rho^2_{\theta,t} \rangle$ (σ_a) are interpreted as increased fluctuations in the rotational velocities of the disks within the packing. The saturation of both quantities at $\Gamma \approx 1.6$ support the hypothesis of a region transition around this value.

of the disks have either a $\rho^2_{\theta,t}$ value close to zero, or an $\rho^2_{\theta,t}$ value close to 1. The $\rho^2_{\theta,t}$ zero values correspond to non-rotating disks, while the high $\rho^2_{\theta,t}$ values correspond to disks rotating with near constant velocity. The histogram for $\Gamma = 4.0$ is typical of acceleration values above the threshold $\Gamma = 1.6$. It shows most disks have a value of $\rho^2_{\theta,t}$ near one, and are, thus, rotating with near constant velocities.

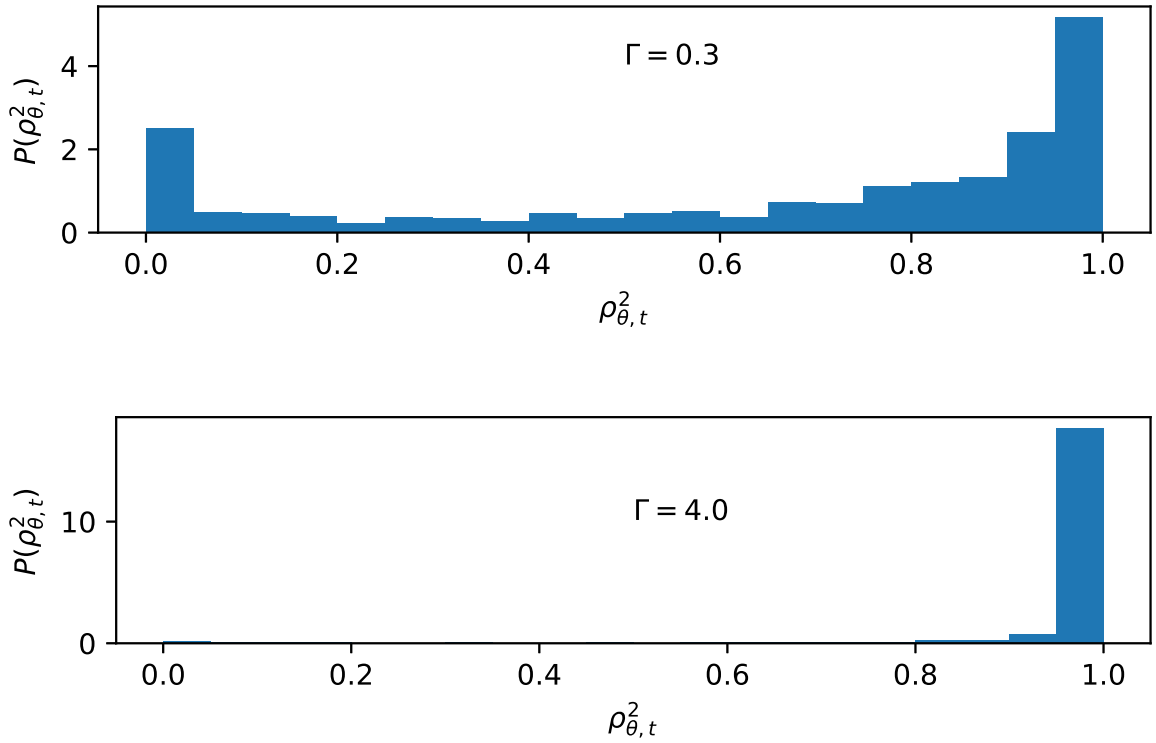

Figure 3.4: Probability density histograms of the mean correlation coefficient $\rho^2_{\theta,t}$ for the 25 experimental packings with Γ values closest to $\Gamma = 0.3$ (top) and $\Gamma = 4.0$ (bottom). The histogram for $\Gamma = 0.3$ shows a concentration of disks with highly noisy angular paths corresponding to values of $\rho^2_{\theta,t}$ near zero, and another concentration of disks with linear angular paths corresponding to values of $\rho^2_{\theta,t}$ near one. For $\Gamma = 4.0$ practically all disks have values of $\rho^2_{\theta,t}$ near 1, corresponding to almost linear angular paths.

3.2 Molecular Dynamics Simulations

In the Introduction (Chapter 1), we mentioned that rotations in disk packings were first observed in Molecular Dynamics simulations. In this Section, we present results from these simulations and show that they are consistent with the experimental results from Section 3.1. These simulations were performed with the same number of disks, the same radii distributions, and the same vibration frequency as in the experiments with real packings. A total of 100 different packings were simulated for each value of dimensionless acceleration Γ. The bottom acceleration ranges from $\Gamma = 0.1$ to $\Gamma = 29$, much larger than the experiments. Parameters for these simulations are: normal stiffness $k_n = 10^4$, stiffness ratio $k_r = 0.77$, normal viscous coefficient $\gamma_n = 0.1$, friction coefficient $\mu = 0.1$, and material surface density $\rho = 3.57$ kg/m^2.

Figure 3.5 shows plots of the angular path θ for each of the disks belonging to one of the 100 simulated packings. Paths for $\Gamma < 1$ seem more linear (less noisy) than paths from the experimental packing of Figure 3.1. Otherwise, the behavior is remarkably similar, sustained rotation is present and angular excursions are of the same order of magnitude.

In numerical simulations the acceleration Γ of the bottom is perfectly defined. This means the uncertainty around Γ values present in the experiments does not exist in the simulations. The straightforward approach of averaging velocities for the same value of Γ can be used.

Figure 3.6, top, shows the mean squared rotational velocity $\langle\bar{\omega}^2\rangle$, averaged from all packings, versus the bottom acceleration Γ. The same average is shown in Figure 3.6, bottom, on log-log scale. The behavior of $\langle\bar{\omega}^2\rangle$ in the log-log plot can be separated in three distinct regions, two regions with power law scaling, and a last region where $\langle\bar{\omega}^2\rangle$ decreases towards zero. For the first region, within $0 < \Gamma < 0.8$, least-squares fits a line with slope of $k = 3.85$, suggesting the same scaling $\langle\bar{\omega}^2\rangle \propto \Gamma^4$ as in the first region in the regression for the experiments (see Figure 3.2).

For the second region, within $1 < \Gamma < 10$, the scaling is assumed to take the form $(\langle\bar{\omega}^2\rangle - \omega_c) \propto (\Gamma - \Gamma_c)^k$, where $\Gamma_c = 1$ is the critical acceleration at which the first regime transition takes place, and ω_c is the mean rotational velocity at Γ_c. Regressing $(\langle\bar{\omega}^2\rangle - \omega_c)$ against $(\Gamma - \Gamma_c)$, using least squares, fits a line with slope $k = 0.99$, suggesting the scaling

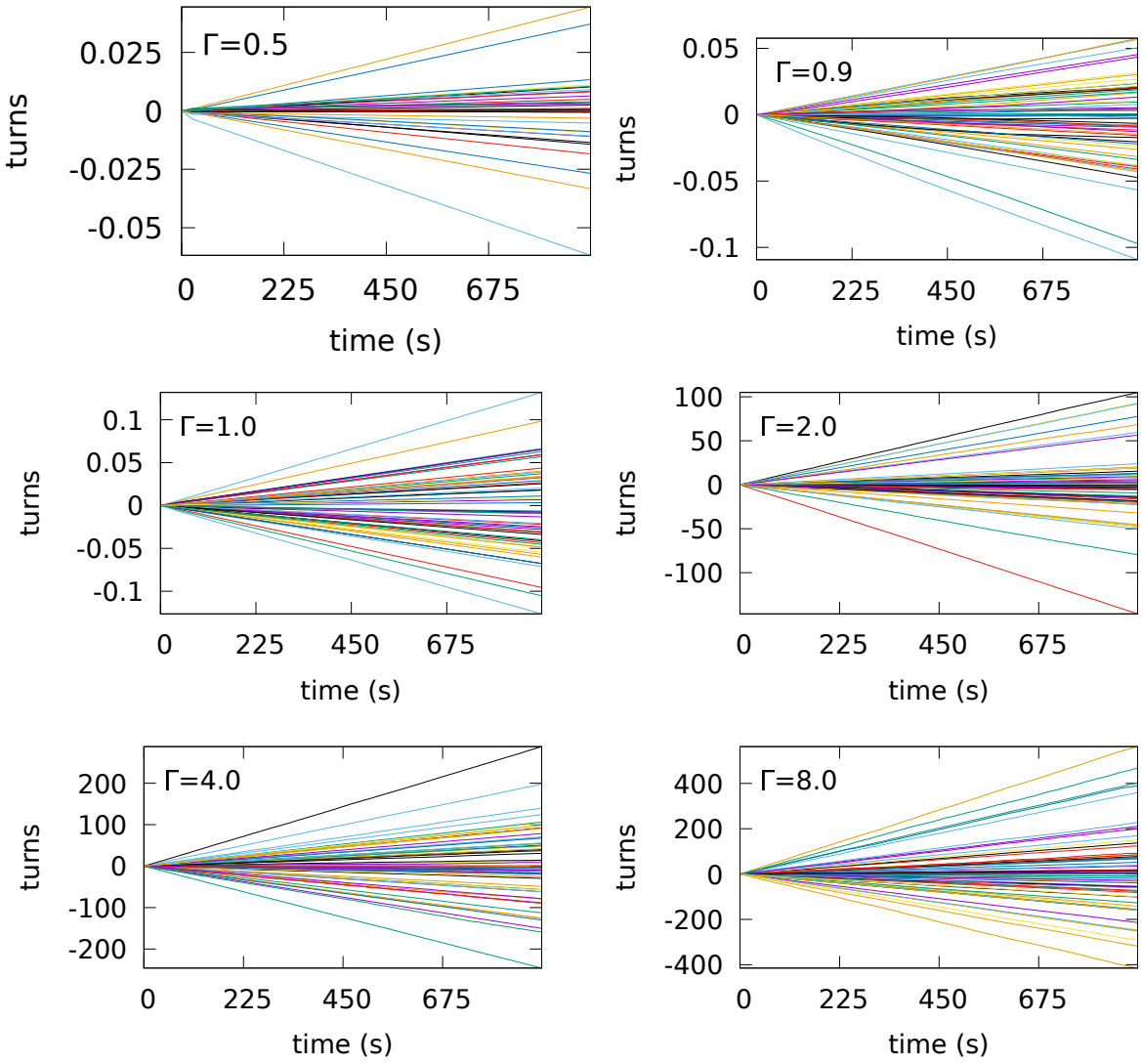

Figure 3.5: Angular paths for each of the disks of a packing simulated with MD. Each plot corresponds to a different bottom excitation Γ.

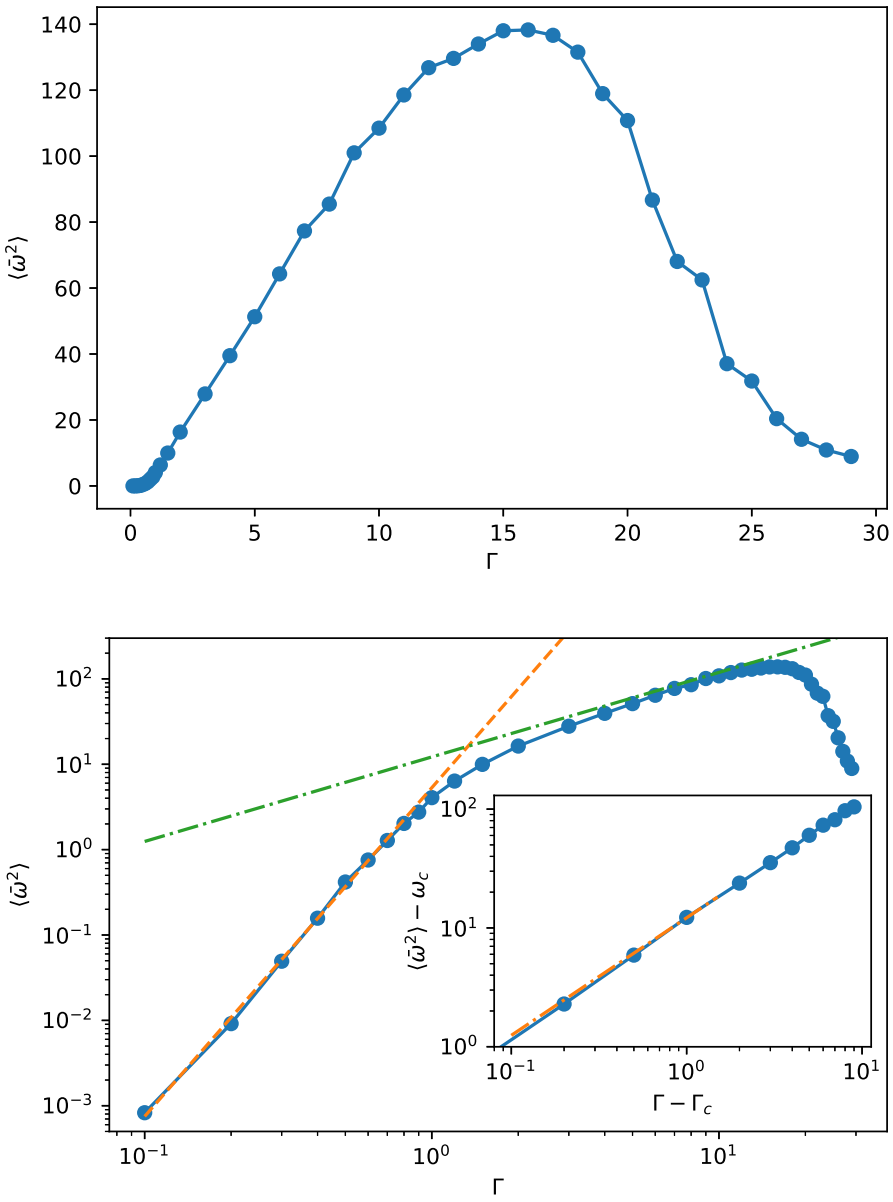

Figure 3.6: Mean squared rotational velocity $\langle\bar{\omega}^2\rangle$, averaged from all MD simulated packings, versus the bottom acceleration Γ. Top: Linear scale plot. Bottom: log-log plot. The dashed line is a least-squares regression line with slope 3.85. The dot-dashed is the result of the least-squares regression of $(\langle\bar{\omega}^2\rangle - \omega_c)$ against $(\Gamma - \Gamma_c)$, with $\Gamma_c = 1$. It has a slope of 0.99. Velocity is measured in revolutions per minute RPM. The insert of the bottom plot shows a restricted interval from $\Gamma = 1$ to 10 where the linear fit is shown in the correct variables $(\langle\bar{\omega}^2\rangle - \omega_c)$ against $(\Gamma - \Gamma_c)$.

$\langle \bar{\omega}^2 \propto \Gamma \rangle$. Again, this is the same scaling as that of the second region in the regression for the experiments. The same scaling transition is observed in numerical simulations, a remarkable result that gives confidence that the mechanism that causes rotation in real packings is reproduced in numerical simulations.

At $\Gamma \approx 10$, $\langle \bar{\omega}^2 \rangle$ starts to decrease. This third region is not observed in the experiments with real packings, since the experimental apparatus is unable to reach a large enough bottom acceleration. When vibration becomes large ($\Gamma > 10$), the packing network geometry starts to fluctuate. This increases the probability of packing rearrangements. If the rate of rearrangements is high, disks may start to diffuse throughout the packing. The local contact configuration of each disk is no longer constant, causing larger velocity fluctuations and, in turn, causing the magnitude of the mean rotational velocity $\bar{\omega}$ of each disk to decrease. If we would continue to increase Γ further, we would enter the regime of granular gases. For a granular gas, there is no local left-right asymmetry due to packing structure, and we expect $\bar{\omega}$ to vanish for all disks.

The mean correlation coefficient $\left\langle \rho^2_{\theta_t} \right\rangle$ and the mean adjusted deviation $\langle \sigma_a \rangle$, averaged over all simulated packings, are shown in Figure 3.7 plotted against the bottom acceleration Γ. Similarly to what happens for the experimental packings, for low bottom acceleration values, $\left\langle \rho^2_{\theta,t} \right\rangle$ increases and $\langle \sigma_a \rangle$ decreases. At $\Gamma \approx 1$, the correlation coefficient reaches a maximum of $\left\langle \rho^2_{\theta,t} \right\rangle \approx 1$, while the mean deviation reaches a minimum of $\langle \sigma_a \rangle \approx 0.2$. Note that the bottom acceleration Γ, at which both quantities reach an extremum, is the critical acceleration $\Gamma_c = 1$, at which the scaling transition for $\langle \bar{\omega}^2 \rangle$ occurs (see Figure 3.6). The appearance of the extrema indicates, again, a regime transition near $\Gamma_c = 1$. For $\Gamma > 1$, $\left\langle \rho^2_{\theta,t} \right\rangle$ monotonically decreases, while $\langle \sigma_a \rangle$ monotonically increases. The increase (decrease) of $\left\langle \rho^2_{\theta,t} \right\rangle$ ($\langle \sigma_a \rangle$) signals an decrease in the linearity of angular paths, i.e., an increase of velocity fluctuations.

The same three regions that we identified when discussing the behavior of $\langle \bar{\omega}^2 \rangle$ (Figure 3.6) can be distinguished from the behavior of $\left\langle \rho^2_{\theta,t} \right\rangle$ in the log-log plot of Figure 3.7 (bottom): A first region, between $0 < \Gamma < 1$, where $\left\langle \rho^2_{\theta,t} \right\rangle$ increases, and disks in the packing pass gradually from non-rotating to rotating as Γ increases. The region between $1 < \Gamma < 10$, where $\left\langle \rho^2_{\theta,t} \right\rangle$ decreases linearly in the log-log plot. In this middle region, most disks are rotating and the packing structure is stable. Finally, the third region, for $\Gamma > 10$,

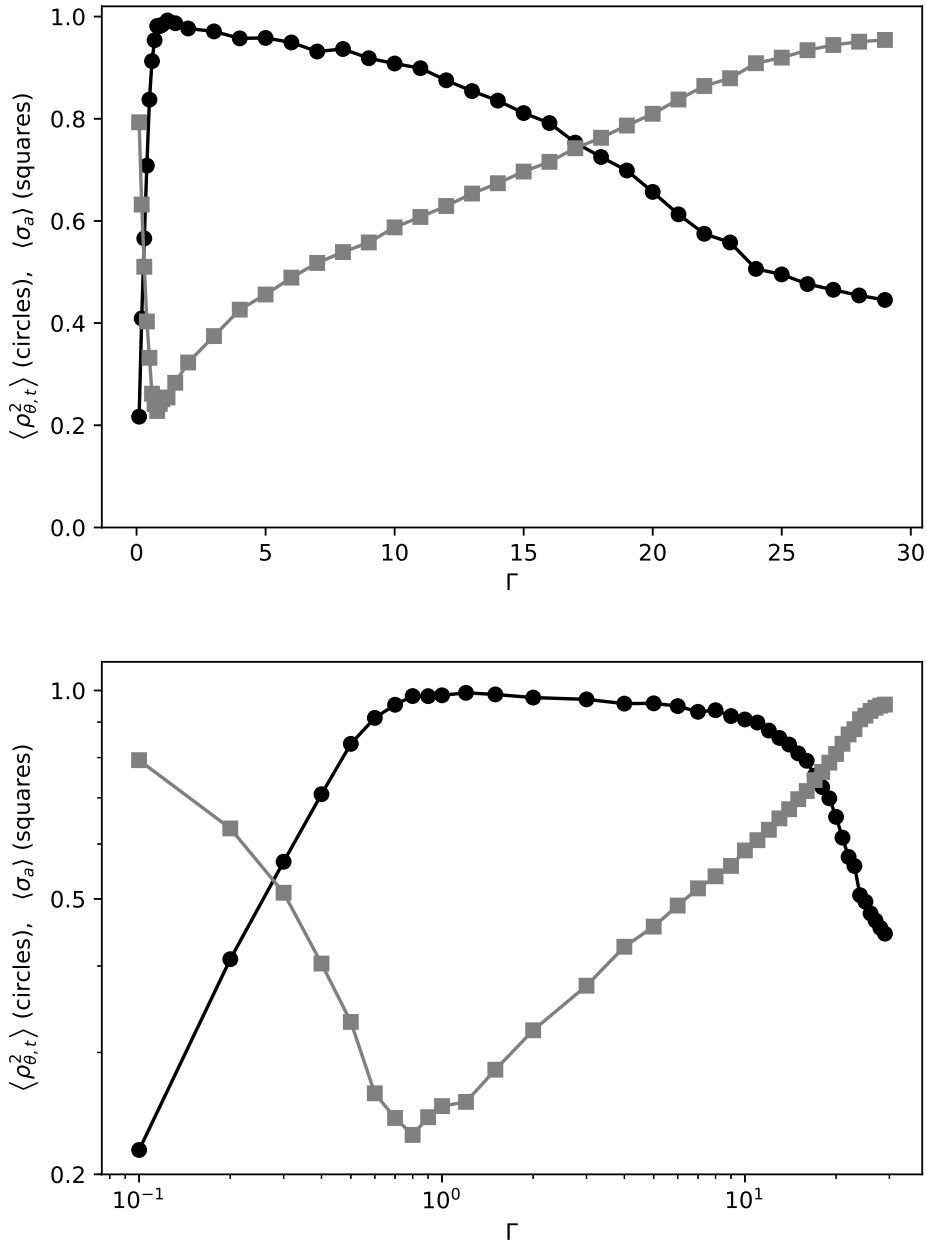

Figure 3.7: The mean correlation coefficient $\langle \rho^2_{\theta,t} \rangle$ (circles), and the adjusted standard deviation σ_a (squares), averaged from all MD simulated packings. Top: Linear scale plot. Bottom: Logarithmic scale plot. The increase (decrease) of $\langle \rho^2_{\theta,t} \rangle$ (σ_a) are interpreted as increased fluctuations in the rotational velocities of the disks within the packing. Both quantities display scaling transitions at $\Gamma \approx 1$ and $\Gamma \approx 10$, delimiting regions at which the packing is in distinct states. The first state is dominated by persistent contacts. The second state is dominated by collisions, but the packing structure is stable. In the last region the packing has become fluidized.

marked by an abrupt decline of $\langle \rho^2_{\theta,t} \rangle$ in the log-log graph. In this final region, the packing structure is becoming increasingly unstable due to large amplitudes of vibration. In this third region the packing is becoming fluidized, in the sense that disks start to diffuse.

Disk transport is actually possible even in the other two regions, where sub-diffusion is promoted by spontaneous packing rearrangements. Even if spontaneous rearrangements occur rarely, as long as the probability of rearrangement is not zero, it is possible that sub-diffusion may be observed at large time scales. However, for the time scales considered in this work, this is not the case.

Probability density histograms of $\rho^2_{\theta,t}$ for four values of Γ are shown in Figure 3.8. For $\Gamma = 0.3$, we can again distinguish between a group of non-rotating disks (low $\rho^2_{\theta,t}$) and a group of rotating disks (high $\rho^2_{\theta,t}$). An example of the distribution in the region where most disks are rotating ($1 < \Gamma < 10$) is given in the histogram for $\Gamma = 4$, where all disks have large values of $\rho^2_{\theta,t}$. For the region with $\Gamma > 10$, where the packing becomes unstable, a group of non-rotating disks appears again (high bar near 0 for the histograms with $\Gamma = 20$ and $\Gamma = 29$). In this final region, the separation between groups of rotating and non-rotating disks is less clear, likely due to increased velocity fluctuations caused by the packing instability. An important number of disks now have $\rho^2_{\theta,t}$ values in between 0 and 1. For $\Gamma = 29$, no disk seems to be rotating, because there is no peak near one. For vibration amplitudes this large, velocity fluctuations start to dominate, disks are diffusing, and the mean rotational velocity is expected to vanish.

To explore the effect of the normal stiffness on the mean squared velocity $\langle \bar{\omega}^2 \rangle$, we performed additional simulations with stiffness values of $k_n = 1e5$ and $k_n = 1e6$. Curves for $\langle \bar{\omega}^2 \rangle$ for the original simulations and simulations with the new stiffness values are shown in Figure 3.9, in both linear scale (top) and logarithmic scale (bottom). Generally, the mean rotational velocity decreases with increasing k_n, the difference being of several order of magnitude in the region with $\Gamma < 1$. The exception being a small vibration interval, just before $\Gamma = 1$, where disks with $k_n = 1e5$ rotate faster than the others. It is likely that this is a numerical error, since the MD integration algorithm we use fails at high stiffness values [36]. The stiffer the disks, the sooner they start bouncing against each other with increasing Γ. For very stiff particles, we expect this to happen very close to $\Gamma = 1$, where the bulk of the packing starts to loose contact with the vibrating bottom. As we increase

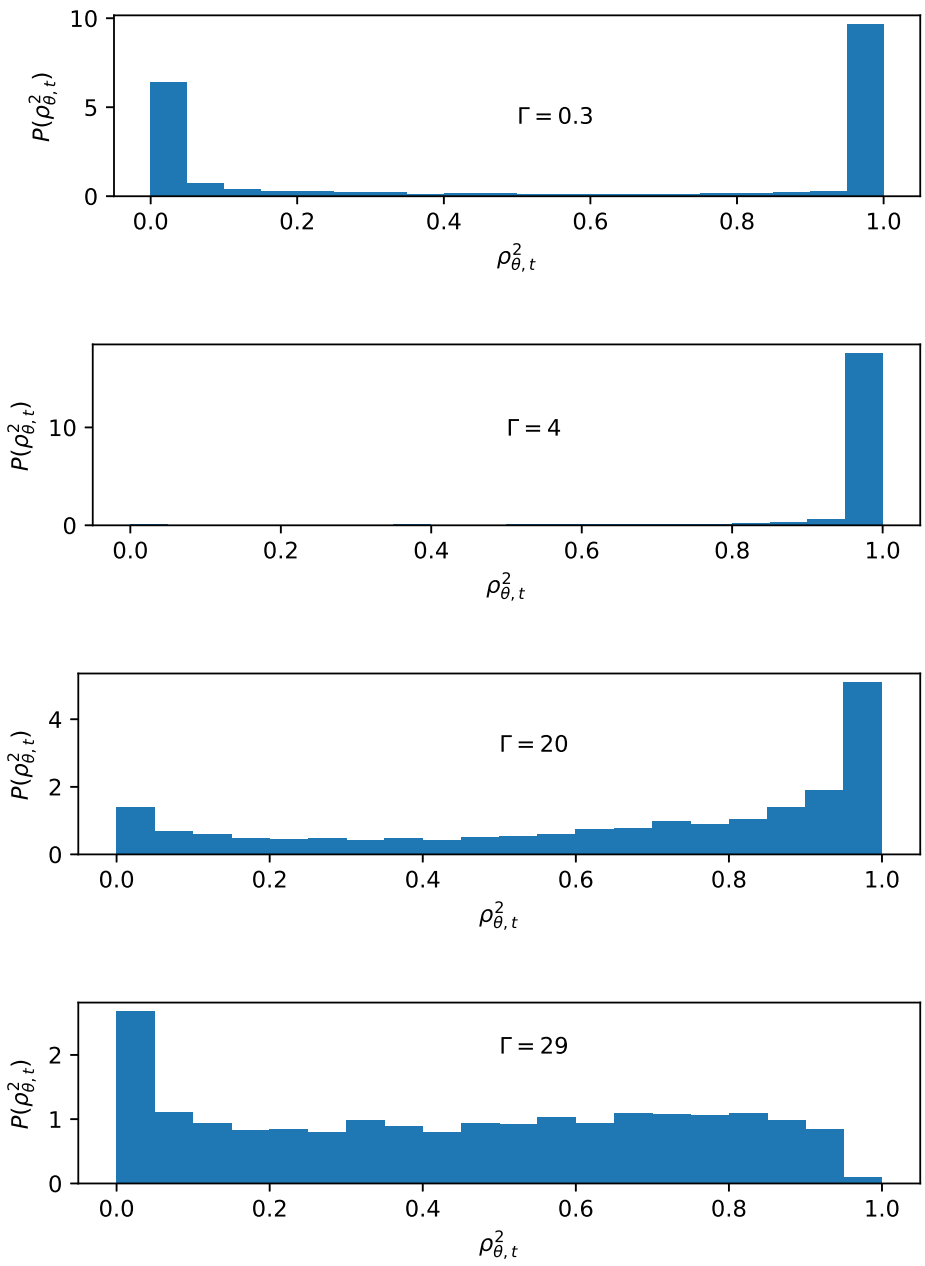

Figure 3.8: Probability density histograms of the correlation coefficient $\rho^2_{\theta,t}$ from 100 MD simulated packings with the same value of Γ. Histograms for $\Gamma = 0.3$, $\Gamma = 4$, $\Gamma = 20$, and $\Gamma = 29$ are shown. The histogram for $\Gamma = 0.3$ shows a concentration of disks with highly noisy angular paths corresponding to values of $\rho^2_{\theta,t}$ near zero, and another concentration of disks with linear angular paths corresponding to values of $\rho^2_{\theta,t}$ near one. For $\Gamma = 4.0$ practically all disks have values of $\rho^2_{\theta,t}$ near 1, corresponding to almost linear angular paths. For $\Gamma = 20$ disks with noisy paths appear again. Finally, for $\Gamma = 29$, there are practically no disks with $\rho^2_{\theta,t}$ close to 1, there is more homogeneous distribution among intermediate values of $\rho^2_{\theta,t}$, with a large concentration near $\rho^2_{\theta,t} = 0$.

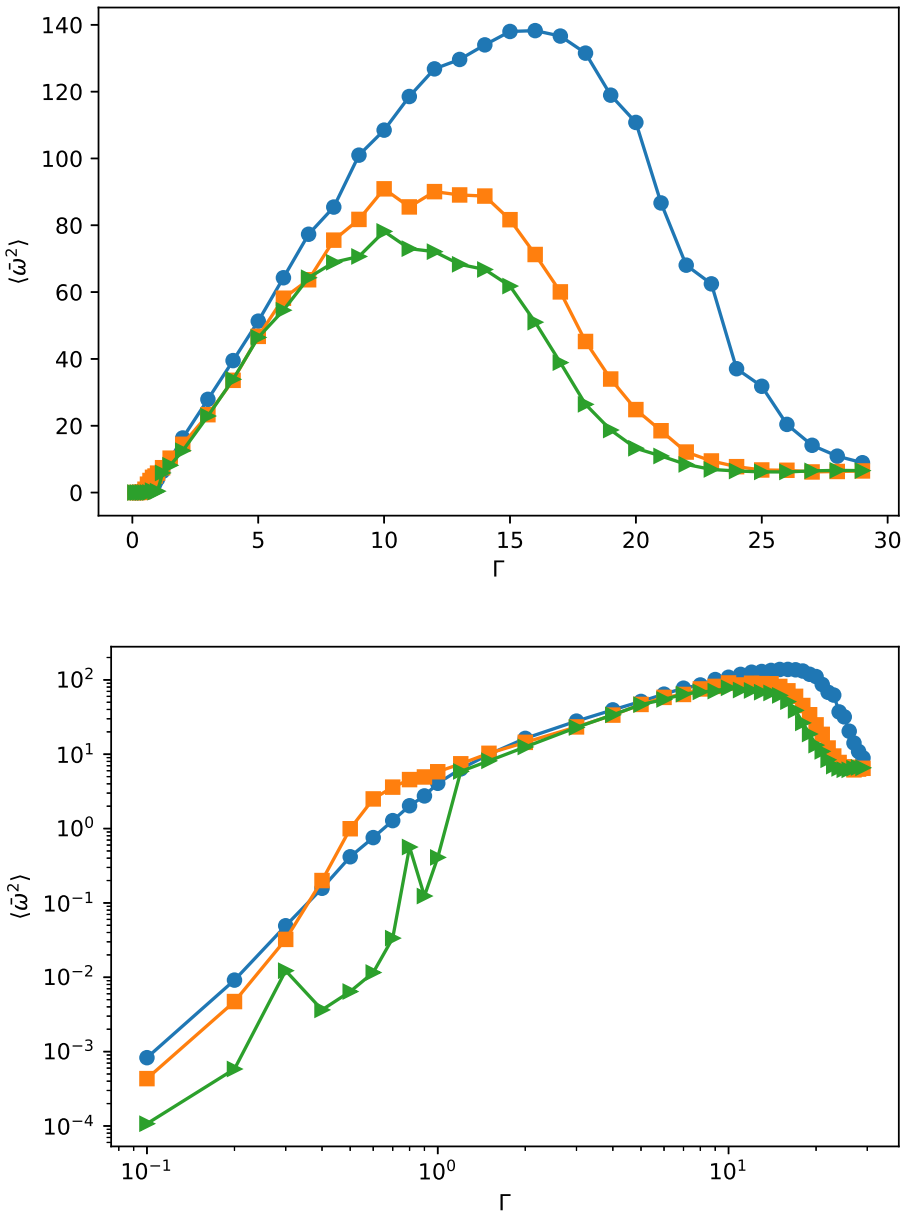

Figure 3.9: Mean squared rotational velocity $\langle\bar{\omega}^2\rangle$ versus Γ, averaged from MD simulated packings. Three curves for three different values of normal stiffness k_n are shown. Stiffness values are: $k_n = 10^4$ (circles), $k_n = 10^5$ (squares), and $k_n = 10^6$ (triangles). Other parameters are: stiffness ratio $k_r = 0.77$, normal viscous coefficient $\gamma_n = 0.1$, friction coefficient $\mu = 0.1$ and material surface density $\rho = 3.57$ kg/m^2.

Γ beyond 1, particles spend very little time in contact, and interactions between them are mainly due to binary collisions. This regime is further explored in the next section using Event-Driven simulations.

3.3 Event Driven Simulations

Event-driven simulations are only used to simulate packings vibrated with $\Gamma \geq 2$. As described in Section 2.3, in ED simulations, collisions are instantaneous, and lasting contacts between disks are impossible. It would not make sense to use ED algorithms to simulate gently vibrated packings, where we expect disks to remain in contact for long times. Furthermore, for $\Gamma < 2$, particle density increases. In dense packings, the mean time between collisions becomes smaller, increasing the number of collisions that need to be simulated. This causes CPU time to become prohibitively large. Also, for dense packings, the probability of numerical artifacts (inelastic collapse, for example) appearing during the simulation becomes important.

For $\Gamma \geq 2$, ED simulations are a powerful technique to numerically study rotations in disk packings. As Γ increases, and the collision rate decreases, CPU time required for the simulation sharply decreases as compared to MD. For high values of Γ, a reduction of several orders of magnitude is achieved. However, since lasting contacts are impossible in ED simulations, these methods will only yield useful results when the system is in a regime where the contribution to rotation from lasting contacts is negligible. To be sure that effects from lasting contacts can be ignored, ED simulations must be validated against MD simulations. All numerical results in this section are obtained from simulations with the following parameters: stiffness ratio $k_r = 0.77$, normal viscous coefficient $\gamma_n = 0.1$, friction coefficient $\mu = 0.1$ and material surface density $\rho = 3.57$ kg/m^2.

Figure 3.5 shows plots of the angular path θ for each of the disks belonging to one ED simulated packing subject to different vibration amplitudes Γ. For all Γ, velocity fluctuations are not appreciable at this scale and all paths look linear. All disks rotate with near constant velocity, similarly to disks in MD simulated packings (see Figure 3.5). Partial packing reorganization occurs for values of $\Gamma = 2$ and $\Gamma = 8$, leading to a velocity change for some disks.

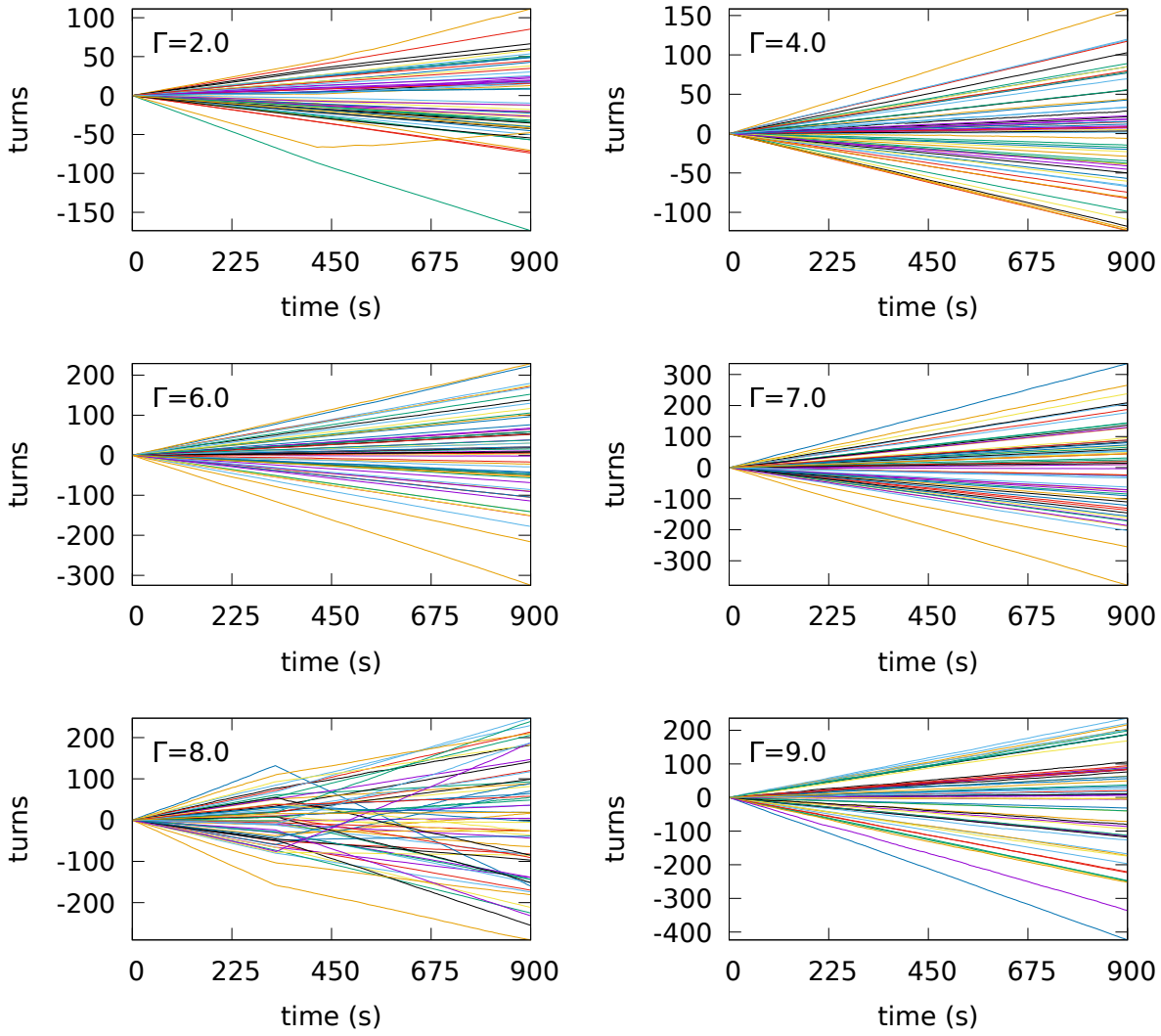

Figure 3.10: Angular paths for each of the disks of a packing studied by ED simulations. Each plot corresponds to a different bottom excitation Γ.

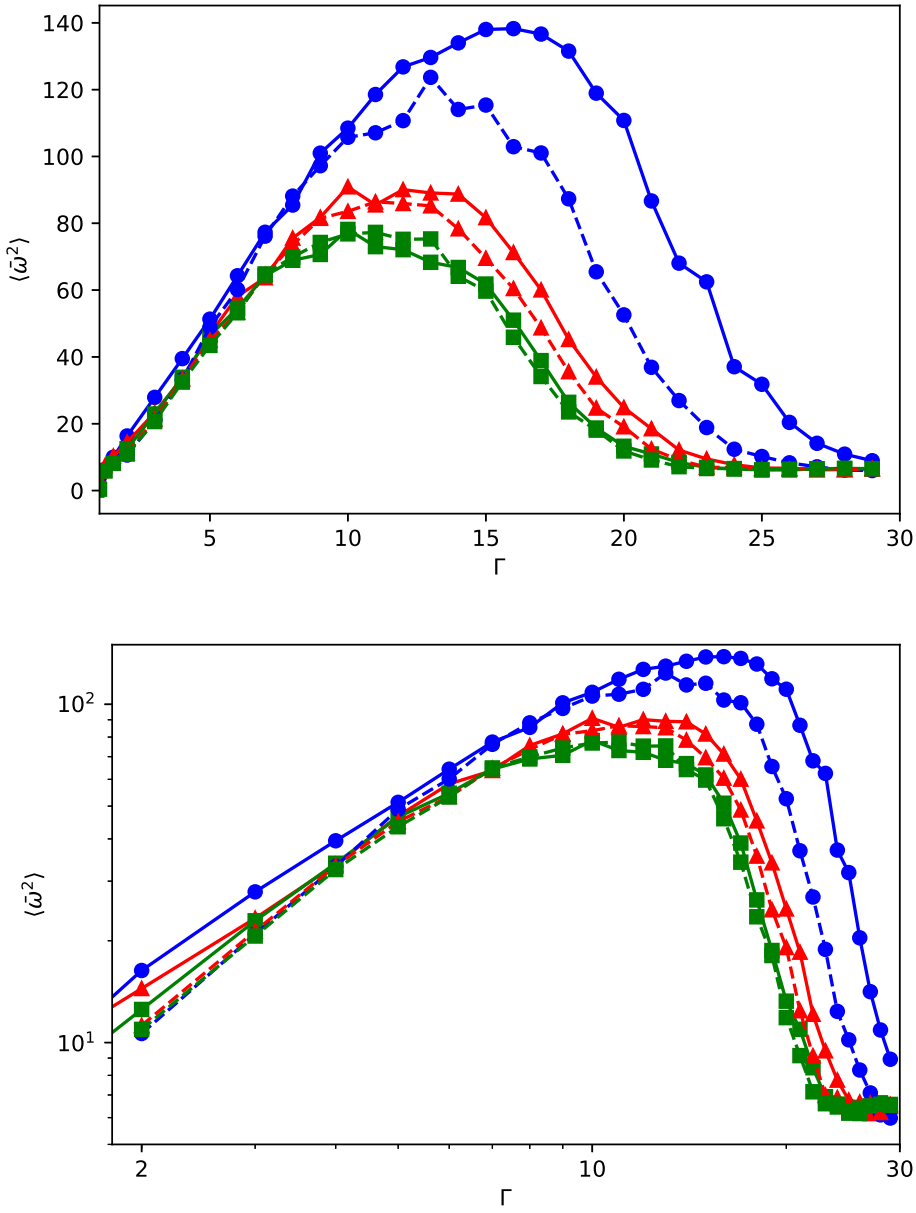

Figure 3.11: Mean squared rotational velocity $\langle\bar{\omega}^2\rangle$, as a function of Γ, averaged from 100 different packings. Top: Linear scale. Bottom: log-log scale. Full lines correspond to MD simulations and dashed lines to ED simulations. Different symbols correspond to different values of the normal stiffness k_n: Circles for $k_n = 10^4$, triangles for $k_n = 10^5$, and squares for $k_n = 10^6$. The coincidence between MD and ED gets better for increasing stiffness, as is expected, since at large stiffness values the duration of collisions decreases.

The mean squared rotational velocity $\langle \bar{\omega}^2 \rangle$, averaged over 100 different packings, is plotted against Γ in Figure 3.11, both using a linear scale (top) and a logarithmic scale (bottom). Both MD and ED numerical simulations for different values of k_n are plotted to allow a direct comparison from both methods. Full lines correspond to MD simulations and dashed lines to ED simulations. Different symbols correspond to different values of the normal stiffness k_n: Circles for $k_n = 10^4$, triangles for $k_n = 10^5$, and squares for $k_n = 10^6$. There is a good degree of coincidence between the results from these two methods in the region of parameters in which both can be used ($\Gamma > 2$). The fact that rotations in disk packings can be reproduced using ED simulations means that, for $\Gamma \gtrapprox 2$, it is enough to consider instantaneous collisions when studying the origin of rotation. We will take advantage of this in Chapter 6, when studying rotations in a simplified system.

4 A minimal packing to study rotations: The 3-disk setup

In Chapter 3, we have reported the appearance of sustained rotation in packings with a large number of disks. To develop a better understanding of the origin of rotation, it is convenient to study a simpler system, with the minimum number of disks that still display rotation. In a reduced system, it is easier to isolate interactions among disks, and analyze their effects on the rotational velocity.

The minimal setup to study spontaneous rotation consists of a single disk supported against gravity by two contacts. This setup may consist of three disks of the same radius R, or of a disk on a wedge. The 3-disk setup relates more closely to disk packings, while the wedge has the advantage that contact angles are always constant, simplifying the analysis under certain conditions. The supporting element (wedge or disk) vibrates around its equilibrium position, engaging in energy and momentum transfer with the upper disk. This setup may be regarded as the simplest granular packing that can be studied [37]. In this chapter, we introduce this minimal packing, together with a model of inter-particle forces. Results from this section are used in Chapter 5 to study rotation under the condition of persistent contacts between disks, and in Chapter 6 to study rotation when the upper disk bounces off the supporting element.

4.1 Notation

The relevant notation for a system of three disks is shown in Figure 4.1 (left). Contacts are labeled $i = 1$ (left disk) and $i = 2$ (right disk). The angle between contacts is $\alpha_{12} = 2\theta_0$. If all radii are equal, and all disks are touching, $\theta_0 = \pi/6$. The angle between gravity and

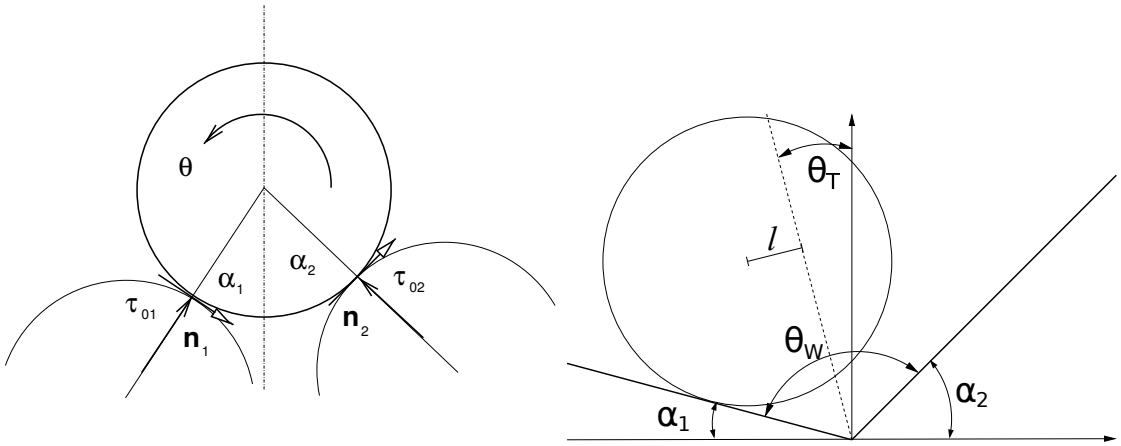

Figure 4.1: The 3-disk setup showing the definition of angles and the direction of normal n and tangential τ forces (left). A disk on a wedge showing the same angles α_i, the tilt angle θ_T, the wedge aperture θ_w and the distance l from the disk center to the wedge bisector (right).

contact i is called α_i. When gravity makes an angle θ_T with the bisector of the contacts, one has that $\alpha_1 = \theta_0 - \theta_T$ and $\alpha_2 = \theta_0 + \theta_T$, these angles are, therefore, not equal. The notation for the wedge is shown in Figure 4.1 (right). Angles α_i are the same as for the 3-disk setup and θ_w defines the wedge aperture. Upon excitation (e.g. vibration of the supporting disks) the upper disk is seen to rotate spontaneously, in a direction that depends on the tilting angle θ_T, as well as on other parameters, such as the amplitude of excitation.

Direction of normal n and tangential τ forces are also shown in Figure 4.1. The details of the force model are discussed in the following section.

4.2 Forces between disks

A wide variety of proposals have been put forward [20–22, 38–40] to describe frictional forces between elastic bodies. Tangential forces τ are typically dependent upon normal forces n, mainly through the Amonton condition, which limits frictional forces so that $|\tau| \leq \mu n$, where μ is the friction coefficient.

Several previous studies of gravitational billiards used heavily simplified tangential force models. This was justified because rotational motion was not investigated in detail in those

works, but introduced mainly as a source of energy dissipation. Gorski and Srokowski [41] simply apply the same coefficient of restitution to both the normal and tangential components of the relative velocity. Hart et al. [42] employed a simplified tangential force model considering two cases: the no-slip case, which gives rise to rolling motion, and the sliding case, where the tangential force is assumed to always lie at the limit value given by Amonoton's condition. Kurggel-Emden et al. [40] reviewed a variety of linear and non-linear tangential-force models and compared numerical simulations of binary collisions to experimental results. In a similar study, Di Renzo and Maio [38] concluded that, regarding the value of post-collision velocities, there is no significant improvement by considering non-linear models over linear ones.

Rotation in disk packings originates from tangential forces between disks. To observe this rotation in simulations, we require a force model that reproduces key aspects of tangential forces in real systems, but are simple enough to allow for analytic treatment. When not limited by the Amonton condition, we have chosen to implement forces that depend linearly on the relative position of the disks in contact. Our choice, linear elastic forces, implemented as described in this section, is able to reproduce the statistical properties of rotation in large experimental packings (see Chapter 3).

4.2.1 Normal forces

We assume linear elasticity for the normal force $\vec{n}$ between two disks with centers at $\vec{r}_a$ and $\vec{r}_b$ with radii R_a and R_b. Defining $\delta = (R_a + R_b) - |\vec{r}_b - \vec{r}_a|$, one has

$$\vec{n} = \hat{n}_{ab} \left(k_n \delta - \gamma_n u_n \right), \tag{4.1}$$

where $\hat{n}_{ab}$ is the normal versor, k_n is the compressive elastic constant, γ_n is a viscous constant, and u_n is the normal relative velocity (any sign) between disks. Notice that (4.1) can become negative for two disks that are still closer than the sum of their radii, if they are moving appart from each other fast enough, because in this case the contribution from the viscosity term is negative. Not correcting for this would be unphysical, since, by definition, normal forces can only be compressive. In a correct implementation of visco-elastic forces,

one thus replaces (4.1) with

$$\vec{n} = \hat{n}_{ab} \max\left(k_n\delta - \gamma_n u_n,\ 0\right). \tag{4.2}$$

The physical meaning of this "cutoff" is easy to explain. When two visco-elastic disks that are compressed toghether start to move apart, it takes a certain time for them to expand and regain their original shape. Therefore, if their (negative) relative velocity is large enough, they can become detached from each other (their normal force becomes zero) even before the distance between their centers becomes larger than the sum of their radii.

4.2.2 Tangential forces

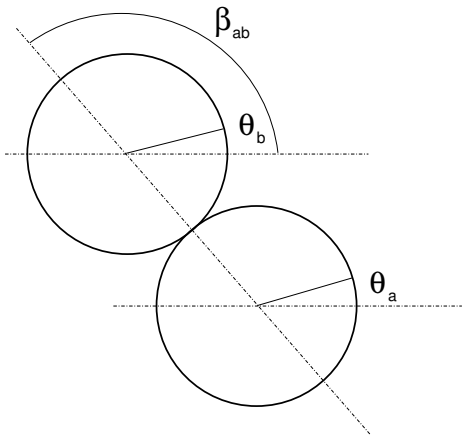

Figure 4.2: Two disks in contact showing the definition of angles used to calculate the relative tangential displacement (λ_{ab}).

Our model for tangential forces derives from one originally proposed by Cundall and Strack [22, 43]. An "elastic skin" with tangential stiffness k_t accounts for tangential forces at each closed contact. The tangential force is

$$\vec{\tau} = -k_t\delta_t\hat{t}_{ab}, \tag{4.3}$$

where $\vec{t}_{ab}$ is the tangential versor, δ_t is the accumulated tangential relative displacement between disks, in the direction of the tangential versor. This is defined as the time integral of the relative tangential velocity of the surfaces in contact

$$\delta_t = \int_{t_0}^{t} u_t dt, \tag{4.4}$$

where t_0 is the time at which the contact is first establised. The total tangential force is limited by the Amonton condition $|\tau| \leq \mu n$. If the Amonton condition would be violated, δ_t is modified in order to keep the total tangential force right at the frictional limit. This modification represents the dissipative loss of elastic energy stored in the "elastic skin", i.e. the particle's skin "slips" whenever Amonton's limit is reached.

Direct calculation of δ_t

A naive numerical implementation of (4.4), e.g. in molecular dynamics, requires one to integrate the tangential velocity step-wise in time. In situations such as ours, in which there may be oscilatory tangential motion over long times, this procedure is markedly error-prone due to roundoff accumulation when δ_t oscilates back and forth through zero. Additionally, there is some small amount of unavoidable error implied by the fact that the tangential velocity is approximated by a series of steps.

We have therefore implemented the an alternative, less error-prone, procedure. It allows one to calculate δ_t exactly, directly from the knowledge of particle coordinates at time t, plus one (for disks, two for spheres, etc.) additional quantity that is determined at the time when the particles first make contact.

Let θ_a be the angular coordinate of a disk a. Upon general rotations and displacements of their centers, the *relative tangential displacement* λ_{ab} of two disks a and b in contact (See Fig. 4.2) is given by

$$\lambda_{ab} = R_a\theta_a + R_b\theta_b - \beta_{ab}(R_a + R_b), \tag{4.5}$$

where R is the radius of a disk and β_{ab} is the angle made by the line that joins the centers of the disks in contact with the x-axis. Notice that λ is constant for two disks that roll on

each other rigidly (without deformation of the skin) and without slippage.

Assume that, when two disks are put in contact, their relative tangential coordinate equals λ^*. If these disks are now moved slightly with respect to each other, producing a change in λ (without slip), tangential forces will develop. Tangential forces in our model were already defined to depend linearly on the deformation of the skin [22], that is:

$$\tau = k_t(\lambda - \lambda^*), \tag{4.6}$$

where we have assumed that no skin "slippage" has occurred as a consequence of the tangential deformation. Therefore λ^* still has the value that was defined at first contact. When the tangential force is large enough so as to violate Amonton's condition, the skin "slides" or "slips". This is represented, in our implementation, by a change in λ^* for that contact, so as to maintain $|\tau|$ at its maximum possible value, which is given by μn.
By way of example, assume that the Amonton condition is violated, resulting in $-\mu n > k_t(\lambda - \lambda^*)$. In this case, one redefines $\lambda^* = \lambda + \mu n/k_t$, such that the equality $-\mu n = k_t(\lambda - \lambda^*)$ is restored. If, on the other hand, the violation of the Amonton condition is such that $k_t(\lambda - \lambda^*) > \mu n$, one redefines $\lambda^* = \lambda - \mu n/k_t$ so as to have $k_t(\lambda - \lambda^*) = \mu n$.

When a disk belonging to a packing touches the walls of the container, or when considering the system of a disk in a wedge (Chapter 6), the contact is between a disk (a) and a wall (w), instead of between two disks. In this case, we calculate the relative tangential displacement as

$$\lambda_{aw} = R_a\,(\theta_a - \beta_{aw}) + d_{aw}, \tag{4.7}$$

where β_{aw} is the angle of the line perpendicular to the wall that passes through the center of the disk, and d_{aw} is the distance from a reference point in the wall to the contact point. When considering the wedge, it is convenient to choose its vertex as the reference point.

Auxiliary coordinates $\delta\theta$ and Θ

Consider now a disk 0 with radius R_0, supported against gravity by two contacts 1 and 2, as shown in Figures 4.1. Tangential forces on disk 0 are written:

$$\tau_{01} = -\, k_t \left(\lambda_{01} - \lambda^*_{01}\right) \stackrel{\text{def}}{=\!=} -k_t R_0 \left(\theta - \hat{\theta}_{01}\right) \tag{4.8}$$

$$\tau_{02} = -\, k_t \left(\lambda_{02} - \lambda^*_{02}\right) \stackrel{\text{def}}{=\!=} -k_t R_0 \left(\theta - \hat{\theta}_{02}\right). \tag{4.9}$$

When the contact is with a disk, we define

$$\hat{\theta}_{0i} = \theta^*_0 - \frac{R_i}{R_0}(\theta_i - \theta^*_i) + \frac{R_0 + R_i}{R_0}(\beta_{0i} - \beta^*_{0i}). \tag{4.10}$$

Alternatively, when contact is with a wall, the definition of $\hat{\theta}_{0i}$ is

$$\hat{\theta}_{0i} = \theta^*_0 + (\beta_{0i} - \beta^*_{0i}) - \frac{d_{0i} - d^*_{0i}}{R_0}. \tag{4.11}$$

In (4.10) and (4.11), quantities superscripted with an $*$ are measured when the contact is closed for the first time, and are modified by slips during the time evolution of the system.

The torque acting on the disk is:

$$\mathcal{T} = R_0 \left(\tau_{01} + \tau_{02}\right) \stackrel{\text{def}}{=\!=} -2R_0^2 k_t (\theta - \theta_{eq}), \tag{4.12}$$

where we have used equations (4.8) and (4.9), and defined the static equilibrium angle as

$$\theta_{eq} = \frac{\hat{\theta}_{01} + \hat{\theta}_{02}}{2}. \tag{4.13}$$

We further define the skin "stretch" Θ as

$$\Theta = \frac{\hat{\theta}_{02} - \hat{\theta}_{01}}{2}, \tag{4.14}$$

which measures how much the "elastic skin" is stretched in equilibrium, and the departure

from equilibrium $\delta\theta$ as

$$\delta\theta = \theta - \theta_{eq}. \tag{4.15}$$

In terms of Θ and θ_{eq} one can now write

$$\begin{cases} \tau_{01} = & -k_t R_0(\Theta + \delta\theta) \\ \tau_{02} = & k_t R_0(\Theta - \delta\theta) \end{cases} \tag{4.16}$$

$$\begin{cases} \Theta = & (\tau_{02} - \tau_{01})/2k_t R_0 \\ \delta\theta = & -(\tau_{02} + \tau_{01})/2k_t R_0 \end{cases} \tag{4.17}$$

Notice that the total torque $\mathcal{T}$ (4.12) depends on $\delta\theta$ but not on Θ.

$$\mathcal{T} = R_0\left(\tau_{01} + \tau_{02}\right) = -2R_0^2 k_t \delta\theta \tag{4.18}$$

The stretch Θ, on the other hand, does not depend on θ as long as there are no slippages, it is determined by the movement of the supports. Θ determines the residual tangential forces, obtained when $\delta\theta = 0$. If $\Theta > 0$, according to (4.16), $-\tau_{01} + \tau_{02} > 0$ and this means that the residual forces "pull" on the disk slightly upwards (their vertical component is directed upwards). A negative stretch, on the other hand, means that the residual forces "push" the disk downwards.

4.3 Equations of motion

In the following we use the notation (Refer to Fig. 4.1):

$$s_i = \sin(\alpha_i), \tag{4.19}$$

$$c_i = \cos(\alpha_i), \tag{4.20}$$

$$s_{12} = \sin\left(\alpha_1 + \alpha_2\right) = \sin(2\theta_0), \tag{4.21}$$

$$c_{12} = \cos\left(\alpha_1 + \alpha_2\right) = \cos(2\theta_0), \tag{4.22}$$

If $\ddot{x}$ and $\ddot{y}$ are the linear accelerations of the upper disk, m its mass and g the acceleration due to gravity, Newton's equations for the x and y directions read

$$n_{01}s_1 - n_{02}s_2 + \tau_{01}c_1 + \tau_{02}c_2 = m\ddot{x} \tag{4.23}$$

$$n_{01}c_1 + n_{02}c_2 - \tau_{01}s_1 + \tau_{02}s_2 = mg + m\ddot{y}, \tag{4.24}$$

from which one can get the normal forces as:

$$n_{01} = \frac{m\ddot{x}c_2 + (mg + m\ddot{y})s_2}{s_{12}} - \tau_{01}\frac{c_{12}}{s_{12}} - \tau_{02}\frac{1}{s_{12}} \tag{4.25}$$

$$n_{02} = \frac{-m\ddot{x}c_1 + (mg + m\ddot{y})s_1}{s_{12}} + \tau_{01}\frac{1}{s_{12}} + \tau_{02}\frac{c_{12}}{s_{12}}. \tag{4.26}$$

Defining:

$$w_1 = W_1 R_0 k_t = m\ddot{x}c_2 + (mg + m\ddot{y})\, s_2 \tag{4.27}$$

$$w_2 = W_2 R_0 k_t = -m\ddot{x}c_1 + (mg + m\ddot{y})\, s_1, \tag{4.28}$$

we rewrite

$$s_{12}n_{10} = w_1 - \tau_{01}c_{12} - \tau_{02} \tag{4.29}$$

$$s_{12}n_{20} = w_2 + \tau_{01} + \tau_{02}c_{12}. \tag{4.30}$$

4.4 Amonton's condition

Tangential forces τ cannot exceed the limit provided by Amonton's condition:

$$|\tau| \leq \mu n. \tag{4.31}$$

When this condition is violated at a contact, a slippage occurs. This means that one of the $\hat{\theta}_0$ values changes (the skin slips) so that the corresponding tangential force is kept at the limit given by (4.31). Here we have assumed that the static and dynamic friction coefficients are the same. If this were not the case, the value of the tangential force would

need to be adjusted after slipping starts to account for $\mu_{static} \to \mu_{dynamic}$ in (4.31) [20].

Using (4.29) and (4.30), we write Amonton's conditions for contacts 1 and 2 as:

$$\begin{cases} \frac{s_{12}}{\mu}|\tau_{01}| & \leq & w_1 - \tau_{01}c_{12} - \tau_{02} \\ \\ \frac{s_{12}}{\mu}|\tau_{02}| & \leq & w_2 + \tau_{01} + \tau_{02}c_{12}, \end{cases}$$

form which we can extract the four equations

$$-B^{-}\tau_{01} + \tau_{02} \leq w_1 \qquad (\mathbf{a}) \tag{4.32}$$

$$B^{+}\tau_{01} + \tau_{02} \leq w_1 \qquad (\mathbf{b}) \tag{4.33}$$

$$B^{-}\tau_{02} - \tau_{01} \leq w_2 \qquad (\mathbf{c}) \tag{4.34}$$

$$-B^{+}\tau_{02} - \tau_{01} \leq w_2 \qquad (\mathbf{d}), \tag{4.35}$$

where we have defined $B^{\pm} = (\frac{s_{12}}{\mu} \pm c_{12})$. The physical meaning of these inequalities is as follows:

(a) If (4.32) is violated, θ^*_{01} starts to grow, thus increasing τ_{01}. The skin at contact 1 slides counterclockwise (↺).

(b) If (4.33) is violated, θ^*_{01} starts to decrease, thus decreasing τ_{01}. The skin at contact 1 slides clockwise (↻).

(c) If (4.34) is violated, θ^*_{02} starts to decrease, thus decreasing τ_{02}. The skin at contact 2 slides clockwise (↻).

(d) If (4.35) is violated, θ^*_{02} starts to grow, thus increasing τ_{02}. The skin at contact 2 slides counterclockwise (↺).

It is useful to rewrite inequalities (4.32-4.35) in terms of $\delta\theta$ and Θ. Replacing (4.16) into

(4.32-4.35) and defining $C^{\pm\pm} = \frac{s_{12}}{\mu} \pm c_{12} \pm 1$, we have

$$+C^{--}\delta\theta + C^{-+}\Theta \leq W_1 \qquad (\mathbf{a}) \tag{4.36}$$
$$-C^{++}\delta\theta - C^{+-}\Theta \leq W_1 \qquad (\mathbf{b}) \tag{4.37}$$
$$-C^{--}\delta\theta + C^{-+}\Theta \leq W_2 \qquad (\mathbf{c}) \tag{4.38}$$
$$+C^{++}\delta\theta - C^{+-}\Theta \leq W_2 \qquad (\mathbf{d}). \tag{4.39}$$

Let the point where (b) and (c) simultaneously hold as equalities be S_1. Its location is given by

$$\left\{ \begin{array}{lcl} \tau_{01} & = & (B^- w_1 - w_2)/(1 + B^+ B^-) \\ \tau_{02} & = & (w_1 + B^+ w_2)/(1 + B^+ B^-), \end{array} \right. \tag{4.40}$$

or,

$$\left\{ \begin{array}{lcl} \delta\theta^{S_1} & \stackrel{\text{def}}{=\!=} & \frac{(W_1 - W_2)(c_{12}-1) - (W_1+W_2)\frac{s_{12}}{\mu}}{2s_{12}^2(1+1/\mu^2)} \\ & = & -\frac{\mu mg}{2k_t R(1+\mu^2)\cos\theta_0}\left(\left(1 + \frac{\mu\ddot{x}}{g} + \frac{\ddot{y}}{g}\right)\cos\theta_T + \left(\mu - \frac{\ddot{x}}{g} + \frac{\mu\ddot{y}}{g}\right)\sin\theta_T\right) \\ \Theta^{S_1} & \stackrel{\text{def}}{=\!=} & \frac{-(W_1 - W_2)\frac{s_{12}}{\mu} + (W_1+W_2)(1+c_{12})}{2s_{12}^2(1+1/\mu^2)} \\ & = & -\frac{\mu mg}{2k_t R(1+\mu^2)\sin\theta_0}\left(\left(1 + \frac{\mu\ddot{x}}{g} + \frac{\ddot{y}}{g}\right)\sin\theta_T - \left(\mu - \frac{\ddot{x}}{g} + \frac{\mu\ddot{y}}{g}\right)\cos\theta_T\right). \end{array} \right. \tag{4.41}$$

Equivalently, the point S_2 where (a) and (d) intersect each other is located at

$$\left\{ \begin{array}{lcl} \tau_{01} & = & -(B^+ w_1 + w_2)/(1 + B^+ B^-) \\ \tau_{02} & = & (w_1 - B^- w_2)/(1 + B^+ B^-), \end{array} \right. \tag{4.42}$$

or,

$$\left\{ \begin{array}{lcl} \delta\theta^{S_2} & \stackrel{\text{def}}{=\!=} & \frac{(W_1 - W_2)(c_{12}-1) + (W_1+W_2)\frac{s_{12}}{\mu}}{2s_{12}^2(1+1/\mu^2)} \\ & = & \frac{\mu mg}{2k_t R(1+\mu^2)\cos\theta_0}\left(\left(1 - \frac{\mu\ddot{x}}{g} + \frac{\ddot{y}}{g}\right)\cos\theta_T - \left(\mu + \frac{\ddot{x}}{g} + \frac{\mu\ddot{y}}{g}\right)\sin\theta_T\right) \\ \Theta^{S_2} & \stackrel{\text{def}}{=\!=} & \frac{(W_1 - W_2)\frac{s_{12}}{\mu} + (W_1+W_2)(1+c_{12})}{2s_{12}^2(1+1/\mu^2)} \\ & = & \frac{\mu mg}{2k_t R(1+\mu^2)\sin\theta_0}\left(\left(1 - \frac{\mu\ddot{x}}{g} + \frac{\ddot{y}}{g}\right)\sin\theta_T + \left(\mu + \frac{\ddot{x}}{g} + \frac{\mu\ddot{y}}{g}\right)\cos\theta_T\right). \end{array} \right. \tag{4.43}$$

Inequalities (a) and (b) on the other hand hold simultaneously as equalities at D_1 located

at

$$\left\{\begin{array}{lcl}\tau_{01} &=& 0\\ \tau_{02} &=& w_1\end{array}\right. \quad \text{or,} \quad \left\{\begin{array}{lcl}\delta\theta^{D_1} &\stackrel{\text{def}}{=\!=}& -\frac{W_1}{2}\\ \Theta^{D_1} &\stackrel{\text{def}}{=\!=}& \frac{W_1}{2},\end{array}\right. \tag{4.44}$$

while (c) and (d) hold as equalities at D_2, located at

$$\left\{\begin{array}{lcl}\tau_{01} &=& -w_2\\ \tau_{02} &=& 0\end{array}\right. \quad \text{or,} \quad \left\{\begin{array}{lcl}\delta\theta^{D_2} &\stackrel{\text{def}}{=\!=}& \frac{W_2}{2}\\ \Theta^{D_2} &\stackrel{\text{def}}{=\!=}& \frac{W_2}{2}.\end{array}\right. \tag{4.45}$$

The point where (a) and (c) hold as equalities is T_1

$$\left\{\begin{array}{lcl}\tau_{01} &=& (w_2 - B^- w_1)/(B^{-2} - 1)\\ \tau_{02} &=& (B^- w_2 - w_1)/(B^{-2} - 1),\end{array}\right. \tag{4.46}$$

or,

$$\left\{\begin{array}{lcl}\delta\theta^{T_1} &\stackrel{\text{def}}{=\!=}& \frac{W_1 - W_2}{2(s_{12}/\mu - c_{12} - 1)}\\ &=& \frac{\mu m g}{2k_t R(\sin\theta_0 - \mu\cos\theta_0)}\left(\frac{\ddot{x}}{g}\cos\theta_T + (1+\frac{\ddot{y}}{g})\sin\theta_T\right)\\ \Theta^{T_1} &\stackrel{\text{def}}{=\!=}& \frac{W_1 + W_2}{2(s_{12}/\mu - c_{12} + 1)}\\ &=& \frac{\mu m g}{2k_t R(\cos\theta_0 + \mu\sin\theta_0)}\left((1+\frac{\ddot{y}}{g})\cos\theta_T - \frac{\ddot{x}}{g}\sin\theta_T\right),\end{array}\right. \tag{4.47}$$

and, finally, (b) and (d) hold as equalities at T_2, located at

$$\left\{\begin{array}{lcl}\tau_{01} &=& (B^+ w_1 + w_2)/(B^{+2} - 1)\\ \tau_{02} &=& -(w_1 + B^+ w_2)/(B^{+2} - 1),\end{array}\right. \tag{4.48}$$

or,

$$\left\{\begin{array}{lcl}\delta\theta^{T_2} &\stackrel{\text{def}}{=\!=}& -\frac{W_1 - W_2}{2(s_{12}/\mu + c_{12} + 1)}\\ &=& -\frac{\mu m g}{2k_t R(\sin\theta_0 + \mu\cos\theta_0)}\left(\frac{\ddot{x}}{g}\cos\theta_T + (1+\frac{\ddot{y}}{g})\sin\theta_T\right)\\ \Theta^{T_2} &\stackrel{\text{def}}{=\!=}& -\frac{W_1 + W_2}{2(s_{12}/\mu + c_{12} - 1)}\\ &=& -\frac{\mu m g}{2k_t R(\cos\theta_0 - \mu\sin\theta_0)}\left((1+\frac{\ddot{y}}{g})\cos\theta_T - \frac{\ddot{x}}{g}\sin\theta_T\right).\end{array}\right. \tag{4.49}$$

Points D_i, S_i and T_i delimit the admissible region of solutions to (4.36-4.39) in $\{\delta\theta, \Theta\}$ space. The physical relevance of these points is explained as follows. When the system is at point D_i, the normal force n_i and the tangential force τ_{0i} become zero, thus indicating

the detachment of contact i.

When at point S_i, on the other hand, the disk rotates rigidly with both contacts sliding simultaneously in the same direction (clockwise if at point S_1 and counterclockwise if at S_2). When on S_i the system is said to be on a Sliding Phase.

When at point T_i both contacts slide simultaneously in opposite directions. When at T_1, $\Theta > 0$ while at T_2, $\Theta < 0$.

The position of S_1 relative to D_1, and that of S_2 relative to D_2 determine the shape of the admissible space, and also the physical behavior of the disk upon forced rotation. This region of solutions is not fixed, the acceleration of the disk center of mass is contained in the terms W_1 and W_2 of equations (4.41), (4.43), (4.44), (4.45), (4.47) and (4.49). When $\ddot{x}$ and $\ddot{y}$ change the points defining the region in $\{\delta\theta, \Theta\}$ space move and the region changes. If the supports vibrate softly enough as to never break contact with the upper disk, the shape of this region determines the velocity of rotation of the upper disk, as will be discussed in Chapter 5.

To keep contacts closed, points $D1$ and $D2$ must remain inaccessible. This means having $\delta\theta^{S_1} > \delta\theta^{D_1}$ and $\delta\theta^{S_2} < \delta\theta^{D_2}$. These conditions are met when (from equations (4.41) and (4.43))

$$\mu < \frac{-\ddot{x}\cos(\theta_0 - \theta_T) + (g + \ddot{y})\sin(\theta_0 - \theta_T)}{\ddot{x}\sin(\theta_0 - \theta_T) + (g + \ddot{y})\cos(\theta_0 - \theta_T)}. \tag{4.50}$$

If both accelerations are much smaller than gravity, we can approximate condition (4.50) by

$$\mu \lesssim \tan(\theta_0 - \theta_T). \tag{4.51}$$

For small friction, thus, points D_1 and D_2 are not relevant, and the solution region is bounded by the quadrilateral with vertices at S_1, S_2, T_1 and T_2.

Figure 4.3 shows two possible shapes for the bounding quadrilateral in $\{\delta\theta, \Theta\}$ space. Dashed lines correspond to the case of vanishing accelerations $\ddot{x} = \ddot{y} = 0$, referred to as the quasi-static case. This case can be observed, for example, when the disk rotates under the effect of an external torque that oscillates very slowly. The quasi-static region is

asymmetric if $\theta_T \neq 0$. Dotted lines correspond to a solution with constant normal forces at each contact. The Amonton's friction limit is also constant for each contact and the region takes the form of a parallelogram rotated 45°. Since normal forces do not change, contacts cannot open, and points $D1$ and $D2$ go to infinity. This parallelogram is symmetric upon reflection through the origin, and becomes a square if both normal forces are equal.

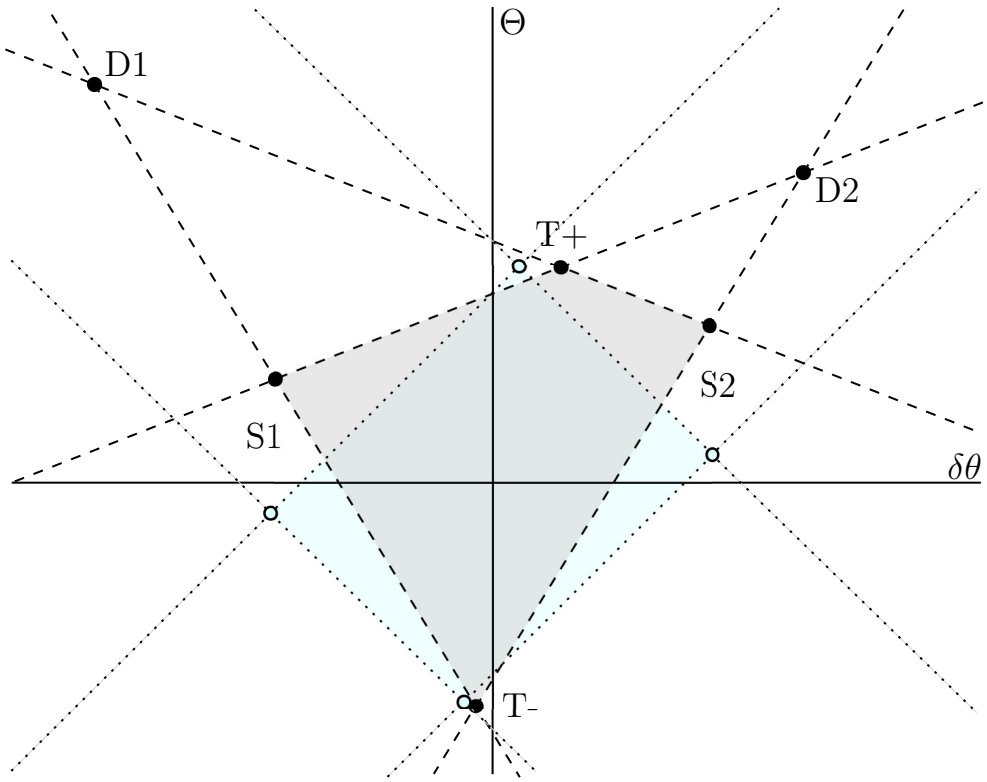

Figure 4.3: Admissible region of possible solutions for the tangential forces in $\{\delta\theta, \Theta\}$ space. Dotted lines delimit a symmetric region corresponding to constant normal forces. Dashed lines delimit the admissible region under quasistatic displacements, this region is asymmetric.

In Chapter 5 we apply the framework derived here to the simple case of a harmonic external torque applied to the upper disk.

4.5 Coefficients of restitution for the linear-dashpot model

While the previous discussion is useful to describe the 3-disk system with closed contacts, as soon as a contact opens, normal and tangential forces vanish. Without contact, the admissible region in $\{\delta\theta, \Theta\}$ space shrinks to a point, and the geometric framework of Section 4.4 is useless.

In a regime where contacts are short lived, and the disk is found bouncing off the supports, it is more useful to define a set of coefficients that account for the dynamics during a collision. In this section, we use the force model to integrate the dynamics during a collision, under the assumption that the time disks spend in contact is negligible compared to the time they spend apart, i.e, collision may be approximated as instantaneous events. From these calculations, we obtain a pair of coefficients that map velocities before a collision to velocities after a collision. These coefficients are called the normal coefficient of restitution e_n and the tangential coefficient of restitution e_t.

The coefficients e_n and e_t are used in the Event-Driven simulations for disk packings, as discussed in Section 2.3.1, and also in the discrete map developed in Chapter 6 to study the 3-disk system when the upper disks in bouncing on top of the supporting disks.

4.5.1 The normal coefficient of restitution

In the linear-dashpot model, the normal coefficient of restitution e_n turns out to be independent of the velocities of the colliding disks. The detailed derivation of e_n can be found in [44]. Here we reproduce some key aspects of the calculations, since some intermediate equations will be useful later on.

Let u_n and u_t be the relative normal and tangential velocities of a pair of disks a and b, with position vectors $\vec{r}_a$ and $\vec{r}_b$, and radii R_a and R_b. The distance between their centers is $r_{ab} = |\vec{r}_a - \vec{r}_b|$ and $\hat{n}_{ab}$ is a versor parallel to $\vec{r}_a - \vec{r}_b$.

For instantaneous collisions, the normal versor $\hat{n}_{ab}$ is constant. The time derivatives of the overlap, defined as $\delta = R_a + R_b - r_{ab}$, are, thus, independent of the tangential forces and velocities. If the rate of change of the normal versor, given by $\dot{\hat{n}}_{ab}$, is not negligible, a

collision cannot be approximated as instantaneous. Normal and tangential forces are then coupled through the term $\dot{\hat{n}}_{ab} = u_t^2/r_{ab}$, and the calculations of this section are not valid.

Assuming a constant normal versor $\hat{n}$, we can use Newton's equations of motion to obtain the acceleration of the overlap as

$$\ddot{\delta} = -(\ddot{\vec{r}_a} - \ddot{\vec{r}_b}) \cdot \hat{n}_{ab} = -\frac{n}{m_{eff}}, \tag{4.52}$$

where m_{eff} is the effective mass and n is the magnitude of the normal force. Given $u_n = -\dot{\delta}$, we can rewrite n from equation (4.1) as

$$n = k_n\delta + \gamma_n\dot{\delta}. \tag{4.53}$$

Equation (4.52)is that of a damped harmonic oscillator. Taking into account the boundary conditions, $\delta(0) = 0$ and $\dot{\delta}(0) = u_n$, the solution for $\delta(t)$ is

$$\delta(t) = \begin{cases} -\dfrac{u_n}{\omega_n} e^{-\beta t} \sin(\omega_n t), & \beta < \omega_0 \\ -\dfrac{u_n}{\omega_n} e^{-\beta t} \sinh(\omega_n t), & \beta > \omega_0, \end{cases} \tag{4.54}$$

where $\omega_0^2 = k_n/m_{eff}$, $\beta = \gamma_n/2m_{eff}$ and $w_n^2 = |\omega_0^2 - \beta^2|$.

We can use equation (4.54) to find the duration of the collision t_c from the condition that the overlap must be zero at the end of the collision. For under-damped oscillations, solving for t_c from the condition $\delta(t_c) = 0$ yields $t_c = \pi/\omega_n$, the over-damped case has no solution. The normal coefficient of restitution can be evaluated as $e_n = -\dot{\delta}(t_c)/u_n = \exp(-\beta t_c)$. A problem with this solution is that it allows for negative normal forces near the end of the collision. Negative normal forces are unrealistic, since we only consider repulsive forces in the linear-dashpot model.

A better way of deriving e_n is to end the collision as soon as the normal force vanishes for the first time. This can be expressed as the condition $\ddot{\delta}(t_c) = 0$. Differentiating

equation (4.54) twice, and solving for t_c, yields the solution

$$t_c = \begin{cases} \frac{1}{\omega_n}\left(\pi - \arctan\frac{2\beta\omega_n}{\omega_n^2-\beta^2}\right), & \beta < \frac{\omega_0}{\sqrt{2}} \\ -\frac{1}{\omega_n}\left(\arctan\frac{2\beta\omega_n}{\omega_n^2-\beta^2}\right), & \beta \in \left[\frac{\omega_0}{\sqrt{2}}, \omega_0\right] \\ \frac{1}{\omega_n}\ln\frac{\beta+\omega_n}{\beta-\omega_n}, & \beta > \omega_0, \end{cases} \tag{4.55}$$

whereby a solution for the over-damped case is now possible.

We calculate the coefficient of normal restitution as

$$e_n = e^{-\beta t_c} = \begin{cases} \exp\left[-\frac{c}{\sqrt{1-c^2}}\left(\pi - \arctan\frac{2c\sqrt{1-c^2}}{1-2c^2}\right)\right], & c < \frac{1}{\sqrt{2}} \\ \exp\left[\frac{c}{\sqrt{1-c^2}}\left(\arctan\frac{2c\sqrt{1-c^2}}{1-2c^2}\right)\right], & c \in \left[\frac{1}{\sqrt{2}}, 1\right] \\ \exp\left[-\frac{c}{\sqrt{c^2-1}}\ln\frac{c+\sqrt{c^2-1}}{c-\sqrt{c^2-1}}\right], & c > 1. \end{cases} \tag{4.56}$$

Note that e_n depends only on the dimensionless damping ratio c, defined by the relation $\beta = \omega_0 c$.

In the under-damped case ($c < 1$), the normal force during the collision is given by the equation

$$n(t) = -\frac{e^{-\frac{\gamma_n}{2m_{eff}}t}u_n}{\omega_n}\left[\gamma_n\omega_n\cos(\omega_n t) + (k_n - \frac{\gamma_n^2}{2m_{eff}})\sin(\omega_n t)\right]. \tag{4.57}$$

The normal force changes discontinuously from zero to $-\gamma_n u_n$ at the beginning of the collision, at $t = 0$. Care needs to be taken when discontinuous forces are implemented in MD simulations, a further discussion on this topic can be found in [36].

4.5.2 The tangential coefficient of restitution

The dynamics in the tangential direction can be separated in two regimes: a sticking regime, where the tangential force is proportional to the relative tangential displacement δ_t, and a slipping regime, where the tangential force is saturated, and its value is given by

the Coulomb friction force as $\tau = \mu n$, where μ is the friction coefficient.

Tangential dynamics may switch regimes several times during the duration of a collision. This makes obtaining a closed analytic expression for the tangential force and coefficient of restitution difficult. We can, however, solve each in regime and stitch the solutions numerically. Also, in the limit of high impact velocities, the slipping regime will last almost for the full collision, making it possible to obtain an approximate analytic expression for e_t. Other limiting cases are also considered in this section. A nice discussion of the tangential coefficient of restitution within the linear-dashpot model can be found in [45].

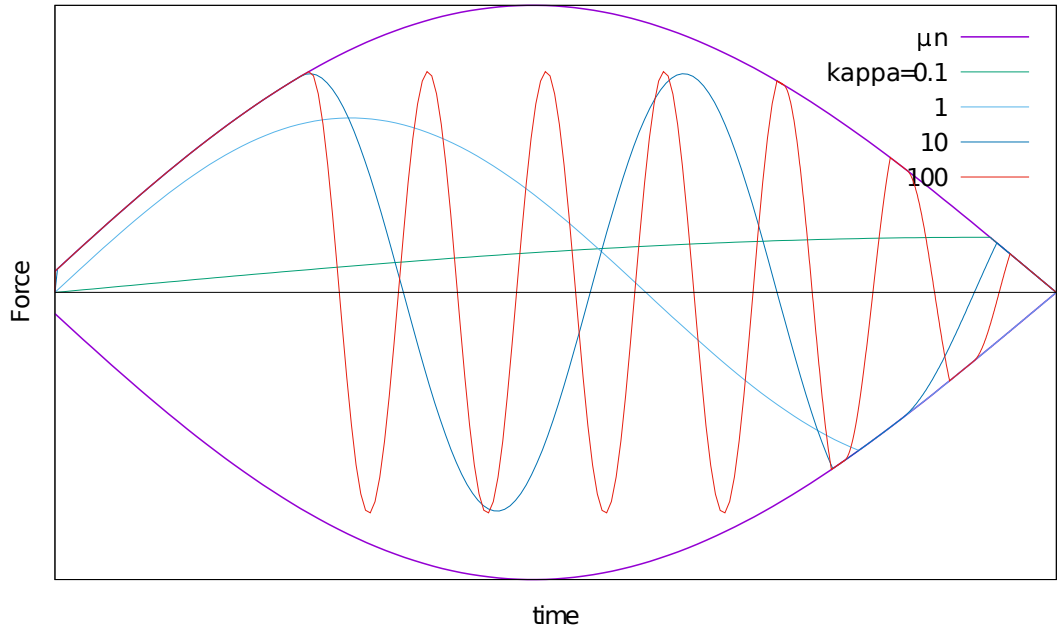

Figure 4.4: Forces during a collision between disks under the linear-dashpot model. The purple line represents the scaled normal force μn. Tangential forces for different stiffness ratios $\kappa = k_t/k_n$ oscillate, limited by the normal force.

A typical behavior of the forces during a collision is shown in Figure 4.4. The tangential force is given by

$$\tau = \begin{cases} -\operatorname{sgn}(\delta_t)\, k_t |\delta_t|, & |\delta_t| < \mu n \qquad \text{(stick)}, \\ -\operatorname{sgn}(\delta_t)\, \mu n, & |\delta_t| \geq \mu n / k_t \quad \text{(slip)}. \end{cases} \tag{4.58}$$

A general equation of motion can be derived from Newton's second law and the definitions for the relative velocity at the contact point $\vec{u} = (\vec{v}_a - \vec{v}_b) - (R_a\vec{\omega}_a + R_b\vec{\omega}_b) \times \hat{n}_{ab}$, and the relative tangential velocity $\vec{u}_t = -\hat{n}_{ab} \times (\hat{n}_{ab} \times \vec{u})$. It can be shown [45] that

$$\frac{du_t(t)}{dt} = \frac{\tau}{\alpha}, \tag{4.59}$$

with

$$\alpha = \left[\frac{1}{m_{eff}} + \frac{R_a^2}{I_a} + \frac{R_b^2}{I_b}\right]^{-1} = \frac{m_{eff}}{3}. \tag{4.60}$$

The last equality is true for disks with moment of inertia $I = mR^2/2$.

In the sticking regime, $\tau = -k_t\delta_t$, and the equation of motion (4.59) becomes

$$\ddot{\delta}_t(t) = -\frac{k_t}{\alpha}\delta_t(t) = -\omega_t^2\delta_t(t), \tag{4.61}$$

where $\omega_t^2 = k_t/\alpha$, and we have used the fact that $u_t(t) = \dot{\delta}_t(t)$. The set of solutions, integrating from an arbitrary time t_0, up to time t, are

$$\delta_t{}^{st} = \delta_t(t_0)\cos\left[\omega_t(t-t_0)\right] + \frac{u_t(t_0)}{\omega_t}\sin\left[\omega_t(t-t_0)\right], \tag{4.62}$$

$$u_t^{st}(t) = -\omega_t\delta_t(t_0)\sin\left[\omega_t(t-t_0)\right] + u_t(t_0)\cos\left[\omega_t(t-t_0)\right], \tag{4.63}$$

$$\tau^{st}(t) = -k_t\delta_t(t_0)\cos\left[\omega_t(t-t_0)\right] - \frac{k_t u_t(t_0)}{\omega_t}\sin\left[\omega_t(t-t_0)\right]. \tag{4.64}$$

In the sliding regime, the skin is stretched at its maximum, and $\tau = -\operatorname{sgn}(\delta_t)\,\mu n$. Equation (4.59) takes the form

$$\dot{u}_t(t) = -\operatorname{sgn}\left(\delta_t(t_0)\right)\frac{\mu}{\alpha}n(t), \tag{4.65}$$

with the solutions

$$\begin{aligned} u_t^{sl}(t) =& u_t(t_0) - 3\,\mathrm{sgn}\left(\delta_t(t_0)\right)\mu u_n e^{-\beta t_0}\times \\ & \left\{ e^{-\beta(t-t_0)}\left[\cos(w_n t) - \frac{\beta}{\omega_n}\sin(\omega_n t)\right] - \right. \\ & \left. \left[\cos(w_n t_0) - \frac{\beta}{\omega_n}\sin(\omega_n t_0)\right]\right\}, \end{aligned} \tag{4.66}$$

$$\tau^{sl} = \mathrm{sgn}\left(\delta_t(t_0)\right)\frac{e^{-\beta t}\mu u_n}{\omega_n}\left[\gamma_n\omega_n\cos(\omega_n t) + (k_n - \beta\gamma_n)\sin(\omega_n t)\right]. \tag{4.67}$$

Now that we have solutions for each regime, we need to stitch them. As long as there is dissipation, the normal force at $t = 0$ will be positive, and a finite Coulomb limit will exist at the beginning of the collision. There is no initial sliding phase for $\gamma_n > 0$. At the end of the collision, the normal force n goes to zero, as does the Coulomb limit for the tangential force. There is always a sliding phase at the end of the collision. This means there is at least one switch of regime during the collision, from sticking to sliding.

Let the time at which the switch occurs be t_s. The transition from sticking to sliding occurs when the skin is at its maximum elongation, this is

$$|\delta_t(t_s)| = \frac{\mu}{k_t} n(t_s). \tag{4.68}$$

For a transition from sliding to sticking, we need to obtain the value of the tangential force in the sticking regime after an infinitesimal time δt. We then need to compare this value to the saturated force given by the Coulomb limit. The transition will take place the moment both forces are equal, i. e., the moment the tangential force no longer exceeds the Coulomb limit. This can be expressed as

$$-k_t\delta_t(t_s + \delta t) = -\,\mathrm{sgn}\left(\delta_{t0}\right)\mu n(t_s + \delta t). \tag{4.69}$$

Expanding equation (4.69) to first order in δt, we obtain

$$\delta_t(t_s) + u_t(t_s)\delta t = \mathrm{sgn}\left(\delta_{t0}\right)\frac{\mu}{k_t}\left(n(t_s) + \dot{n}(t_s)\delta t\right). \tag{4.70}$$

Finally, from the fact that, at the transition, $k_t\delta_t(t_s) = \operatorname{sgn}(\delta_{t0})\,\mu n(t_s)$, we obtain the condition for switching, from sliding to sticking, at t_s as

$$u_t(t_s) = \operatorname{sgn}(\delta_{t0})\,\frac{\mu}{k_t}\dot{n}(t_s). \tag{4.71}$$

The derivative of the normal force involved in equation (4.71) is

$$\begin{aligned}\dot{n}(t) = -\frac{u_n e^{-\beta t}}{\omega_n}\,[&(k_n - 2\beta\gamma_n)\omega_n\cos(\omega_n t) - \\ &(k_n\beta + (\omega_n^2 - \beta^2)\gamma_n)\sin(\omega_n t)\big]\,.\end{aligned} \tag{4.72}$$

Equations (4.68) and (4.71) can only be solved numerically, except for the case $\gamma_n = 0$, for which an analytic solution for equation (4.71) can be obtained. Once all switching times t_s are found, equations for different regimes need to be stitched together up to time t_c, at which the collision ends. Remember that t_c is given by equation (4.55). The coefficient e_t, calculated as $e_t = u_t(t_c)/u_t(0)$, is plotted in Figure 4.5 as a function of the ratio $|u_t/u_n|$ for different values of the stiffness ratio κ. It can be shown that, in the limit of elastic collisions, e_t only depends on the ratio $|u_t/u_n|$. From Figure 4.5, it is clear that, for large values of $|u_t/u_n|$, all curves are well approximated by e_t in the full-sliding limit (thin solid line).

We now obtain the expression for e_t in the limit of full sliding. The impulse equations for the relative velocities are

$$\int_0^{t_c} n\,dt = -(1+e_n)m_{eff}u_n, \tag{4.73}$$

$$u_t' - u_t = \frac{1}{\alpha}\int_0^{t_c}\tau\,dt = -\operatorname{sgn}(u_t)\,\frac{\mu}{\alpha}\int_0^{t_c} n\,dt = 3\operatorname{sgn}(u_t)\,\mu(1+e_n). \tag{4.74}$$

Using the definition of the tangential coefficient of restitution, $e_t = u_t(t_c)/u_t(0)$, and equation (4.74), we get

$$e_t = 1 - 3\mu(1+e_n)\left|\frac{u_n}{u_t}\right|. \tag{4.75}$$

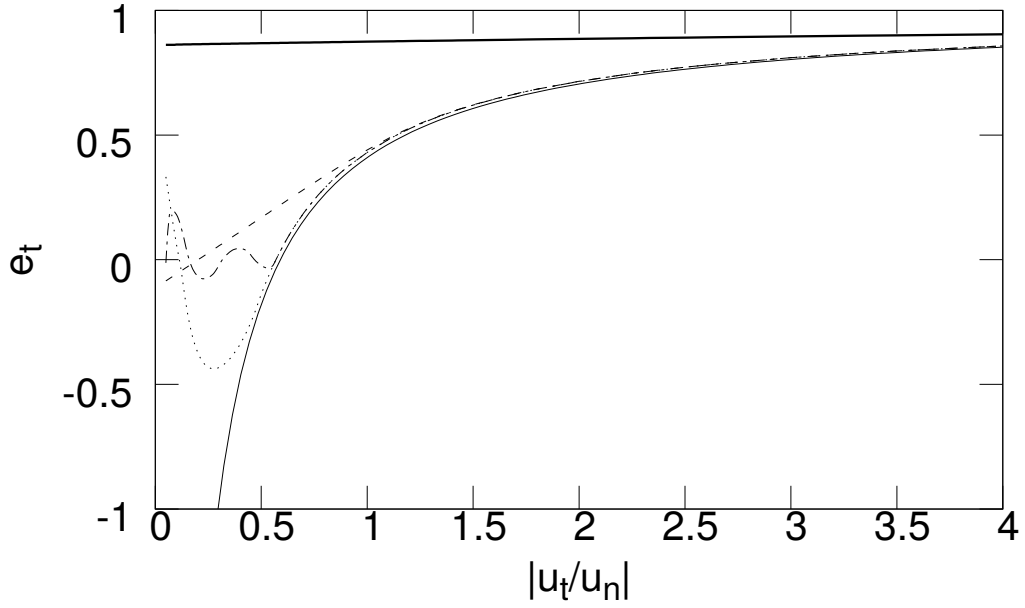

Figure 4.5: The tangential coefficient of restitution e_t, numerically calculated for different values of stiffness ratio κ. For comparison, e_t for the full sliding approximation (Eq. (4.75)) is also plotted (thin solid line). Values of κ used are: $\kappa = 0.01$ (thick line), $\kappa = 0.10$ (dashed line), $\kappa = 1.00$ (dotted line) and $\kappa = 10.00$ (dot-dashed line). Other simulation parameters are: $k_n = 4.5e6N/m$, $R = 0.02m$, $\gamma = 9.84kg/s$, $\mu = 0.1$, $m = 4.5g$.

It has been reported in [45] that the coefficient of tangential restitution cannot be less than zero for full sliding. This is not true. If the Coulomb limit recedes faster than the tangential spring, the system can keep on sliding, even if the tangential velocity has changed sign. We have taken this into account in the numerical implementation of the coefficients.

We already know that for, $\gamma_n \neq 0$, the system always starts in the sticking regime, but we still need to treat the case for $\gamma_n = 0$. If there is no dissipation, and the initial tangential relative velocity is large, the system may start in the sliding regime. To determine the regime at the beginning of the collision, we start by analyzing the forces after an infinitesimal displacement at $t = 0$. From equation (4.71), the condition for sliding at the beginning is

$$\left|\frac{u_t}{u_n}\right| > \frac{\mu k_n}{k_t}. \tag{4.76}$$

To recover the full sliding case, we need that $\gamma_n = 0$, the validity of condition (4.76), and that the solution for the first transition time t_{s1} be greater than the duration of the collision t_c. Solving (4.71), with $t_0 = 0$, for t_{s1}, we find

$$t_{s1} = \frac{1}{\omega_n} \cos^{-1} \frac{\left|\frac{u_t}{u_n}\right| - 3\mu}{\frac{\mu k_n}{k_t} - 3\mu}. \tag{4.77}$$

The system remains sliding throughout the collision if $t_{s1} > t_c = \pi/\omega_n$. A condition for this to happen is that t_{s1} must be real, this requires that

$$\left|\frac{u_t}{u_n}\right| > 6\mu - \frac{\mu k_n}{k_t}. \tag{4.78}$$

Al last, in the limit of small tangential velocities, we can ignore the slip at the end of the collision, and use equation (4.63) alone, to obtain

$$\lim_{u_t \to 0} u_t(t_c) = u_t \cos(\omega_t t_c). \tag{4.79}$$

The results of this section are used to evaluate e_t in ED simulations as follows. At the

beginning of the collision, the ratio $\left|\frac{u_t}{u_n}\right|$ is calculated. If $\left|\frac{u_t}{u_n}\right| = 0$, we set $e_t = 1$. If $\left|\frac{u_t}{u_n}\right| > 0$, we check if equation (4.76) is satisfied. If it is, the tangential velocity is large enough to approximate e_t using equation (4.75). Finally, if equation (4.76) is not satisfied, we numerically evaluate e_t by stitching the solutions for u_t across switching times t_s.

5 The 3-disk model with lasting contacts

In Chapter 4 we introduced a toy model to study rotations for a system of one disk supported by two contacts against gravity. In this chapter we present numerical results for rotation of the upper disk, in this model, for two types of excitation: vibration of the supporting contacts and a slowly oscillating external torque acting on the upper disk. We discuss these results using the previously mentioned one-disk model, and develop a one-dimensional model that captures the behavior of these systems in the limit of frequent sliding, (e.g. when μ is small).

For a disk that never loses contacts with the supports, the only way to accumulate rotation is to change the value of the equilibrium angle θ_{eq}, given by equation (4.13). This angle can change only during sliding of the contacts, i.e., on the boundary of the quadrilateral of Figure 4.3. Furthermore, the amount of sliding at each contact, given by the changes in $\hat{\theta}_{01}$ and $\hat{\theta}_{02}$, must satisfy the constrains for the skin stretch $\Theta = (\hat{\theta}_{02} - \hat{\theta}_{01})/2$. This means a large slide at one contact must be accompanied by a slide at the other contact in order to keep the value of Θ inside the bounded region. If contacts slide more often in a given direction, then the change in θ_{eq} is biased, and rotation accumulates. For an unbiased excitation of the upper disk, the bias in sliding preference originates in the asymmetry of the Amonton inequalities (4.36) through (4.39). This asymmetry is reflected in the shape of the bounding quadrilateral. It is easier to reach some boundaries than others. It is easy to verify that for zero tilt ($\theta_T = 0$) the quadrilateral becomes symmetric. In this case rotation cannot accumulate. If normal forces are held constant, even if the system is tilted, the bounded region in $(\delta\theta, \Theta)$ is always symmetric, as illustrated by the dotted polygon of Figure 4.3. Under this condition of constant normal forces, the upper disk does not rotate.

This means that it is not sufficient that normal forces at each contact be different, they also must be allowed to fluctuate as part of the dynamics of the system in order to observe rotation.

5.1 Simulation details

In order to study the 3-disk system, we used the molecular dynamics simulation program described in Section 2.2. We performed a numerical exploration of the effects of various excitation amplitudes and system tilts on the rotational velocity.

Our simulations consider a disk interacting via elastic, viscous, and frictional forces with two supporting disks, as described in Chapter 4. Contact forces are described by equations (4.2) and (4.3), with parameter values $k_n = 10^3$, $k_t = 10^6$, $\gamma = 10$, and friction coefficient $\mu = 0.1$. Stiffness values where chosen to make the disk tangentially stiff, while being relatively soft in the normal direction. This allows us to explore a wider range of excitation amplitudes, without the disk loosing contact with the support disks. Viscous dissipation is chosen to keep normal oscillations in the underdamped regime.

Besides contact forces from the supporting disks, the top disk experiences a downward gravitational acceleration of magnitude $g = 10$. The disk has radius $R = 1$ and mass $m = 0.1$, which gives a gravitational force of $mg = 1$. Units are arbitrary, and the parameter values where chosen to simplify the analysis of the results. No attempt to relate the simulated system to a physical one is made in this study.

The time-step Δt for the integration of the equations of motion (a fifth-order predictor-corrector algorithm is used) is set to 10^{-6} s, which is at least smaller than one hundredth of the natural frequency of tangential oscillations, and much smaller than that of normal oscillations.

We implemented two types of excitation: 1) An external torque acting directly on the top disk, of amplitude A_e, and angular frequency ω_e. 2) A random vibration of the supporting disks. The external torque excitation is discussed first, since it lends itself to being studied using the theoretical framework of Chapter 4. Discussing the external torque case first will allow us to familiarize ourselves with the system, before approaching the more relevant case of random vibration of the supports.

5.2 Direct Excitation: Harmonic Torque

As mentioned in Section 4.4, if the 3-disk system is excited gently enough as to maintain the accelerations $\ddot{x} = \ddot{y} = 0$, the shape of the admissible region in $\{\delta\theta, \Theta\}$ space is constant in time and is that of the asymmetric polygon of Figure 4.3. One way to accomplish this gentle excitation is by imposing a slowly oscillating external torque on the upper disk. The frequency ω_e of the torque must be much smaller than the largest natural frequency of oscillation at the contacts. This means $\omega_e \ll \sqrt{k/m}$, with $k = \max(k_n, k_t)$. The torque is given by the equation

$$T_e = A_e \sin(\omega_e t), \tag{5.1}$$

where A_e is the torque amplitude.

In this quasi-static regime, as long as at least one contact does not slide, tangential forces at the contacts will adjust to match the external torque. This prevents the disk from accelerating, and maintains its rotational and translational velocities at zero. If the external torque grows beyond the combined Amonton's limits of both contacts, both contacts start to slide simultaneously in the same direction, and the disk experiences angular acceleration. Once contacts are saturated, any increase in torque will only influence the angular degree of freedom, maintaining the disk in translational equilibrium during sliding.

The disk will continue to accelerate and accumulate rotation until the torque decreases again below the Amonton's limit. At this point friction forces will decelerate the disk until it stops and torque equilibrium is restored. This process then repeats in the opposite direction. We have shown, in Section 4.4 that, if the system is tilted, clockwise sliding contacts saturate at a different Amonton's limit than counter-clockwise sliding contacts, i.e., $\delta\theta^{S1} \neq \delta\theta^{S2}$. This means that the angular acceleration of the disk when sliding clockwise, as well as the time spent sliding, are different than those when sliding counter-clockwise. The net rotation is then non-zero, and angular drift accumulates. The mean rotational velocity of the upper disk $\bar{\omega}$ can be calculated as the net rotation over a period

of oscillation of the torque

$$\bar{\omega} = \frac{\Delta\theta_1 + \Delta\theta_2}{2\pi/\omega_e}, \tag{5.2}$$

where $\Delta\theta_1$ is the angle rotated when sliding clockwise at S_1, and $\Delta\theta_2$ is the angle rotated when sliding counter-clockwise at S_2.

To reach S_2 and slide counter-clockwise, the external torque must surpass the Amonton's limit at S_2. Using equations (4.18) and (4.43) we can write this limit as

$$A_{S2} = A_0(\cos\theta_T - \mu\sin\theta_T), \tag{5.3}$$

with A_0 given by

$$A_0 = \frac{gm\mu R}{\cos\theta_0(1+\mu^2)}. \tag{5.4}$$

In the same way, to reach S_1, and slide clockwise, the external torque must surpass the Amonton's limit at S_1, which, by equations (4.18) and (4.41), can be written as

$$A_{S1} = A_0(\cos\theta_T + \mu\sin\theta_T). \tag{5.5}$$

Notice that, for positive tilt, $A_{S2} < A_{S1}$; it is easier to reach the sliding point S_2 than it is to reach S_1. This means that the system spends more time sliding counter-clockwise, with the result that the rotational velocity is always positive. When the system is excited differently, the sense of rotation may differ from the one observed for external torque forcing. In particular (Section 5.3), when the supports are vibrated randomly, the velocity is always opposite in sign to the one observed here.

The behavior of the critical amplitudes A_{S1} and A_{S2} can be understood qualitatively as follows. When the system is tilted with $\theta_T > 0$, contact 1 is forced to carry a larger portion of the upper disk's weight. This it makes it easier to slide at contact 2 than at contact 1. Upon external forcing, contact 2 always slides first. Once contact 2 is sliding, any excess torque must be compensated by the tangential force at 1 alone, which is accomplished with relatively little excess torque. Since it is easier to saturate contact 2 with a positive torque

than with a negative one, the disk always rotates counter-clockwise. The reason contact 2 saturates faster for counter-clockwise rotation can be understood from the influence that each tangential force at each contact has in the Amonton's limit of the opposite contact.

When the external torque is positive, tangential forces are negative and point opposite to the arrows of Figure 4.1. The tangential force at contact 1 pulls the disk away from contact 2, decreasing the Amonton's limit at 2. At the same time, tangential force at 2 pushes the disk onto the support 1, increasing the Amonton's limit at 1. This means that an increasing positive torque favors sliding at a contact 2, already weakened by the system tilt. This explains why A_{S2} grows monotonically with θ_T.

On the other hand, when the external torque is negative, tangential forces are positive, and the opposite happens. The tangential force at contact 1 increases the limit at contact 2, while tangential force at contact 2 decreases the limit at 1. As the torque continues to decrease it becomes harder to slide at contact 2, in opposition to the weakening effect of the tilt. For low tilt, this strengthening effect dominates, and A_{S1} grows with θ_T. As tilt increases, tangential force at contact 1 cannot compensate the weakening due to tilt, and A_{S1} starts decreasing. This explains the appearance of a maximum for A_{S1}.

5.2.1 Sliding regimes

Depending on the value of A_e relative to A_{S1} and A_{S2}, different sliding regimes can be identified. For $A_e < A_{S2}$ the contacts never slide and the disk does not rotate. For $A_{S2} < A_e < A_{S1}$, the upper disk only slides counter-clockwise at S_2, we call this unidirectional sliding. For $A_e > A_{S1}$, the system slides both counter-clockwise, at S_2, and clockwise, at S_1. We call this bidirectional sliding. A diagram delimiting sliding regimes in $(\theta_T,\ A_e/A_0)$ space is shown in Figure 5.1. This diagram has tilt values ranging from $\theta_T = 0$ to a maximum value θ_T^D. The tilt value θ_T^D is defined as the tilt at which it becomes possible for contacts to open, this is, the detaching points D_i described in Section 4.4 become first accessible. The tilt θ_T^D can be obtained from equation (4.51) as $\theta_T^D = \theta_0 - \arctan\mu$.

From Figure 5.1 it is clear that, for a fixed tilt, as the amplitude A_e increases, the system always transitions from no-sliding to unidirectional, and finally to bidirectional sliding. The situation is not so simple when tilting the system at fixed amplitudes (this amounts to tracing horizontal lines in the phase diagram). If $A_e < A_{S2}(\theta_T^D)$ the systems

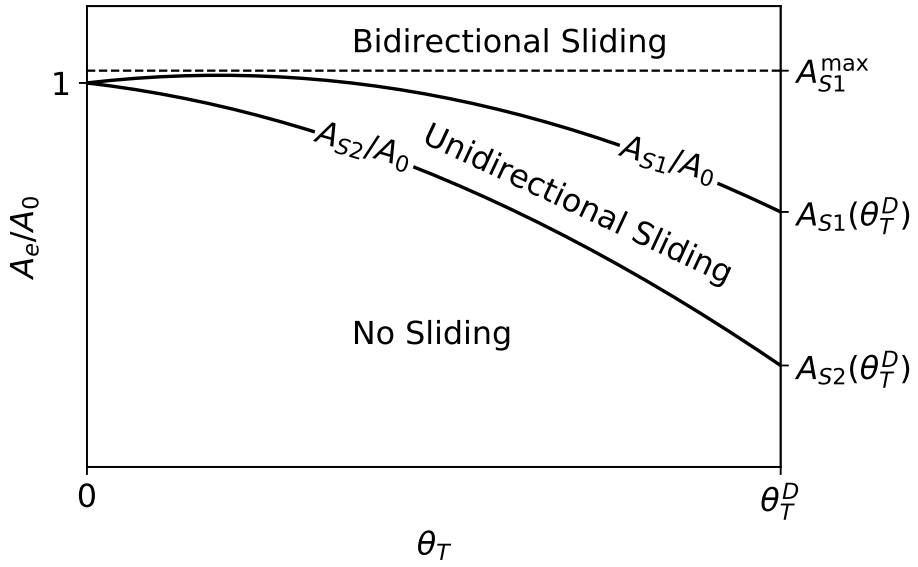

Figure 5.1: Sliding phase diagram for the 3-disk system forced by an external harmonic torque. θ_T is the tilt and θ_T^D the detachment limit.

never leaves the no-sliding regime. If $A_{S2}(\theta_T^D) < A_e < A_{S1}(\theta_T^D)$, the system goes from no-sliding to unidirectional sliding, but contacts detach before reaching bidirectional sliding. If $A_{S1}(\theta_T^D) < A_e < A_0$ the system goes from no-sliding to unidirectional sliding, and can proceed to bidirectional sliding. For $A_e > A_0$ the system starts at the bidirectional sliding regime. If, in addition to $A_e > A_0$, A_e is below the maximum for A_{S1} ($A_{S1}^{\max} = A_{S1}(\arctan\mu)$), as θ_T increases the systems transitions to unidirectional sliding, then goes back to bidirectional sliding, thus displaying reentrant behavior. If $A_e > A_{S1}^{\max}$ the system always stays at bidirectional sliding until detachment.

5.2.2 Numerical Simulations

Figures 5.2 and 5.3 show the rotational velocity $\bar{\omega}$ of the upper disk as a function of A_e, obtained from numerical simulations of the 3-disk system under quasistatic torque. Different lines correspond to different tilt values θ_T. Figure 5.2 shows $\bar{\omega}$ vs A_e in linear scale. For $\theta_T = 0$ (circles) the disk never rotates, the Amonton's limits at the contacts

are symmetric. For the other lines, the transition from no-sliding to unidirectional sliding comes earlier for increasing values of θ_T. This is expected since A_{S2} decreases with θ_T as described by equation (5.3).

Figure 5.3 shows $\bar{\omega}$ vs $(A_e - A_{S2})$ in log-log scale. For low amplitudes, the system is in unidirectional sliding and the velocity scales as $(A_e - A_{S2})^2$. For large amplitudes, $A_e > A_{S1}$, and the system transition to bidirectional sliding, the velocity scales linearly in $(A_e - A_{S2})$.

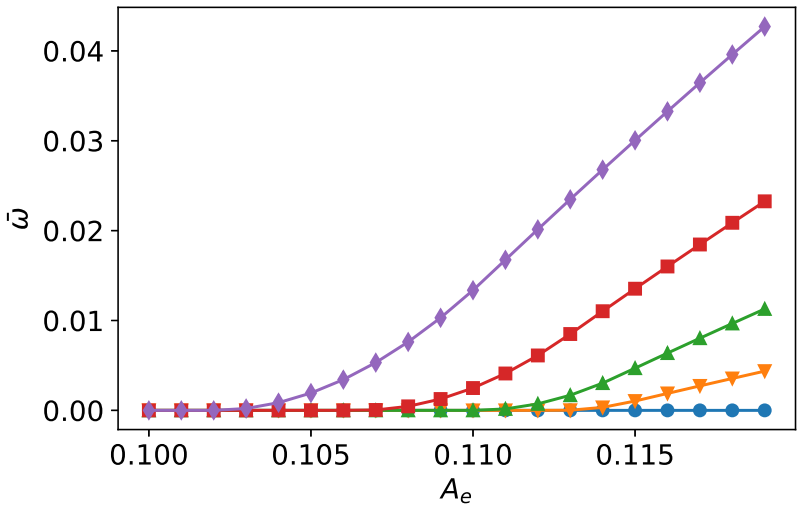

Figure 5.2: Numerical simulation results for the mean rotational velocity $\bar{\omega}$ of the upper disk vs the amplitude of the applied external torque A_e in linear scale. Different lines correspond to different values of system tilt with respect to gravity, $\theta_T = 0\pi$ (circles), $\theta_T = 0.03\pi$ (triangles pointing down), $\theta_T = 0.06\pi$ (triangles pointing up), $\theta_T = 0.09\pi$ (squares), $\theta_T = 0.12\pi$ (diamonds).

Figures 5.4 and 5.5 show plots of the rotational velocity $\bar{\omega}$ vs system tilt θ_T, obtained from numerical simulations, for different values of torque amplitude A_e. Figure 5.4 shows $\bar{\omega}$ vs θ_T in linear scale. For $A_e = 0.100 < A_{S2}(\theta_T^D)$ (circles), the disk never rotates. For values of $A_e = 0.105$ (triangles pointing down), $A_e = 0.110$ (triangles pointing up), and $A_e = 0.113$ (squares) there is a transition to unidirectional sliding at a critical tilt value $\theta_T = \theta_{S2}$. The critical value θ_{S2} can be found numerically by solving the equation $A_e = A_{S2}(\theta_{S2})$. For

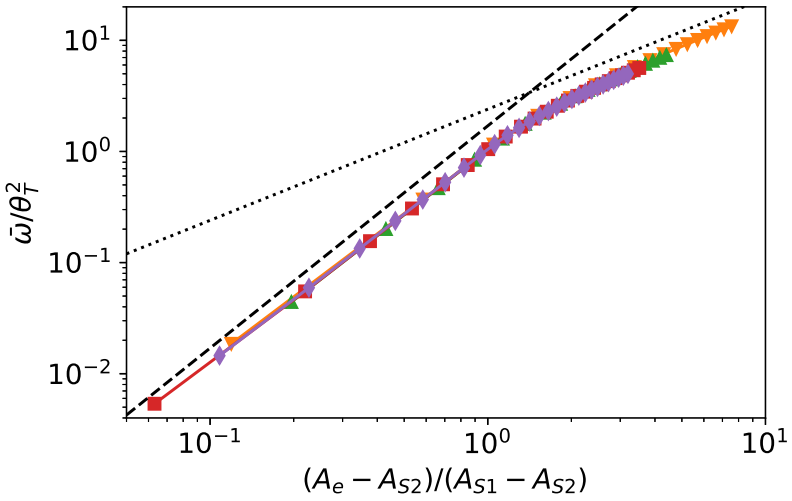

Figure 5.3: Numerical simulation results for the mean rotational velocity $\bar{\omega}$ of the upper disk vs the amplitude of the applied external torque A_e in log-log scale. Different lines correspond to different values of system tilt with respect to gravity, $\theta_T = 0.03\pi$ (triangles pointing down), $\theta_T = 0.06\pi$ (triangles pointing up), $\theta_T = 0.09\pi$ (squares), $\theta_T = 0.12\pi$ (diamonds). Rotational velocity $\bar{\omega}$ displays the power law scaling in $A_e - A_{S2}$, where A_{S2} is the critical amplitude given by equation (5.3). All curves collapse under the scaling displayed on the axes. A_{S1} is the amplitude at which the systems enters bidirectional scaling. The dotted line has slope 1 and the dashed line slope 2.

$A_e = 0.115$ (diamonds), the systems experiences bidirectional sliding for all tilts.

Figure 5.5 shows $\bar{\omega}$ vs $(\theta_T - \theta_{S2})$ in log-log scale. In this plot we appreciate an almost quadratic scaling of the velocity in the unidirectional sliding regime. For the bidirectional sliding regime ($A_e = 0.115$, diamonds), the scaling becomes quadratic only for large tilts.

5.2.3 The hysteresis cycle

Paths traced in $(\delta\theta,\ \Theta)$ space, obtained from numerical simulations, for two different torque amplitudes, $A_e = 0.100$ and $A_e = 0.113$, at tilt $\theta_T = 0.1\pi$, are shown in Figure 5.6. The quadrilateral determining the admissible space, together with the points S_1, S_2, T_1, and T_2, are plotted, as given by equations (4.41), (4.43), (4.47), and (4.49), under the condition

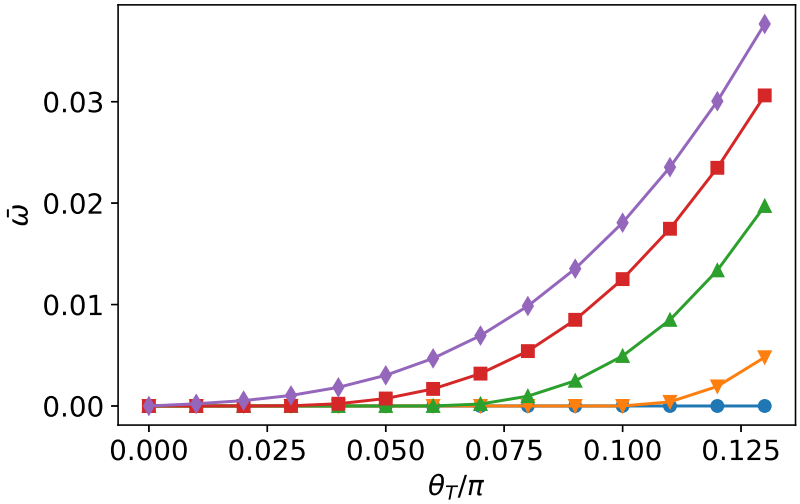

Figure 5.4: Numerical simulation results for the mean rotational velocity $\bar{\omega}$ of the upper disk vs the system tilt θ_T in linear scale. Different lines correspond to different values of amplitude A_e of the applied external torque, $A_e = 0.100$ (circles), $A_e = 0.105$ (triangles pointing down), $A_e = 0.110$ (triangles pointing up), $A_e = 0.113$ (squares), $A_e = 0.115$ (diamonds).

that $\ddot{x} = \ddot{y} = 0$. For $A_e = 0.100$ we have $A_e < A_{S2}$ and the system never reaches the sliding points, so the disk does not rotate. For $A_e = 0.113$, we have $A_e > A_{S1}$ and the system is in the bidirectional sliding regime. Both S_1 and S_2 are reached and the disk rotates.

As shown in Figure 5.6, when in bidirectional sliding, the system executes the following sequence: Start at S_1, just when the disk has stopped rotating. Then let θ change under the effect of the external torque. When the external torque increases, the disk rotates counter-clockwise, and $\delta\theta$ grows. Since no contact has slipped so far, Θ remains constant. The system, then, moves horizontally towards the line $\overline{T_2S_2}$, defined by inequality (4.39). Upon reaching $\overline{T_2S_2}$, contact 2 starts sliding, and both $\delta\theta$ and Θ grow along this line towards S_2. After some time at S_2, the torque $\mathcal{T}_e$ decreases below A_{S2}, and friction forces start to decelerate the disk. When the disk stops, the system leaves S_2 and moves along the horizontal line $\Theta = \Theta^{S2}$ towards the line $\overline{T_1S_1}$ defined by inequality (4.38). Upon reaching $\overline{T_1S_1}$, contact 1 starts sliding, and both $\delta\theta$ and Θ decrease along this line, towards

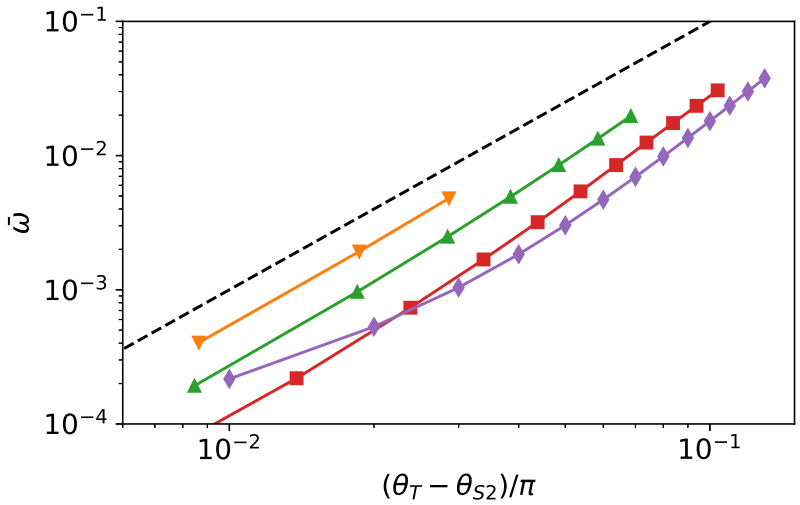

Figure 5.5: Numerical simulation results for the mean rotational velocity $\bar{\omega}$ of the upper disk vs the system tilt θ_T in log-log scale. Different lines correspond to different values of amplitude A_e of the applied external torque, $A_e = 0.105$ (triangles pointing down), $A_e = 0.110$ (triangles pointing up), $A_e = 0.113$ (squares), $A_e = 0.115$ (diamonds). The velocity $\bar{\omega}$ scales quadratically in $\theta_T - \theta_{S2}$, where θ_{S2} is the critical tilt obtained by solving the equation $A_e = A_{S2}$. The dashed line has slope 2.

S_1. After some time at S_1, $\mathcal{T}_e$ increases above $-A_{S1}$, and friction forces start to decelerate the disk. When the disk stops, the system leaves S_1 along the horizontal line $\Theta = \Theta^{S1}$ towards the line $\overline{T_2 S_2}$, repeating the cycle.

5.2.4 Obtaining an exact expression for $\bar{\omega}$

It is possible to obtain an expression for the mean angular velocity from the angular differential equation

$$I\ddot{\theta} = A_e \sin(\omega_e t + \phi_i) - A_{Si}, \tag{5.6}$$

which is valid during sliding. In equation (5.6), $I = mR^2/2$ is the moment of inertia of the disk, and $i = 1$ if sliding at S_1, or $i = 2$ if sliding at S_2. We have introduced the

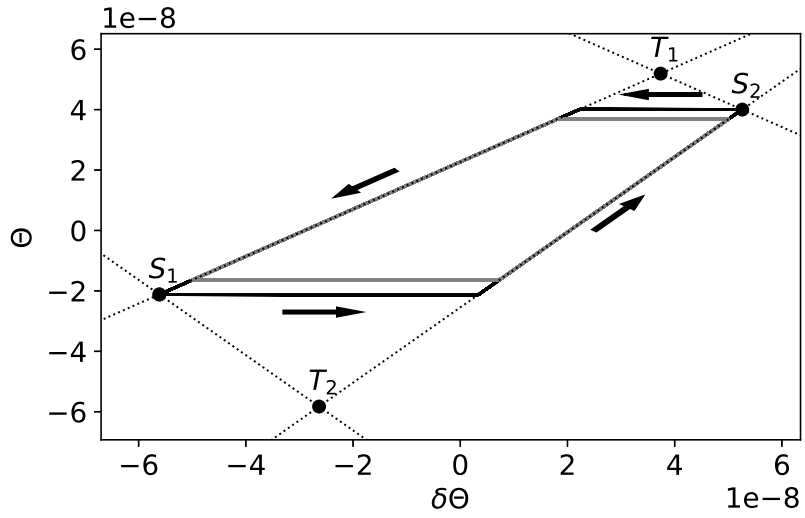

Figure 5.6: Paths traced in $(\delta\theta, \Theta)$ space traced during two numerical simulations under external torque excitation. Dotted lines and points delimit the admissible region in this space as defined in Section 4.4. The gray line corresponds to a simulation with $A_e = 0.100 < A_{S2}$ in the no-sliding regime. The black line corresponds to a simulation with $A_e = 0.113 > A_{S1}$ in the bidirectional sliding regime.

phase $\phi_i = \arcsin(A_{Si}/A_e)$ to set the time at which both contacts start sliding to $t = 0$. Integrating equation (5.6) we find the angular velocity of the disk

$$I\omega = -\frac{A_e}{\omega_e}\cos(\omega_e t + \phi_i) - A_{Si}t + \frac{A_e}{\omega_e}\cos\phi_i. \tag{5.7}$$

Integrating again we can find the equation of motion for the angle θ, while sliding at S_i, as

$$I\theta = -\frac{A_e}{\omega_e^2}\sin(\omega_e t + \phi_i) - \frac{A_{Si}t^2}{2} + \frac{A_e}{\omega_e}\cos\phi_i t + \frac{A_e}{\omega_e^2}\sin\phi_i. \tag{5.8}$$

After some time sliding, the torque decreases below the Amonton's limit, and friction forces eventually stop the disk. The time at which the disk stops, t_{si}, can be obtained by equating equation (5.7) to zero and solving for t. Unfortunately, this can only be done numerically. Once we have found t_{si}, we can obtain the net angular displacement $\Delta\theta_i = \theta(t_{si})$ from

equation (5.7). Finally, the mean angular velocity can be obtained from equation (5.2) as

$$\bar{\omega} = \begin{cases} \frac{1}{2\pi m R^2 \omega_e A_{S2}} (A_{S2} - \mathcal{T}_e(t_{s2}))^2 & \text{(unidirectional sliding)} \\ \frac{1}{2\pi m R^2 \omega_e} \left[\frac{(A_{S2} - \mathcal{T}_e(t_{s2}))^2}{A_{S2}} - \frac{(A_{S1} + \mathcal{T}_e(t_{s1}))^2}{A_{S1}} \right] & \text{(bidirectional sliding)} \end{cases} \tag{5.9}$$

where $\mathcal{T}_e(t)$ is the external torque at time t.

A numerical evaluation of equation (5.9) agrees very well with numerical simulations of the 3-disk system. Figure 5.7 is a reproduction of Figure 5.2, with the lines connecting the data points replaced by equation (5.9).

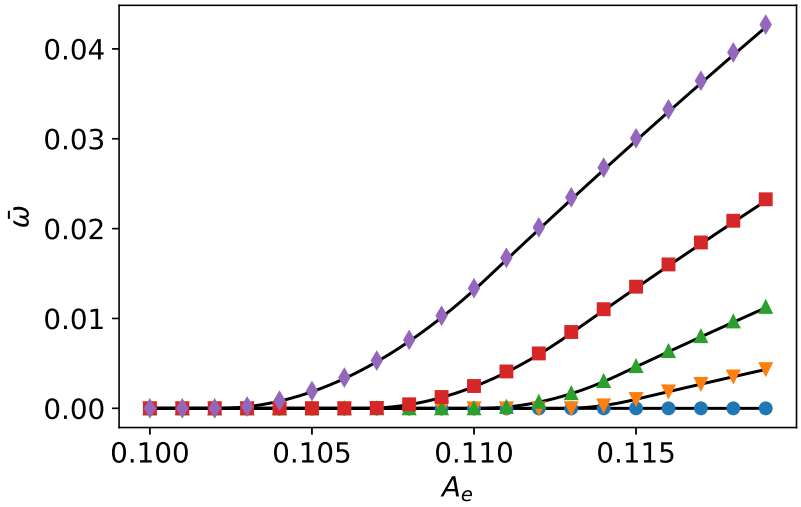

Figure 5.7: Numerical simulation results for the mean rotational velocity $\bar{\omega}$ of the upper disk (data points) compared with predictions from equation (5.9) (lines). Different lines correspond to different values of system tilt with respect to gravity, $\theta_T = 0\pi$ (circles), $\theta_T = 0.03\pi$ (triangles pointing down), $\theta_T = 0.06\pi$ (triangles pointing up), $\theta_T = 0.09\pi$ (squares), $\theta_T = 0.12\pi$ (diamonds). Simulations agree very well with numerical evaluations of equation (5.9)

5.3 Random Vibrational Excitation

We now discuss the more realistic situation in which the supporting disks vibrate randomly. For this type of excitation the assumption of quasistaticity is no longer valid, and a different analysis is required. Furthermore, as will be discussed, when the supports are vibrated, the upper disk rotates in the a direction opposite to the one observed when applying an external torque to the system. We end the section with the introduction of a simplified model that gives some insight on the origin of this sign difference.

5.3.1 Implementation Details of the Vibration

Random vibration is numerically implemented as follows: The center and angular position of each of the two support disks are simulated as a white-noise-forced harmonic oscillator. Each of the support disk coordinates, x_b, y_b, and θ_b, follow the same stochastic differential equation. For x_b this equation reads

$$\ddot{x_b}(t) + 2c\omega_b \dot{x_b}(t) + \omega_b^2 x_b(t) = \xi(t), \tag{5.10}$$

where c is the damping ratio, ω_b is the natural frequency of oscillation, and $\xi(t)$ is the acceleration due to the random forcing with mean $\langle \xi(t) \rangle = 0$ and correlation $\langle \xi(t+\tau)\xi(t) \rangle = D\delta(\tau)$. The parameters ω_b, c, and D are related to the mean square displacement $\langle x_b^2 \rangle$ and mean square velocity $\langle \dot{x_b}^2 \rangle$ by the equations [46]

$$\langle x_b^2 \rangle = \frac{D}{4c\omega_b^3} \tag{5.11}$$

$$\langle \dot{x_b}^2 \rangle = \frac{D}{4c\omega_b} = \langle x_b^2 \rangle \omega_b^2. \tag{5.12}$$

The length and time scales of the oscillations are given by $\sqrt{\langle x_b^2 \rangle}$ and ω_b, which, in turn, determine the typical velocity $\sqrt{\langle \dot{x_b}^2 \rangle}$. This amounts to fixing two of the three parameters of equation (5.10). The third parameter determines the correlation time $t_c = 1/c\omega_b$. The correlation time t_c determines the rate of exponential decay of correlations in the movement

of the supports, for example, in the xx correlation function [46]

$$\langle x_b(t)x_b(t+\tau)\rangle = \left\langle x_b^2 \right\rangle \exp\left(-\frac{|\tau|}{t_c}\right) \left(\cos(\sqrt{1-c}\omega_b|\tau|) + \frac{c}{\sqrt{1-c}}\sin(\sqrt{1-c}\omega_b|\tau|)\right). \tag{5.13}$$

In the simulation, the vibration is specified by the value of the RMS displacement $A_b = \sqrt{\langle x_b^2\rangle} = \sqrt{\langle y_b^2\rangle} = R\sqrt{\langle \theta_b^2\rangle}$, the natural frequency ω_b, and the damping ratio c. Chosen values for the damping ratio and the frequency are $c = 0.5$ and $\omega_b = 20\pi$. Different values of A_b and tilt θ_T were explored.

5.3.2 Numerical Simulations

Figure 5.8 shows the upper disk mean angular velocity $\bar{\omega}$ vs the amplitude A_b, for several values of system tilt θ_T. For $\theta_T = 0$, the disk does not rotate, since conditions at both contacts are symmetric. Rotation does appear for other values of θ_T. An important difference with respect to the quasistatic excitation is the sign of the rotational velocity. Under random vibration, angular velocity is opposite in sign to the case of an applied harmonic torque (Section 5.2).

In contrast to the quasistatic excitation of Section 5.2, large vibrating amplitudes may cause contacts between to disks to open. Since in this chapter we are only concerned with the situation of lasting contacts, data points for which contacts open during the simulation are not plotted in the figures. A discussion of rotation in the regime of a bouncing disk can be found in Chapter 6 and in [26]. From Figure 5.8, we can see that increasing θ_T decreases the value A_b of the last data point. Tilting the system makes it easier for contact 2 to open, we have not plotted points for which this happens.

Figure 5.9 shows the upper disk mean angular velocity $\bar{\omega}$ vs the system tilt θ_T for several values of amplitude A_b. Data points where contacts opened during the simulation are omitted. Since the angle at which disk detaches decreases as A_b increases, contacts start breaking earlier with increasing A_b.

While the evolution of the velocity with amplitude is monotonic until detachment (see Figure 5.8), this is not the case when tilting the system. As θ_T increases from zero, the

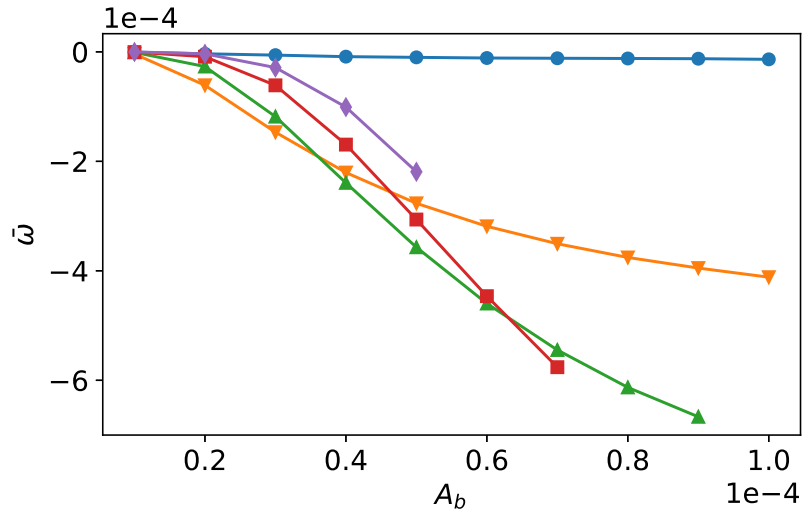

Figure 5.8: Numerical simulation results for the mean rotational velocity $\bar{\omega}$ of the upper disk vs the RMS amplitude A_b of the vibrating support disks. Different lines correspond to different values of system tilt with respect to gravity, $\theta_T = 0\pi$ (circles), $\theta_T = 0.02\pi$ (triangles pointing down), $\theta_T = 0.04\pi$ (triangles pointing up), $\theta_T = 0.06\pi$ (squares), $\theta_T = 0.08\pi$ (diamonds).

velocity first decreases, it reaches a minimum, and then starts increasing again towards zero.

5.3.3 A general mechanism for rotation

Numerical results from Sections 5.2.2 and 5.3.2 serve as two particular examples of how different methods of exciting the system cause rotation in opposite directions. In Section 5.2, we explained the mechanism by which an external torque imposes a positive mean rotational velocity on the upper disk. There, we showed that the asymmetry required to accumulate rotation comes from the fact that the magnitude of the friction force, acting on the upper disk when the disk is sliding counterclockwise, is different from the magnitude of the friction force when the disk is sliding clockwise.

When the support disks are randomly vibrated, numerical results from Section 5.3.2 show that the upper disk rotates clockwise, meaning that the direction of rotation is reversed

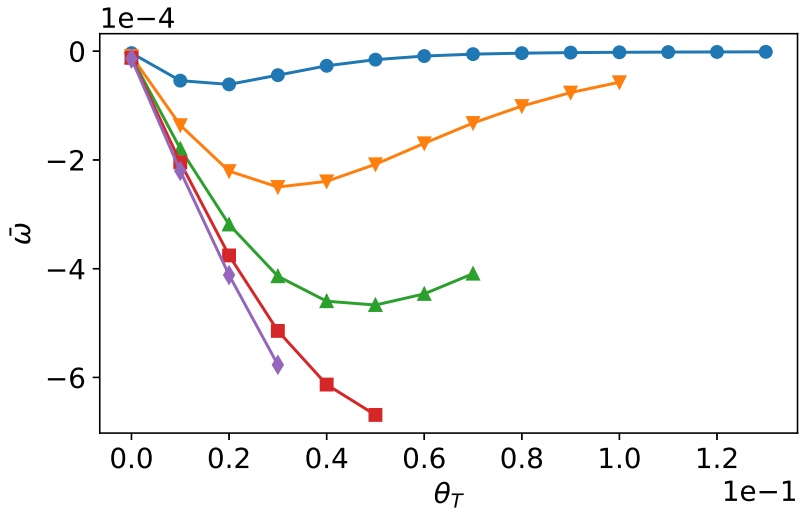

Figure 5.9: Numerical simulation results for the mean rotational velocity $\bar{\omega}$ of the upper disk vs the system tilt θ_T. Different lines correspond to different values of amplitude RMS A_b of the support vibrations, $A_b = 2 \times 10^{-5}$ (circles), $A_b = 4 \times 10^{-5}$ (triangles pointing down), $A_b = 6 \times 10^{-5}$ (triangles pointing up), $A_b = 8 \times 10^{-5}$ (squares), $A_b = 1 \times 10^{-4}$ (diamonds).

with respect to case of an externally applied torque. In this Section, we argue that the cause of this direction reversal comes from the fact that randomly displacing the support disks allows the system to access the complete set $\{S_1, S_2, T_1, T_2\}$ of sliding configurations of the two contacts. This is, while under the effect of the external torque the system was only allowed to reach the points S_1 and S_2 of the bounding quadrilateral of Figure 4.3, for random vibration of the supports, the points T_1 and T_2 are also accessible. At S_1 and S_2 both tangential forces are of the same sign, positive for S_1, and negative for S_2. At T_1, the tangential force at contact 1 is negative ($\tau_1 < 0$) and the tangential force at contact 2 is positive ($\tau_2 > 0$). At T_2 the opposite is true, $\tau_1 > 0$ and $\tau_2 < 0$.

The reason T_1 and T_2 are now accessible is that the support disks are able to move independently. If the relative position of the supports was fixed, for example, if they were joined by a rigid bar, the tangential displacements between each support and the upper disk would always be the same. This joint rigid displacement of the supports cannot cause

tangential forces of opposite sign. This is equivalent to the situation of exciting the disk with an external torque, with the difference that under the influence of the torque, it is the upper disk that moves and the supports remain fixed. On the other hand, when the movement of the supports is independent and uncorrelated, tangential displacements between the supports and the upper disks can be opposite. Under these conditions, cases of contacts sliding in opposite directions occur frequently.

The stochastic nature of the vibration makes it impossible to solve the dynamics in a similar manner to that employed in Section 5.2 to explain the rotation under the influence of an external torque. Instead we aim to obtain a qualitative understanding of the mechanism that causes rotation. To do this, we first need to make a some approximations. We first assume that contacts are always sliding. To justify this assumption we perform the following analysis: From Figure 5.8, we can approximate the value of A_b, at which the disk starts to rotate, at around $A_b \approx 1 \times 10^{-5}$. Given that normal forces are of order $\sim mg$, the relative displacement needed to reach the Amonton's limit, L, is of order $L \sim \mu mg/k_t$. For our simulation parameters, $L \sim 1 \times 10^{-7}$. This makes the typical amplitude of the vibration A_b at least two orders of magnitude larger than the displacement needed to initiate sliding at a contact. These relative large displacements of the supports occur during a mean time given by the correlation time t_c of order $t_c \sim 1/c\omega_b \approx 3 \times 10^{-2}$. This correlation time is much larger than the natural period of the elastic oscillations of the upper disk, of order $\sim \sqrt{m/k_t} \approx 3 \times 10^{-4}$. For a contact that has just finished sliding and is entering the elastic regime, it will likely stay in the elastic phase for about half a period of oscillation before starting to slide in the opposite direction. Sliding is maintained until the tangential velocity of the upper disk and the support, at the point of contact, become equal again. This typically occurs when the support starts to reverse its tangential motion. Since the correlated motion of the support is maintained in average during an time interval of length t_c, this makes the sliding phase much longer than the elastic phase. Under these circumstances we can safely ignore the duration of the elastic phase.

Ignoring the duration of elastic oscillations at the contacts, the dynamics of the system can be approximated as a random series of intervals at which the disk slides alternately at points S_1, S_2, T_1 and T_2. During each of these intervals, there is a torque acting on the upper disk. This torque is not constant, normal forces are constantly changing due to the

vibration of the supports, but if we call $\bar{\mathcal{T}}_i$ the mean torque acting during interval i, we can obtain the mean torque acting on the upper disk during a total of N different sliding intervals as

$$\bar{\mathcal{T}} = \frac{1}{t_T} \sum_{i=1}^{N} \bar{\mathcal{T}}_i t_i, \tag{5.14}$$

where t_i is the duration of the sliding interval i and $t_T = \sum_{i=1}^{N} t_i$.

Calculating each torque $\bar{\mathcal{T}}_i$ is not easy, but we can find some suitable approximation. The torque acting on the disk during each of this sliding intervals is given by the sum of both tangential forces. Since we are assuming contacts are always sliding, tangential forces are saturated at the Amonton's limit, and the total torque is given by $\mathcal{T} = \mu(\mathrm{sgn}\,(\tau_1)\, n_1 + \mathrm{sgn}\,(\tau_2)\, n_2)$. Normal forces are constantly changing due to the vibration of the supports, but fluctuations are not completely random. The normal force at a contact is determined by the normal relative distance between the upper disk and the support (see equation (4.2)). This distance changes whenever either of the disks move. Thus, we can distinguish two causes for the fluctuations of the normal forces, one caused by the movement of the support, and other caused by the movement of the upper disk. We will ignore the fluctuations on the normal force caused by the random vibration of the support disk. The normal displacement of the support disk is assumed random and uncorrelated with the contact status (sliding or not-sliding), and thus is not expected to be the source of drift. The main purpose of the vibration is to facilitate sliding, mainly through the tangential motion of the supports.

The displacement of the upper disk couples forces from both contacts in the 3-disk system in the sense that forces on contact 1 influence forces at contact 2 and vice-versa. This introduces correlations in the fluctuations of contact forces. During each sliding interval, contact forces try to bring the system to translational equilibrium, although this equilibrium is actually never achieved. Random vibration and the continuous switching of sliding configurations keeps the system in a dynamical state out of equilibrium. But, as an approximation, we can use the equilibrium values of contact forces at each sliding point to estimate a the value of the mean torque during each respective interval. We can obtain the equilibrium torque values from equation (4.18) using the value of $\delta\theta$ for each sliding point from equations (4.41), (4.43), (4.47) and (4.49), and setting $\ddot{x} = \ddot{y} = 0$:

$$\bar{\mathcal{T}}^{S_1} = \frac{mgR\mu(\cos\theta_T + \mu\sin\theta_T)}{(1+\mu^2)\cos\theta_h}, \tag{5.15}$$

$$\bar{\mathcal{T}}^{S_2} = -\frac{mgR\mu(\cos\theta_T - \mu\sin\theta_T)}{(1+\mu^2)\cos\theta_h}, \tag{5.16}$$

$$\bar{\mathcal{T}}^{T_1} = \frac{mgR\mu\sin\theta_T}{\sin\theta_h + \mu\cos\theta_h}, \tag{5.17}$$

$$\bar{\mathcal{T}}^{T_2} = -\frac{mgR\mu\sin\theta_T}{\sin\theta_h - \mu\cos\theta_h}. \tag{5.18}$$

Since the torques defined in equations (5.15) through (5.18) are constant, equation (5.14) for the mean torque becomes

$$\begin{aligned}\bar{\mathcal{T}} =& \frac{1}{t_T}\left(\bar{\mathcal{T}}^{S_1}\sum_{i=1}^{N^{S_1}} t_i + \bar{\mathcal{T}}^{S_2}\sum_{i=1}^{N^{S_2}} t_i + \bar{\mathcal{T}}^{T_1}\sum_{i=1}^{N^{T_1}} t_i + \bar{\mathcal{T}}^{T_2}\sum_{i=1}^{N^{T_2}} t_i\right) \\ =& \frac{1}{t_T}\left(N^{S_1}\bar{\mathcal{T}}^{S_1}\bar{t}^{S_1} + N^{S_2}\bar{\mathcal{T}}^{S_2}\bar{t}^{S_2} + N^{T_1}\bar{\mathcal{T}}^{T_1}\bar{t}^{T_1} + N^{T_2}\bar{\mathcal{T}}^{T_2}\bar{t}^{T_2}\right),\end{aligned} \tag{5.19}$$

where N^j is the number of intervals the system spends at the sliding point j, and $\bar{t}^j$ is the mean time of interval j, defined as $\bar{t}^j = \frac{1}{N^j}\sum_{i=1}^{N^j} t_i$. For a unbiased random vibration it is reasonable to assume $N^j = N/4$ for all four sliding configurations, which further simplifies equation (5.19) to

$$\bar{\mathcal{T}} = \frac{1}{4\bar{t}}\left(\bar{\mathcal{T}}^{S_1}\bar{t}^{S_1} + \bar{\mathcal{T}}^{S_2}\bar{t}^{S_2} + \bar{\mathcal{T}}^{T_1}\bar{t}^{T_1} + \bar{\mathcal{T}}^{T_2}\bar{t}^{T_2}\right), \tag{5.20}$$

where $\bar{t} = t_T/N$ is the mean time of a sliding interval averaged over all intervals, independently of their sliding configuration.

In numerical simulations it is observed that the upper disk has a well defined and stationary mean rotational velocity. This condition requires that the mean torque on the upper disk be zero, $\bar{\mathcal{T}} = 0$. For a particular tilt θ_T, the torques $\mathcal{T}^j$ in equation (5.20) are constant, thus, to balance the torque, the mean duration $\bar{t}^j$ of each sliding interval must be such that they satisfy $\bar{\mathcal{T}} = 0$. This means tilting the system modifies the duration of the siding intervals, in turn modifying the mean rotational velocity.

When the tilt angle $\theta_T = 0$, $\bar{\mathcal{T}}^{S_1} = -\bar{\mathcal{T}}^{S_2}$ and $\bar{\mathcal{T}}^{T_1} = \bar{\mathcal{T}}^{T_2} = 0$, as calculated from equations (5.15) trough (5.18). In this situation, symmetry requires that all $\bar{t}^j$ are equal. The mean total torque is zero, and the mean rotational velocity is also zero. As we slightly tilt the system, initially, all times $\bar{t}^j$ will remain equal. The total torque mean on the system is just the average of all torques $\bar{\mathcal{T}}^j$ in equations (5.15) trough (5.18), but now evaluated at $\theta_T \neq 0$. This mean torque is

$$\bar{\mathcal{T}}^* = \frac{mgR\mu^2(\mu^2 + (1+\mu^2)\cos 2\theta_h)\sec^3\theta_h \sin\theta_T}{2(1+\mu^2)(\mu^2 - \tan^2\theta_h)}. \tag{5.21}$$

The torque $\bar{\mathcal{T}}^*$ is always negative for the parameter values used in our simulations. This means, upon tilting, a negative mean torque will act on the upper disk. The mean rotational velocity will decrease until the changes in the times $\bar{t}^j$ balance out the mean torque to zero again. This explains why the rotational velocity is negative when the supports are vibrated randomly. If the sliding points T_1 and T_2 where not accessible, the torque upon tilting $\bar{\mathcal{T}}^*$ would be the average of $\bar{\mathcal{T}}^{S_1}$ and $\bar{\mathcal{T}}^{S_2}$ alone. This restricted average is positive, leading to a positive rotational velocity of the upper disk upon tilting.

6 A bouncing disk on a wedge

In this Chapter we present experimental and numerical results regarding the one disk model in the regime of moderate excitation, or "gas phase". The study is that of a viscoelastic frictional disk bouncing on a wedge billiard that is vibrated vertically. Unlike the analysis of Chapter 5, in this regime contacts are frequently broken and the disk spends most of the time detached from the supporting surface. Both supports are assumed to undergo a prespecified harmonic vibrational motion, while the position and angle of the upper disk constitute dynamical degrees of freedom. The contents of this Chapter have been published in reference [26].

If the supports consist of two disks, this toy packing only makes sense for rather weak vibration intensities of the bottom, since the upper disk is not confined and can escape. Whenever the bottom excitation is sufficiently weak, the upper disk will barely move from its lowest potential energy position, and therefore the curvature of the supporting disks will not be relevant. A further simplification of this model, that is appropriate for the case of moderate excitation, consists in replacing the two supporting disks by two straight lines, thus forming a wedge with aperture angle $\theta_W = 2\pi/3$ (see Figure 4.1).

Although billiards on a wedge under gravity have been considered in the past [41, 42, 47–50], their rotational behavior was never studied before. Conservative point-like gravitational billiards on a wedge, with variable aperture θ_W and zero tilt $\theta_T = 0$, were first studied by Lehtihet and Miller [47]. For narrow wedges, where $\theta_W < \pi/2$, the phase space space exhibits stable periodic orbits surrounded by chaos, with the chaotic orbits passing arbitrarily close to the wedge vertex. For wide wedges, $\theta_W > \pi/2$, the system is always ergodic. In fact, these authors found that the case of $\theta_W = 2\pi/3$, corresponding to our three-disk toy-system (see later), displays the strongest stochasticity. This conservative wedge billiard was further studied by Richter et al [48], who found that there is breathing

chaos as θ_W varies. The Lyapunov exponent attains minima at a sequence of discrete values of θ_W. An experimental realization of this system was obtained by Milner et al. [49] in an optical billiard with ultracold atoms. Good agreement was found between experiment [49] and previous numerical simulations [47, 48].

A dissipative version of these billiards was studied experimentally in a work by Feldt and Olafsen [50], where a steel ball bounces on a horizontally driven aluminum surface with parabolic, wedge or hyperbolic shape. None of the these works considered rotation. A first attempt at an analytic description of these systems is done by Gorski and Srokowski [41]. The authors considered a horizontally oscillating billiard, and derived a map for velocities and positions at each collision. This map is then used to simulate the dynamics. Their model assumes a velocity-dependent normal restitution coefficient and ignores friction, thus, ignoring rotation altogether.

A more recent numerical study of the inelastic gravitational billiard was done by Hartl et al. [42]. The authors studied inelastic gravitational billiards with parabolic, wedge and hyperbolic walls. A comparison with the experimental results by Feldt and Olafsen [50] is made. Their model includes friction and air drag. However, a study of rotational behavior is not reported by those authors.

We briefly report experimental results obtained with a setup of three metallic disks, with the main purpose of demonstrating that the phenomenon of spontaneous rotation in a wedge billiard is observed in reality, and is not an artifact of our numerical simulations. We then focus on the description of numerical results obtained by two different algorithms: molecular dynamics (MD) of frictional elasto-plastic disks, and event-driven (ED) simulation. The good quantitative coincidence between these two methods, plus the qualitative similarity to our laboratory results, supports the notion that our numerical description is sound and able to capture the essential mechanisms underlying spontaneous rotation.

Section 6.1 describes our experimental setup and presents a brief account of rotational observations using three-disks in the laboratory. Section 6.2 presents the details of our Molecular Dynamics (MD) simulations, and describes some results for the average rotational velocity versus the wedge tilt. In Section 6.3, the assumptions and methodology behind our Event Driven (ED) simulations are introduced. Section 6.3.2 discusses the fact that the mapping behind ED can be seen to be explicitely scale invariant, and Section 6.3.2

demonstrates explicitely that the rotational velocity of the disk scales as the typical velocity v_b of the vibrating bottom. Section 6.3.3 shows that MD and ED methods produce equivalent results. Section 6.3.4 presents numerical results from ED simulations, discussing the effect of several system parameters on rotational velocity.

6.1 Experimental results

The simple three-disk setup used in our experiments is depicted in Fig. 6.1. Three identical, 2.5cm in diameter, 1cm thick, stainless-steel disks (A, B, C) are used to demonstrate rotational drift in a laboratory realization of our toy model. All three disks have sand-blasted contact surfaces, and they all have a 0.8 cm diameter hole drilled through their center. Two supporting disks (A, B) touch each other and are fixed in place between two clear acrylic plates of 3mm thickness and of size 6x4.5cm each. Washers (W_1, W_2) are used to provide a slight amount of extra spacing between the disks and the acrylic plates. The third, free to move, disk (C) rests on top of disks A, B. The whole setup is attached to an L-shaped aluminum profile (P) with bolts (B_1, B_2) that pierce through the centers of the supporting disks (A, B). The L-shaped profile P is in turn bolted (B_3) to a similar profile (Q) that is attached to a Taika TK-W102D 300W-10inch diameter loudspeaker. The three-disk setup can be tilted by loosening B_3 and then retightening it. The tilt angle θ_T is measured using a protractor (S). The third disk C is masked with a white paper sticker and has a black rectangular mark (M) on its camera-facing side, allowing us to track rotations with image-processing software. Because the washers provide a small amount of extra space between the acrylic sheets, the top disk C is free to rotate and move on the plane of the sheets.

The speaker is driven by a sinusoidal wave provided by an Agilent 33220A waveform generator, amplified through a Mitzu MPA2100 amplifier. We explored several frequency ranges and intensities for the driving, but the illustrative results reported in this Chapter were obtained with a 200 Hz signal. The signal strength is set strong enough to keep the upper disk slightly bouncing on its contacts when the tilt θ_T is zero. In a typical measurement run, a webcam takes pictures at one-second intervals during five minutes. To extract rotation data, the pictures are later processed using the "analyze particles" feature

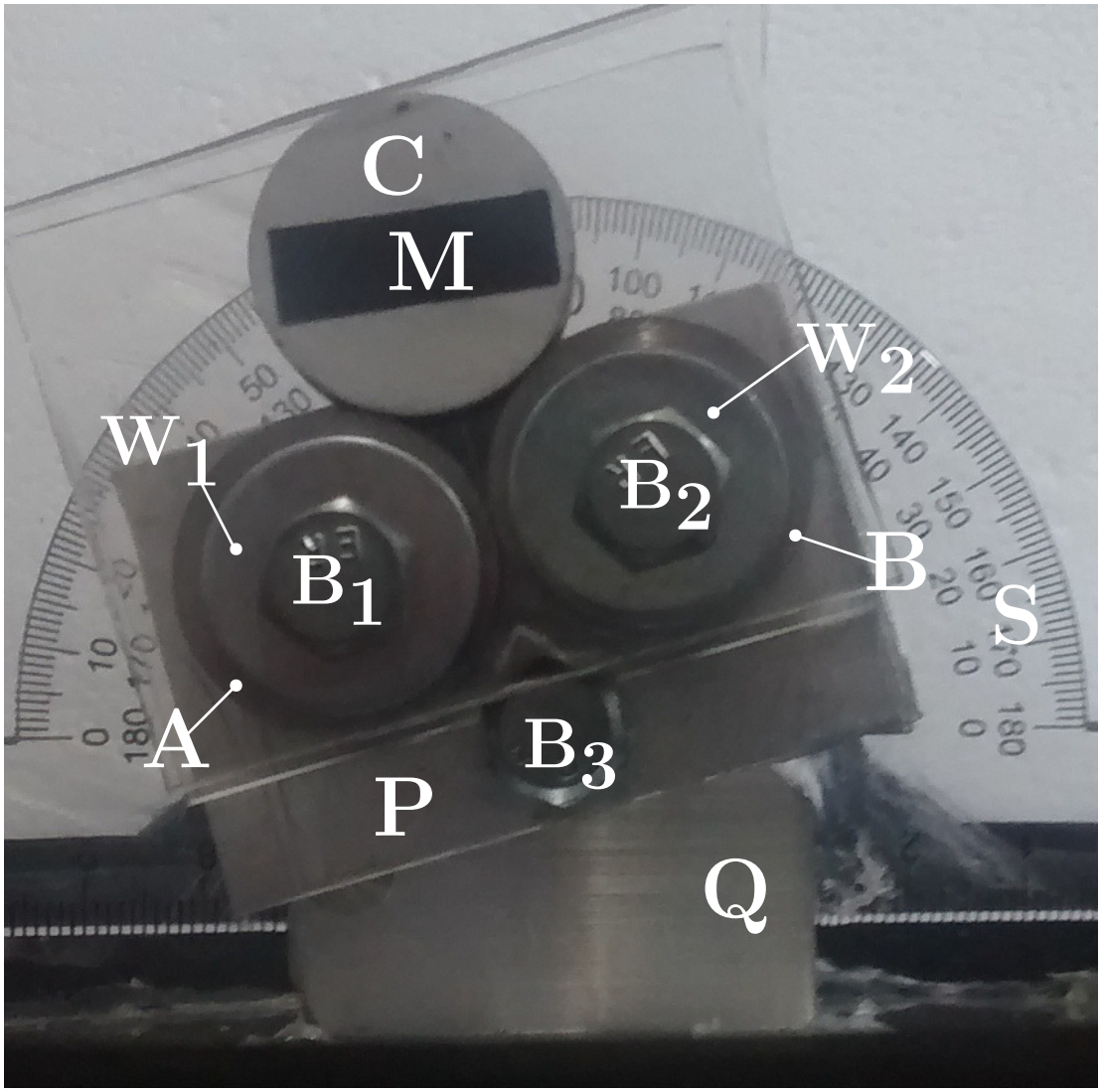

Figure 6.1: Photography of the experimental setup used to verify spontaneous rotation in the three-disk setup. Disk C rotates due to repetitive bounces off disks A and B. The aluminum profile Q is attached to a sinusoidally vibrating loudspeaker which provides the driving.

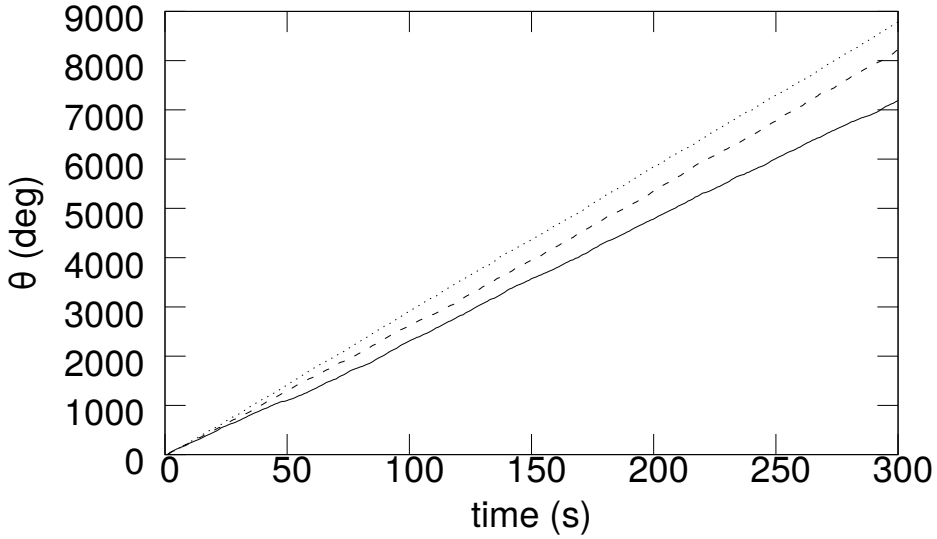

Figure 6.2: Evolution of the angular variable θ of the upper disk, recorded during five minutes, for three different tilt angles: $\theta_T = 8$ (solid line), $\theta_T = 12$ (dashed line) and $\theta_T = 16$ (dotted line). Images are taken at one-second intervals and later processed using image-recognition software.

from the Fiji software [31]. The image sequence is fed through the software, which in turn processes the images, identifies the black rectangular mark of the upper disk C, and fits an ellipse to it. The fitted parameters that define the spatial location of the ellipse are then saved to a file and processed to obtain the time series for the rotation angle $\theta(t)$ for disk C.

Measured rotation angles vs time, from experimental runs with wedge-tilts θ_T of 8, 12 and 16 degrees are plotted in Figure 6.2. For zero tilt, our setup is symmetric and no rotation is expected. We verified that the overall rotation is very small in this case, and the rotational behavior is essentially random (not ballistic), for zero tilts. Our experimental results show that sustained rotation is real and can be reproducibly realized in the laboratory. For nonzero tilts, the disk is seen to rotate with an average velocity $\bar{\omega}$ that depends on tilt and on the intensity of the driving. We study the details of this phenomenon numerically in the following sections.

6.2 Molecular dynamics simulations

As a first numerical investigation of wedge billiards, we implemented Molecular Dynamics (MD) simulations [28] for a disk in a vertically vibrated wedge and for a disk supported by two vibrating disks. These two cases were found to differ only for high intensity excitation, because in that case the upper disk starts to "feel" the curvature of its supporting disks, eventually falling out of place if the excitation is too large. We concentrate here on the description of the wedge results alone. This setup has the property (see Section 6.3.2) of being scale invariant.

Our simulations consider a disk interacting via elastic, viscous and frictional forces with two straight lines forming a wedge, as shown in Figure 4.1 (right). Forces are defined as discussed in Section 4.2. Besides contact forces from the wedge walls, the disk experiences a downward gravitational acceleration of magnitude $g = 9.81m/s^2$. In collisions against the wedge, the normal coefficient of restitution e_n [44] is a material constant that depends on k_n, γ and m. In our simulations we often use $e_n = 0.9$, and $\kappa = k_t/k_n = 0.773$. The time step Δt for MD integration (a fifth-order predictor-corrector algorithm is used) is set to a hundredth of the "collision time" [44] $t_{col} = -2m \ln e_n/\gamma_n$. This ensures that

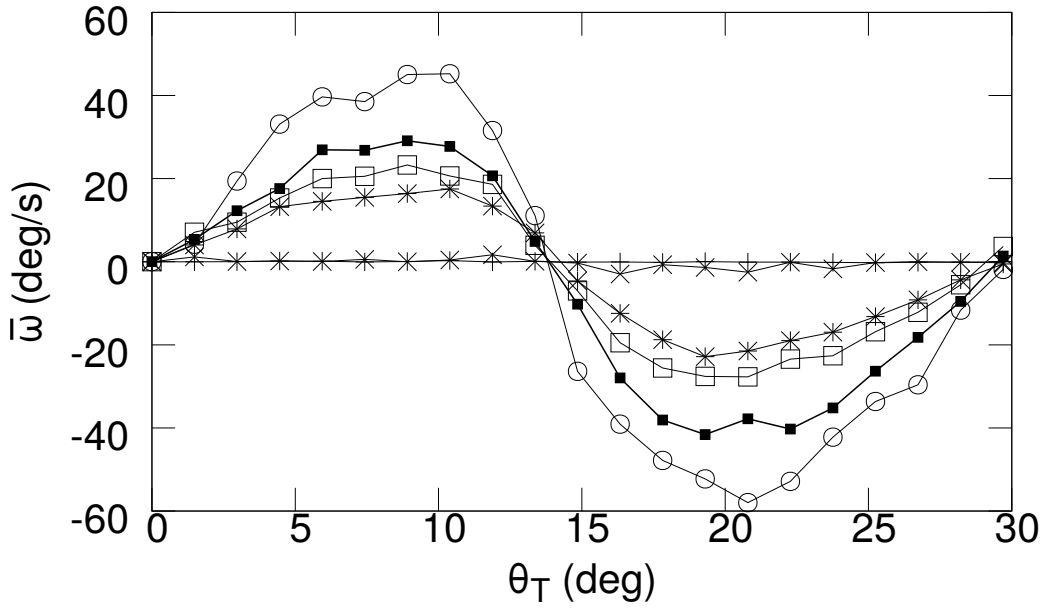

Figure 6.3: Molecular simulations numerical results for the mean rotational velocity of a disk bouncing in a wedge for different values of the dimensionless acceleration of the wedge Γ. Values shown are $\Gamma = 0.9$ (plusses), $\Gamma = 1.0$ (crosses), $\Gamma = 1.2$ (asterisks), $\Gamma = 1.5$ (empty squares), $\Gamma = 2.0$ (filled squares), $\Gamma = 3.0$ (circles). Other simulation parameters are $k_n = 4.5e6N/m$, $\kappa = 0.773$, $R = 0.02m$, $\gamma = 9.84kg/s$, $\mu = 0.1$, $m = 4.5g$. The wedge is vibrating at $80Hz$.

collisions are described with enough numerical accuracy. Relevant system parameters are: the wedge aperture angle θ_W, the gravitational acceleration g, the typical wedge velocity v_b, the mass m of the disk, the normal coefficient of restitution e_n, the frictional coefficient μ, the normal elastic coefficient k_n, and the tangential elastic coefficient k_t.

A sinusoidal vertical motion, with angular frequency ω_b and amplitude A, is imposed on the wedge. The maximum dimensionless acceleration is then $\Gamma = A\omega_b^2/g$, and the maximum bottom velocity is $v_b = A\omega_b$. The average rotational velocity $\bar{\omega}$ of the disk is then measured numerically over a time-window of 300 seconds. The mean rotational velocity $\bar{\omega}$ is plotted against tilt θ_T for different values of Γ in Fig. 6.3. For $\Gamma \leq 1$, the disk remains in contact with the wedge most of the time, and the rotation is too small to be measurable on this time scale. For $\Gamma > 1$, a regime appears where $\bar{\omega}$ scales linearly with v_b. In this regime, the disk is bouncing on the wedge, experiencing mainly binary collisions of negligible duration compared to the mean flight time $\bar{t}_{flight}$. This is the regime we set to describe in this Chapter. The case of $\Gamma < 1$, where the disks remains in contact with the wedge, also gives rise to rotation, but with a much smaller velocity. That case admits an approximate analytic description, and was described in Chapter 5. In this Chapter, we concentrate on the description of spontaneous rotation in the $\Gamma > 1$ phase. Fig. 6.3 shows that, in this phase, the mean rotational velocity $\bar{\omega}$ of the disk is not a monotonic function of tilt θ_T, and may change direction as the tilt is increased. Notice that the actual shape of the function $\bar{\omega}(\theta_T)$ depends strongly on system parameters, particularly so on the value of the friction coefficient μ (See Fig. 6.6).

6.3 Event-driven simulations

For the case of $\Gamma > 1$, we also implemented event-driven (ED) simulations of the gravitational wedge billiard. The applicability of ED algorithms is limited to the description of dynamical systems dominated by binary collisions of negligible duration in time. These algorithms have, however, the advantage of greatly speeding up simulations in certain cases. For a discussion of ED simulations in the context of granular materials, see for example the book by Pöschel and Schwager [17].

We choose to implement our algorithm as an iterative map that is similar to those used

by Lehtihet and Miller [47] and Richter et al. [48] in their studies of Hamiltonian wedge billiards. Unlike their case, our map considers inelastic collisions and Coulomb friction. The algorithm we use maps the values for positions and velocities of the disk before a collision i to the values before the next collision $i+1$. In particular, we chose to build a four-coordinate mapping for the following four variables of the disk: 1) its pre-collision normal velocity v_n, 2) its pre-collision tangential velocity v_t, 3) its angular velocity ω, and 4) the distance l from the disk center to the wedge bisector.

There are actually two sets of mapping equations; one assuming collision $i+1$ to happen at the same wall as collision i, the other considering a collision with the other wall. In order to choose the correct mapping, the time between collisions t^i_{flight} is calculated for both cases, and the earliest one is chosen. Since ω is constant between collisions, the mean rotational velocity is calculated as

$$\bar{\omega} = \frac{\sum_i \omega_i t^i_{flight}}{\sum_i t^i_{flight}}, \tag{6.1}$$

where t^i_{flight} is the time of flight between collisions $i-1$ and i.

In the MD simulations described in Section 6.2, the wedge moves sinusoidally with frequency ω_b and amplitude A, therefore the maximum bottom velocity is $v_b = A\omega_b$. In ED simulations, in order to calculate the time t_{col}, at which the next collision with the bottom will happen, one must in principle find the intersection of a parabola with a harmonic function of time (the bottom position). This can only be done numerically, which is relatively time-consuming. In order to further speed up simulations, we first tested, and later employed, the fixed-bottom random-phse approximation (FBRPA) described in Section 2.3.3. The FBRPA is valid in the limit of large frequency and small amplitude of excitation: Since the amplitude is assumed small, the spatial location of a collision, and, therefore, the collision time t_{col} itself, are practically unaffected by the motion of the bottom. Hence, within the FBRPA, we assume the bottom to be fixed, and calculate the intersection of the parabolic motion of the disk under gravity with the straight line describing the fixed bottom. This calculation can be easily done analytically.

6.3.1 Derivation of the mapping equations

In this section we give the details of the deviation of the mapping equations. We start by defining a set of three coordinate systems, a standard Cartesian reference frame, with origin at the wedge vertex, and two local reference frames at each wall, with axes in the normal and tangential directions to the wall. Quantities in the Cartesian coordinate system are super-scripted x for the component along the x-axis, and y for the component along the y-axis. Quantities in the local reference frame are super-scripted n for quantities in the normal direction, and t for quantities in the tangential direction. We can transform the disk velocity v, from a local reference frame to the Cartesian reference frame, via the set of equations

$$v^x = -\sin\theta v^n + \cos\theta v^t \tag{6.2}$$

$$v^y = +\cos\theta v^n + \sin\theta v^t, \tag{6.3}$$

where θ is the angle the wall makes with the x-axis. The inverse transformation, from the Cartesian frame to the local frame, is given by equations

$$v^n = -\sin\theta v^x + \cos\theta v^y \tag{6.4}$$

$$v^t = +\cos\theta v^x + \sin\theta v^y. \tag{6.5}$$

In the Cartesian reference frame, the walls of the wedge are described by the equation

$$y = \tan\theta x, \tag{6.6}$$

where $\theta = \theta_L$ for the left wall, and $\theta = \theta_R$ for the right wall. The angles θ_L and θ_R can take values from $-\frac{\Pi}{2}$ to $\frac{\Pi}{2}$.

We want to map quantities from a collision k to the next collision $k+1$. Between collisions, during free flight, the disk experiences gravitational acceleration. We can write equations for quantities at the beginning of collision $k+1$ from the equations for a parabolic

path as

$$x_{k+1} = x_k + v_k'^x t_f \tag{6.7}$$

$$y_{k+1} = y_k + v_k'^y t_f - \frac{g t_f^2}{2} \tag{6.8}$$

$$v_{k+1}^x = v_k'^x \tag{6.9}$$

$$v_{k+1}^y = v_k'^y - g t_f, \tag{6.10}$$

where primed quantities refer to velocities at the end of a collision, un-primed quantities refer to velocities at the beginning of a collision, and t_f is the time of flight. The subscript indicates the collision at which the quantity is measured, either collision k or $k+1$.

Now, we transform equations (6.7) through (6.10) to the local reference frame. Applying the transformations (6.2) and (6.3)

$$x_{k+1} = x_k + (-\sin\theta_i v_k'^n + \cos\theta_i v_k'^t) t_f \tag{6.11}$$

$$y_{k+1} = y_k + (+\cos\theta_i v_k'^n + \sin\theta_i v_k'^t) t_f - \frac{g t_f^2}{2} \tag{6.12}$$

$$v_{k+1}^n = \cos(\theta_f - \theta_i) v_k'^n - \sin(\theta_f - \theta_i) v_k'^t - g t_f \cos\theta_f \tag{6.13}$$

$$v_{k+1}^t = \sin(\theta_f - \theta_i) v_k'^n + \cos(\theta_f - \theta_i) v_k'^t - g t_f \sin\theta_f, \tag{6.14}$$

where θ_i is the angle corresponding to of the wall the path is starting on (either θ_L or θ_R), and θ_f is the angle corresponding to the wall the disk is arriving at.

To find t_f we need the time at which the parabolic path intersects the wall of the wedge. We can find the intersection by solving the system of equations composed of equations (6.6), (6.11) through (6.14), and the energy equation

$$E = \frac{m}{2}\left((v^n)^2 + (v^t)^2\right) + \frac{mR^2}{4}\omega^2 + mgy. \tag{6.15}$$

From this system of equations, we are only interested in the solutions with $t_f > 0$. The

relevant solution for t_f is

$$\begin{aligned} t_f = &\frac{1}{g\cos\theta_f}\Big[\cos(\theta_i-\theta_f)v_k'^n + \sin(\theta_i-\theta_f)v_k'^t \\ &+ \sqrt{[\cos(\theta_i-\theta_f)v_k'^n + \sin(\theta_i-\theta_f)v_k'^t]^2 + 2g\frac{\cos\theta_f}{\sin\theta_i}\sin(\theta_i-\theta_f)y_k}\Big]. \end{aligned} \tag{6.16}$$

Equations (6.12), (6.13) and (6.14), together with the fact that during flight the rotational velocity does not change, define the map equations

$$v_{k+1}^n = -\sqrt{(c_{if}v_k'^n + s_{if}v_k'^t)^2 + 2g\frac{c_f}{s_i}s_{if}y_k} \tag{6.17}$$

$$v_{k+1}^t = \frac{-s_i v_k'^n + c_i v_k'^t}{c_f} + \tan\theta_f v_{k+1}^n \tag{6.18}$$

$$\omega_{k+1} = \omega_k' \tag{6.19}$$

$$y_{k+1} = y_k + \left(c_i v_k'^n + s_i v_k'^t\right)t_f - \frac{gt_f^2}{2}, \tag{6.20}$$

where we have used equation (6.16), and the abbreviations $c_i = \cos\theta_i$, $s_i = \sin\theta_i$, $c_{ij} = \cos(\theta_i - \theta_j)$, and $s_{ij} = \sin(\theta_i - \theta_j)$.

The four different combinations of θ_i and θ_f give four different sets of mapping equations, depending on the identity of the initial and final wall (left or right). For the two cases for which the particles bounces twice on the same wall, $\theta_i = \theta_f = \theta$, the mapping simplifies to

$$v_{k+1}^n = -v_k'^n \tag{6.21}$$

$$v_{k+1}^t = v_k'^t - 2\tan\theta v_k'^n \tag{6.22}$$

$$\omega_{k+1} = \omega_k' \tag{6.23}$$

$$y_{k+1} = y_k - \frac{2\tan\theta v_k'^n}{g}\left(\tan\theta v_k'^n - v_k'^t\right) \tag{6.24}$$

$$t_f = \frac{2v_k'^n}{g\cos\theta}. \tag{6.25}$$

Finally, to write the mapping equations in a form involving only pre-collision quantities,

we use the collision rules given by equations (2.11), (2.23), and (2.24) to obtain

$$v_{k+1}^n = -\sqrt{\left(c_{if}\left(-e_n v_k^n + (1+e_n)v_{b,k}^n\right) + s_{if}\left(v_k^t - \frac{1-e_t}{3}u_k^t\right)\right)^2 + 2g\frac{c_f}{s_i}s_{if}y_k} \tag{6.26}$$

$$v_{k+1}^t = \frac{-s_i\left(-e_n v_k^n + (1+e_n)v_{b,k}^n\right) + c_i\left(v_k^t - \frac{1-e_t}{3}u_k^t\right)}{c_f} + \tan\theta_f v_{k+1}^n \tag{6.27}$$

$$\omega_{k+1} = \omega_k - \frac{2(1-e_t)}{3R}u_k^t \tag{6.28}$$

$$y_{k+1} = y_k + \left[c_i\left(-e_n v_k^n + (1+e_n)v_{b,k}^n\right) + s_i\left(v_k^t - \frac{1-e_t}{3}u_k^t\right)\right]t_f - \frac{gt_f^2}{2} \tag{6.29}$$

$$t_f = \frac{c_{if}\left(-e_n v_k^n + (1+e_n)v_{b,k}^n\right) + s_{if}\left(v_k^t - \frac{1-e_t}{3}u_k^t\right) - v_{k+1}^n}{gc_f}, \tag{6.30}$$

where u is the relative velocity between the disk and the wall, and v_b is the velocity of the wall at the moment of the collision. Coefficients of restitution e_n and e_t are calculated as described in Section 4.5.

6.3.2 A-dimensionalization of the map and scaling

Two relevant parameters in this system are the maximum bottom velocity $v_b^{max} = A\omega_b$, and the gravitational acceleration g, which together define a length-scale $\ell_0 = (v_b^{max})^2/g$, and a time-scale $t_0 = v_b^{max}/g$. All dependences from A, ω_b, and g in the system can be written in terms of these two scales alone. These two scales can be clearly associated, respectively, with the typical height and time-duration of parabolic trayectories described by the disk as it bounces on the wedge. If now all distances are divided by ℓ_0, all times by t_0, and all velocities by $\ell_0/t_0 = v_b^{max}$, the mapping becomes dimensionless. In other words, the two above-mentioned scales disappear entirely from the formulation. Using these new adimensional variables, the system dynamics for the wedge is formulated in terms that are independent of A, ω_b and g. To get, for example, the actual velocities, we would only need to multiply the results obtained from this adimensional system by $A\omega_b$. This scaling is illustrated in Section 6.3.2 numerically.

The bottom velocity v_b is a stochastic variable drawn from a distribution with probabilities that depend only on scaled velocities (see Section 2.3.3). This probability is

independent of the actual velocity $A\omega_b$ and the scaling works with this type of random sampling. Also, e_n is a constant and e_t depends on a ratio of velocities, the coefficients of restitution, being dimensionless quantities, are not affected by the scaling.

The dimensionless mapping equations are then

$$v^n_{k+1} = -\sqrt{\left(c_{if}\left(-e_n v^n_k + (1+e_n)v^n_{b,k}\right) + s_{if}\left(v^t_k - \frac{1-e_t}{3}u^t_k\right)\right)^2 + 2\frac{c_f}{s_i}s_{if}y_k} \tag{6.31}$$

$$\begin{aligned} v^t_{k+1} =& \frac{-s_i\left(-e_n v^n_k + (1+e_n)v^n_{b,k}\right) + c_i\left(v^t_k - \frac{1-e_t}{3}u^t_k\right)}{c_f} \\ &+ \tan\theta_f v^n_{k+1} \end{aligned} \tag{6.32}$$

$$\omega_{k+1} = \omega_k - \frac{2(1-e_t)}{3R}u^t_k \tag{6.33}$$

$$\begin{aligned} y_{k+1} =& y_k - \frac{t_f^2}{2} \\ &+ \left[c_i\left(-e_n v^n_k + (1+e_n)v^n_{b,k}\right) + s_i\left(v^t_k - \frac{1-e_t}{3}u^t_k\right)\right]t_f \end{aligned} \tag{6.34}$$

$$t_f = \frac{c_{if}\left(-e_n v^n_k + (1+e_n)v^n_{b,k}\right) + s_{if}\left(v^t_k - \frac{1-e_t}{3}u^t_k\right) - v^n_{k+1}}{c_f} \tag{6.35}$$

The simplified dimensionless map for collisions upon the same wall is

$$v^n_{k+1} = e_n v^n_k - (1+e_n)v^n_{b,k} \tag{6.36}$$

$$v^t_{k+1} = \left(v^t_k - \frac{1-e_t}{3}u^t_k\right) + 2\tan\theta_i\left(e_n v^n_k - (1+e_n)v^n_{b,k}\right) \tag{6.37}$$

$$\omega_{k+1} = \omega_k - \frac{2(1-e_t)}{3R}u^t_k \tag{6.38}$$

$$\begin{aligned} y_{k+1} =& y_k - 2\tan\theta_i\left(e_n v^n_k - (1+e_n)v^n_{b,k}\right) \\ &\left(\tan\theta_i\left(e_n v^n_k - (1+e_n)v^n_{b,k}\right) + \left(v^t_k - \frac{1-e_t}{3}u^t_k\right)\right) \end{aligned} \tag{6.39}$$

$$t_f = 2\frac{(1+e_n)v^n_{b,k} - e_n v^n_k}{c_i} \tag{6.40}$$

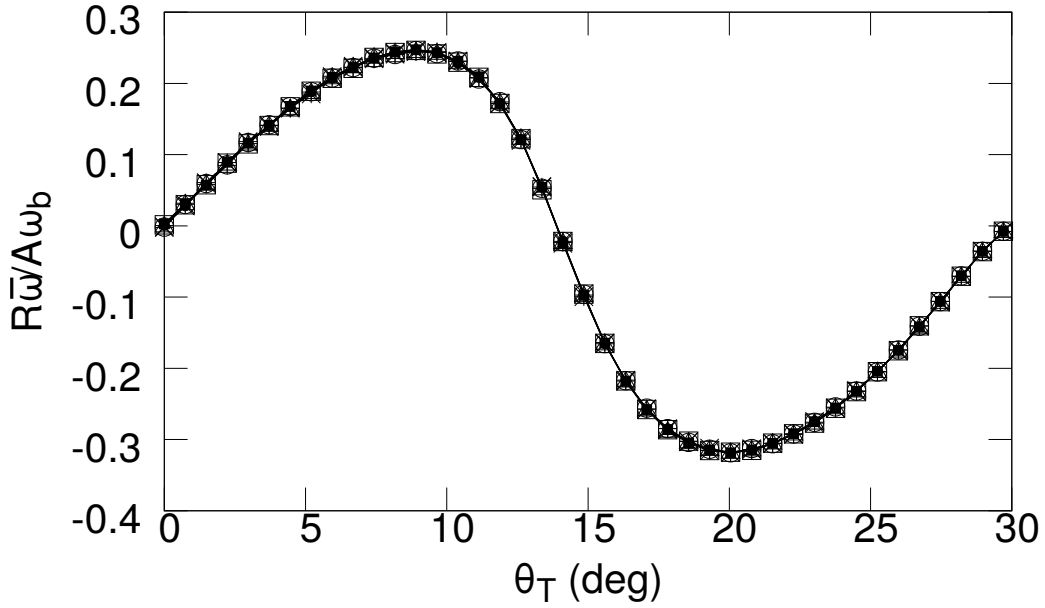

Figure 6.4: Event-driven numerical results for the rotational velocity of a disk bouncing in a wedge. The figure shows how curves with different values of Γ and ω_b collapse for the scaled variable $R\bar{\omega}/A\omega_b$, where R is the radius of the disk. We have used the nine possible combinations of the values $\Gamma = 1, 10, 100$ and $\omega_b = 1, 10, 100$. Results are undistinguishable from each other, because the ED mapping is explicitely scale-invariant. Other simulation parameters are $\mu = 0.1$, $e_n = 0.9$, $\theta_W = 2\pi/3, \kappa = k_t/k_n = 0.773$.

Scaling with bottom velocity

Figure 6.4 shows how the rescaled rotational velocity $\bar{\omega}/A\omega_b$, obtained with ED simulations, depends on the tilt θ_T, for a combination of different sets of amplitudes of vibration A and vibration frequencies ω_b. What we actually did was to run simulations for several combinations of dimensionless acceleration $\Gamma = A\omega_b^2/g = 1, 10, 100$ and $\omega_b = 1, 10, 100$ 1/s. The gravitational acceleration was in all cases $g = 9.81m/s^2$.
Clearly, the rotational velocity of the disk scales linearly with the maximum velocity of the bottom $A\omega_b$, as argued in Section 6.3.2. This scaling depends on the fact that the wedge geometry is scale free, i.e. it does not change under rescaling of the coordinates. This would not be true for a three-disk setup, as the curvature of the supporting disks is not scale-invariant. In this case, dynamical properties would only be expected to scale with v_b in the limit of small intensity excitation, when only the neighborhood of vertex of lowest potential energy is explored by the bouncing disk.

6.3.3 Equivalence of molecular dynamics and event driven simulation results.

By integrating the equations of motion of the system, Molecular Dynamics (MD) simulations attempt to follow the dynamical behavior of a physical system as closely as the available force model allows. In Event-Driven (ED) simulations, collisions are assumed instantaneous, and their effect is described by collision rules that map velocities before a collision to their values after the collision. Positions are assumed constant during a collision, and gravity is assumed to be negligible compared to inter-particle forces.
Our isolation of two relevant scales in Section 6.3.2 is clearly a simplification that only holds in the limit in which event driven simulations are valid: when the contact-time t_{col}, which measures the typical duration of a collision, is negligible with respect to the typical time t_{flight} between collisions. It is expected that, in this limit, the assumptions behind the ED method are valid, and ED simulation results coincide with those from MD. In Figure 6.5 we show the rotational velocity of the frictional disk on the wedge, for different parameters for both MD and ED simulations. We can see that, when the adimensional acceleration $\Gamma > 1$, these two methods produce results that scale with $v_b^{max} = A\omega_b$, and

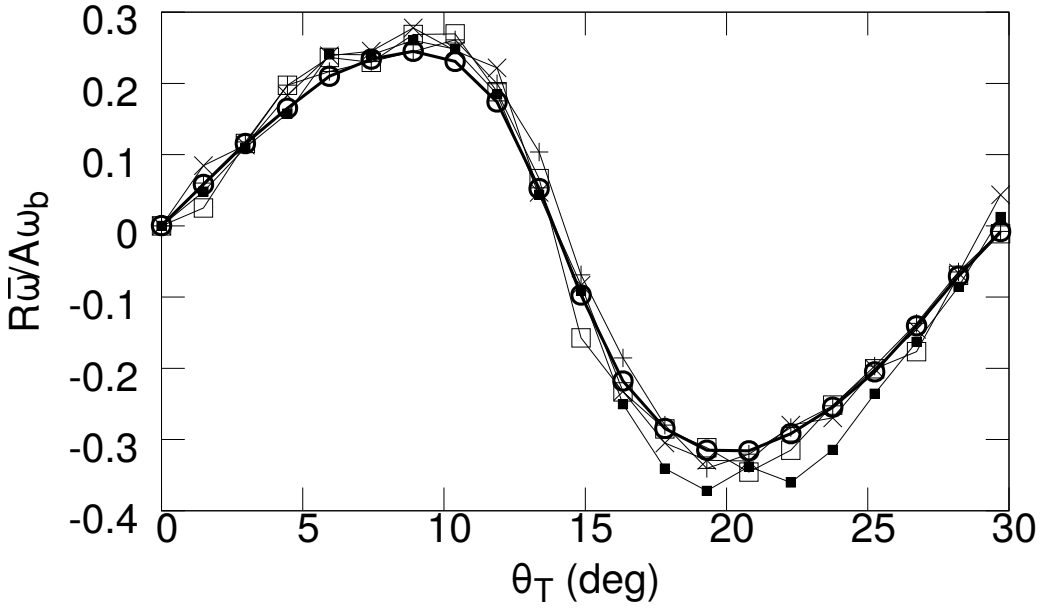

Figure 6.5: Scaled rotational velocity from MD and ED simulations compared. It can be seen that both simulation schemes agree very well. Only one curve for ED is shown (thick line, open circles) since all ED simulations are scale invariant by construction (see Section 6.3.2 and Fig. 6.4). MD curves are plotted for $\Gamma = 1.2$ (plusses), $\Gamma = 1.5$ (crosses), $\Gamma = 2.0$ (filled squares), $\Gamma = 3.0$ (empty squares). Simulation parameters are $\theta_W = 2\pi/3$, $k_n = 4.5e6N/m$, $\kappa = k_t/k_n = 0.773$, $R = 0.02m$, $e_n = 0.9$, $\mu = 0.1$, $m = 4.5g$.

are indistinguishable from each other within numerical error. While MD simulations are very time-consuming for these rotational billiards (because the time-step for integration has to be a small fraction of the, already small, collision time) ED has the advantage of speeding up simulations by orders of magnitude. Therefore, in the remaining sections, we only discuss results obtained with ED simulation.

6.3.4 Numerical results from event-driven simulations

Influence of the friction coefficient μ

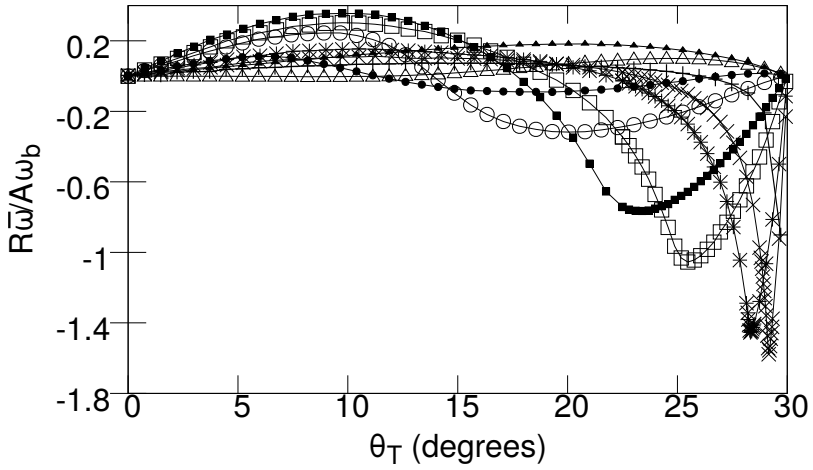

Figure 6.6: Numerical results from event-driven simulations for the scaled rotational velocity of the disk for different values of the friction coefficient μ. Values shown are $\mu = 0.001$ (pluses), $\mu = 0.005$ (crosses), $\mu = 0.01$ (asterisks), $\mu = 0.03$ (empty squares), $\mu = 0.05$ (filled squares), $\mu = 0.1$ (empty circles), $\mu = 0.15$ (filled circles), $\mu = 0.30$ (empty triangles) and $\mu = 1.0$ (filled triangles). Other simulation parameters are $\theta_W = 120$, $e_n = 0.9$, $\kappa = k_t/k_n = 0.773$

The friction coefficient μ determines how the tangential coefficient of restitution e_t behaves, and, through it, directly influences the rotational dynamics of the billiard. For very small values of μ, the disk slides during the entire contact, and the tangential coefficient of restitution e_t (See the full-sliding approximation (4.75)) only depends on μ and not on the elastic stiffness k_t. For moderate values of μ, the disk alternates between stick and slip

several times during the collision. In this regime, e_t depends on both μ and other material properties such as the normal and tangential stiffnesses, and can only be evaluated numerically.

Figure 6.6 plots the scaled tangential velocity $R\bar{\omega}/A\omega_b$ (R is disk radius) against tilt, for different values of μ. As μ increases, the point where $\bar{\omega}$ crosses zero moves to the left, up to $\mu = 0.1$, then we enter the regime when sliding no longer dominates the collision and $\bar{\omega}$ stays positive for all tilts. The limit of small frictional coefficient μ is somewhat surprising, as there is an increase in rotational velocity when the tilt approaches the critical tilt (when one of the walls becomes horizontal – 30 degrees in this case). The observable peak in angular velocity vs tilt θ_t moves towards the critical tilt when $\mu \to 0$. The height of this peak saturates to a parameter-dependent value, but the very existence of this peak indicates that there is a regime of large rotational velocity for small friction and when one of the walls of the wedge lies almost flat. We do not at present have a clear understanding of the reason for this behavior.

Effect of the wedge aperture θ_W

Figure 6.7 shows $R\bar{\omega}/A\omega_b$ versus relative tilt angle θ_T/θ_0, for several values of the wedge aperture θ_W. As expected, there is no rotation for a flat wedge (See the case of $\theta_W = 179$ degrees). Rotation seems to be strongly suppressed for wedge angles in the neighborhood of $\theta_W = 90$ degrees.

Effect of viscous dissipation

The normal restitution coefficient $e_n < 1$ quantifies the importance of viscous dissipation in collisions. Appart from viscosity, these billiards also dissipate energy through Coulomb friction. Therefore, viscous friction is an additional dissipation mechanism on top of friction. Figure 6.8 shows the scaled rotational velocity for different values of the restitution coefficient e_n, which depends directly on the amount of viscous dissipation. As expected, smaller values of e_n (larger viscosity of the disk) give rise to lower rotational velocities. We attempted to scale these results using a simple power of the restitution coefficient e_n but found that this procedure did not produce an acceptable scaling. This suggests that, when

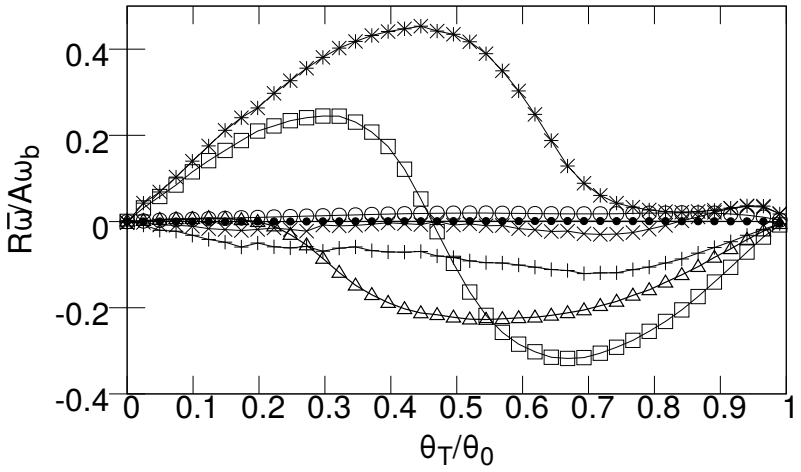

Figure 6.7: Numerical results from ED simulations for the scaled rotational velocity of the disk for different values of the wedge aperture θ_W versus the relative tilt θ_T/θ_0, where θ_0 is the critical tilt (such that one of the wedge walls becomes horizontal). Shown are $\theta_W = 90$ (plusses), $\theta_W = 91$ (crosses), $\theta_W = 100$ (asterisks), $\theta_W = 120$ (empty squares), $\theta_W = 140$ (triangles), $\theta_W = 160$ (open circles) and $\theta_W = 179$ (closed circles). Other simulation parameters are $\mu = 0.1$, $e_n = 0.9$, $\kappa = k_t/k_n = 0.773$

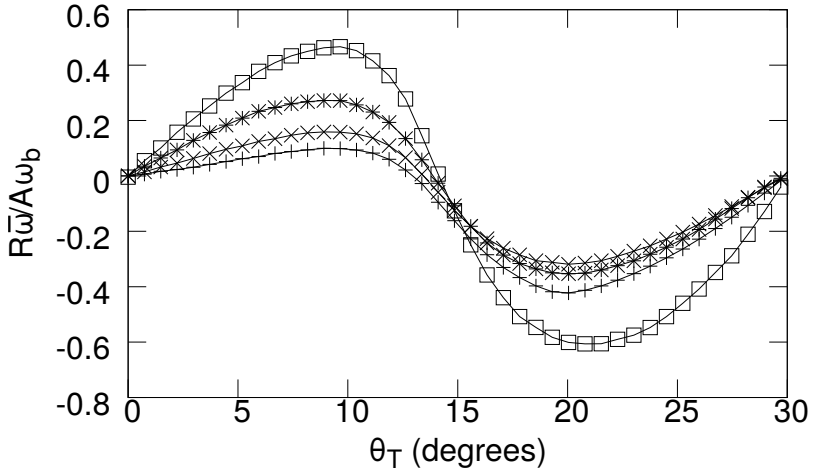

Figure 6.8: Numerical results from event-driven simulations for the scaled rotational velocity of the disk for different values of the normal coefficient of restitution e_n. Values shown are $e_n = 0.5$ (plusses), $e_n = 0.7$ (crosses), $e_n = 0.9$ (asterisks) and $e_n = 1.0$ (empty squares). Other simulation parameters are $\theta_W = 120$, $\mu = 0.1$, $\kappa = k_t/k_n = 0.773$.

the tilt is varied, the relative importance of viscous versus fritctional dissipation changes, at least for the parameter set used in these simulations.

Effect of the elastic ratio κ

The elastic ratio $\kappa = k_t/k_n$ does not appear in the ED mapping equations as a parameter, but its influence is important nevertheless, since it determines the functional form of the tangential restitution coefficient $e_t(u_t/u_n)$. Figure 4.5 shows how $e_t(u_t/u_n)$ behaves, for different values of κ. For small κ, i.e. when the skin is "soft", tangential forces during collisions remain weak. The tangential velocity is practically unaffected during a collision in this case, therefore e_t is close to one (thick solid line, $\kappa = 0.01$ in Fig. 4.5) for all incoming velocities. As κ is increased (dashed, dotted, then dot-dashed lines in Fig. 4.5), sliding starts to appear at large tangential velocities, and e_t follows the full-sliding approximation (4.75) closely for large u_t/u_n (thin solid line in Fig. 4.5). At smaller values of u_t/u_n, however, e_t shows increasingly rapid oscillatory behavior around zero as κ increases. This

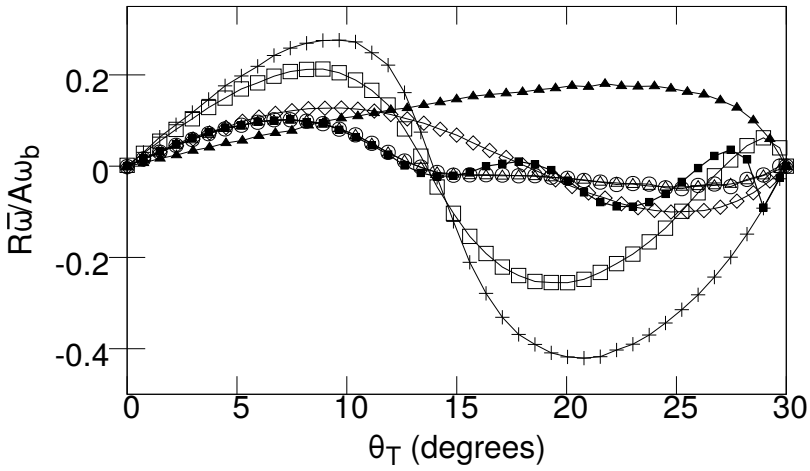

Figure 6.9: Scaled rotational velocity of the disk for different values of the stiffness ratio $\kappa = k_t/k_n$. Shown are $\kappa = 0.01$ (full triangles), $\kappa = 0.1$ (rhombuses), $\kappa = 1$ (empty squares), $\kappa = 10$ (full squares) and $\kappa = 100$ (circles). Results obtained by using the approximation $e_t = \max(0, 1-3\mu(1+e_n)\left|\frac{u_n}{u_t}\right|)$, which is valid in the $\kappa \to \infty$ limit, are shown using empty triangles. Other simulation parameters are $\theta_W = 120$, $\mu = 0.1$, $e_n = 0.9$.

depends on the fact that the rotational dynamics becomes complex, with many periods of slipping and sticking, therefore the outgoing tangential velocity can have any sign, and is much smaller than the incoming velocity, because of strong dissipation. In the limit $\kappa \to \infty$, the oscillatory behavior in the region of small u_t/u_n averages to zero. In this limit, the restitution coefficient can be well approximated by (4.75) whenever this gives a positive result, and zero otherwise, i.e $e_t = \max(0, 1 - 3\mu(1 + e_n)\left|\frac{u_n}{u_t}\right|)$.
Fig. 6.9 shows the scaled average rotation velocity of the disk in a wedge, for several values of κ. No simple tendency is observable in those data as a function of κ, again suggesting that the relative roles of viscous and frictional dissipation may vary strongly as a function of tilt θ_T. The above mentioned approximation for the case of large κ (empty triangles), is seen to be almost indistinguishable from results with $\kappa = 100$ (circles).

7 Conclusions

We study a novel self-organized rotational state in gently vibrated frictional disk-packings. Our investigations are experimental, numerical and analytic. We are able to extract meaningful predictions from our models, which are subsequently verified by numerical simulation.

The core result of this thesis is the experimental characterization of spontaneous rotation in disk packings done in Section 3.1. Via repeated experimentation, we have been able to carry a significant statistical analysis of the amount of rotation in a packing, measured using the mean squared rotational velocity $\langle\bar{\omega}^2\rangle$. We have found that the evolution of $\langle\bar{\omega}^2\rangle$ with vibration intensity (measured by Γ) follows two power laws, each valid in a different range of vibration amplitudes Γ. For low vibration amplitudes ($\Gamma \lessapprox 1$), the scaling is of the form $\langle\bar{\omega}^2\rangle \propto \Gamma^4$. For $\Gamma > 1$, the scaling becomes linear. The threshold $\Gamma = 1$ is significant, since at this amplitude the bottom wall overcomes the gravitational acceleration and the disks at the bottom of the packing start to bounce.

We also measured the velocity fluctuations in a packing using two related but independently calculated quantities, the correlation coefficient $\rho^2_{\theta,t}$ and the adjusted deviation σ_a. When fluctuations dominate and the disks do not rotate, these quantities take the values $\rho^2_{\theta,t} = 0$ and $\sigma_a = 1$. On the other hand, when fluctuations vanish and disks rotate with constant velocity, they take values $\rho^2_{\theta,t} = 1$ and $\sigma_a = 0$. From a statistical analysis on $\rho^2_{\theta,t}$ an σ, we were able to determine that not all disks are rotating for vibration amplitudes $\Gamma < 1$. As Γ increases from zero to one, the fraction of rotating disks in the packing increases, reaching a maximum at $\Gamma = 1$. Beyond $\Gamma = 1$, the majority of the disks in the packing keeps rotating, but velocity fluctuations increase with Γ. This difference in the fraction of rotating disks is likely the origin of the scaling transition at $\Gamma = 1$. All observations reported for experimental packings were successfully reproduced numerically,

validating simulations as a powerful alternative to study rotation in packings in a controlled computational environment.

We have implemented two different algorithms to simulate disk packings: Molecular Dynamics and Event Driven Simulations. Our molecular dynamics code, which is otherwise standard code for simulating elastic objects, implements a physically realistic representation of frictional forces. This, we believe, is at the core of our ability to successfully describe this phenomenon numerically. Our code assumes that each disk has an elastic skin, the deformations of which are responsible for tangential forces. Although the elastic skin idea has been already used in previous work, our approach further builds on it by calculating skin deformations directly from the disks' angular and translational coordinates, instead as from integration of tangential displacements, as done previously. The event-driven code assumes instantaneous collisions, but takes care to calculate how the tangential velocities change during a collision by solving an analytic model that takes into account the elastic skin. A key element in the implementation of the event-driven algorithm is the development of what we called the Fixed-Bottom-Random-Phase-Approximation (FBRPA) described in Section 2.3.3. The FBRPA allows the event-driven simulations to take place with fixed walls, while still preserving the correct velocity distribution for collisions. We believe that the FBRPA can find applications outside the scope of this work, for example, in the study of bouncing ball dynamics.

In an attempt to simplify the analysis, we also studied a basic-unit setup which consists of three disks, or, alternatively, of one disk on a wedge. The upper disk is supported by two contacts with the two lower ones, which are in turn subject to vibration. Motivated by the scaling transition for rotation in disk packings, we studied this simple setup in two regimes: in a regime of low amplitude of vibration, and in a regime of high amplitude of vibration. In both regimes, the rotational phenomenon is clearly observed whenever the whole set is tilted, so that the symmetry between contacts around the direction of gravity is broken.

An analytically description of this simple 3-disk setup is proposed in Chapter 4. Under certain simplifying assumptions, and under the condition that contacts between disks never break, the dynamics of the upper disk can be understood in terms of only two variables: its angular departure $\delta\theta$ from equilibrium, and the loading state of the elastic skin, measured

by its "stretch" Θ. The two-dimensional phase-space defined by these two variables is depicted in Figure 4.3, where the polyhedral figure indicates the location of the limits dictated by the Amonton condition on tangential forces. This figure delimits the non-sliding, or elastic, part of the phase space. If the linear accelerations of the disk's center of mass are neglected, this figure is fixed in time, and the model is analytically solvable.

Therefore, by envisaging the main effect of external forcing as subjecting the disk's angular variable $\delta\theta$ to a very slow oscillating torque, we were able to develop an exact expression that predicts the mean rotational velocity $\bar{\omega}$ as a function of the torque amplitude $\mathcal{T}_e$ (equation (5.9)). The basic idea is that the disk accumulates angular drift whenever its variables $\{\delta\theta, \Theta\}$ are located at the points indicated as S_1 and S_2 in Figure 4.3. For positive (counter-clockwise) tilt, the magnitude of the saturated friction force, given by Amonton's condition is smaller at S_2 than at S_1. Thus, less torque is required to reach point S_2 than to reach S_1. According to this picture, depending on the excitation intensity, the system may slide only at S_2, a regime we call unidirectional sliding, or at both S_2 and S_1, a regime called bidirectional sliding. The sliding regime is perfectly determined by the tilt θ_T and the torque amplitude A_e, a phase diagram is given in Figure 5.1. Independently of the sliding regime, time spent sliding at S_2 is always larger than time spent at S_1. This simple picture, in which linear accelerations are neglected, predicts a monotonically increasing dependence of the average rotational velocity $\bar{\omega}$ on the excitation amplitude $\mathcal{T}_e$.

There is a large degree of similarity between the case of external forcing in the 3-disk system and the elastic-perfectly plastic oscillator (EPO) [51–54]. As in the 3-disk system, the EPO's displacement is constrained by frictional Amonton limits and the force is directly applied to the oscillating element. The EPO can be considered as a simplified version of the 3-disk system under external forcing, where there is only a single sliding contact (instead of two) and sliding limits are constant. Even after this simplification, the direction of the drift is predicted in the same way in both systems. The drift is always towards the friction limit that is easier to reach, i.e., the one with smaller magnitude.

Once the case of externally forced 3-disk system was understood, we directed our efforts to the more physically relevant case of randomly vibrating the supporting disks. In disk packings, the only external force disks experience is gravity. A disk rotation is caused by its interaction with other disks in the packing. In this sense, exciting the upper disk by

randomly vibrating its supports, instead of imposing an external torque, is closer to what actually happens inside a packing.

For the 3-disk system with vibrating supports, the assumption that the linear accelerations of the disk are negligible is incorrect. This hypothesis can be tested through numerical simulations and, in fact, it turns out that the system is always out of equilibrium and experiences very fast oscillations involving all degrees of freedom. When the linear accelerations of the disk are not negligible, the geometrical figure (Figure 4.3) that delimits the non-sliding part of the phase space, that remained fixed in the case of external forcing, changes size and shape in time. Developing a model based on this randomly fluctuating region proved to be too difficult. However, building on the understanding gained from the analysis of the 3-disk system under external forcing, we were able to develop a simplified model that captures the behavior of the system under random vibration.

Results of numerical simulations for the 3-disk system with vibrating supports, which we present in Section 5.3.2, show that the rotational velocity of one disk decreases monotonically with increasing external excitation, and changes non-monotonically with tilt. A qualitative understanding of the mechanism behind rotation was obtained in Section 5.3.3. A key insight gained from the discussion is that the rotational velocity of the upper disk depends strongly on the particular characteristics of the way the system is excited, in particular depending on how the phase space of allowed contact forces is explored by the system. We have observed disks rotating without breaking contacts in disk packings excited with vibration amplitudes $\Gamma < 1$. These disks seem to behave similarly to the upper disk of the 3-disk system with lasting contacts, but these observations need to be further validated in a future work.

The analytic description based on the variables $\delta\theta$ and Θ is unsuitable to perform the analysis when the restriction of non-breaking contacts is lifted. Whenever a contact is broken, the polygon delimiting the elastic region in Figure 4.3 collapses to a single point and all memory of the deformation of the elastic skin is lost. Furthermore, the disk can accumulate rotation while detached from the supports. We can, however, take the limit of high vibration amplitudes. In this limit the time disks remain in contact is negligible, and all rotation is accumulated during flight.

In Chapter 6, we apply this limit to the case of a single disk bouncing repeatedly of

a wedge. With the help of the expression for the coefficients of restitution, derived in Section 4.5, we constructed a dynamical map that calculates the position and the velocities of the disk at the beginning of a collision from the values of the position and the velocities at the previous collision. By re-scaling the mapping, we showed that the rotational velocity scales linearly with the amplitude of vibration, a result that is validated using MD and ED simulations. The coincidence between MD results and ED results (within a random phase approximation for the bottom vibration) for different kinds of wedge motion, strongly suggests that this phenomenon is largely independent from the type of bottom excitation used, depending only, instead, on the mean relative velocity at the collision. In other words, the spontaneous rotation observed does not depend on a synchronization between the bottom and the bouncing disk, but occurs even for a randomly shaken wedge. Detailed numerical simulation using MD and ED algorithms allowed us to quantify the rotational behavior of the bouncing disk under various circumstances, revealing very rich dynamics as the parameters are varied. We expect that the behavior of disks in a packing, for amplitudes of vibration $\Gamma > 1$, falls within the approximation of instantaneous collisions. In a future work we intend to adapt the mapping equations to the case of a random polygonal billiard. The idea is that the walls of the billiard would act as the neighbors of a disk in a packing. We hope that by studying this map we can understand why the mean squared rotational velocity scales linearly in disk packings when $\Gamma > 1$.

In this thesis we have reported and characterized the appearance of rotation in disk packings. We have also shown that a simple mechanism is indeed responsible for spontaneous rotation. The lack of right-left asymmetry in the contacts that support a given disk, is enough to induce rotations under certain conditions. Furthermore, we were able to obtain analytic predictions for a set of simple cases, and validate these predictions against numerical simulations. Alternatively, this can be seen as a double-sided validation, since in this process it becomes clear that the rotational effect observed for large packings is not an artifact of the simulation algorithm. We have also stated possible directions for future work to further the understanding of this phenomenon.

Bibliography

[1] Igor S. Aranson and Lev S. Tsimring. Patterns and collective behavior in granular media: Theoretical concepts. Reviews of Modern Physics, 78(2):641–692, June 2006.

[2] Arshad Kudrolli. Size separation in vibrated granular matter. Reports on Progress in Physics, 67(3):209, 2004.

[3] J. S. Olafsen and J. S. Urbach. Clustering, Order, and Collapse in a Driven Granular Monolayer. Physical Review Letters, 81(20):4369–4372, November 1998.

[4] I. Goldhirsch and G. Zanetti. Clustering instability in dissipative gases. Physical Review Letters, 70(11):1619–1622, March 1993.

[5] Francisco Melo, Paul Umbanhowar, and Harry L. Swinney. Transition to parametric wave patterns in a vertically oscillated granular layer. Physical Review Letters, 72(1):172–175, January 1994.

[6] Francisco Melo, Paul B. Umbanhowar, and Harry L. Swinney. Hexagons, Kinks, and Disorder in Oscillated Granular Layers. Physical Review Letters, 75(21):3838–3841, November 1995.

[7] C. Bizon, M. D. Shattuck, J. B. Swift, W. D. McCormick, and Harry L. Swinney. Patterns in 3d Vertically Oscillated Granular Layers: Simulation and Experiment. Physical Review Letters, 80(1):57–60, January 1998.

[8] C. Bizon, M. D. Shattuck, John R. de Bruyn, J. B. Swift, W. D. McCormick, and Harry L. Swinney. Convection and Diffusion in Patterns in Oscillated Granular Media. Journal of Statistical Physics, 93(3-4):449–465, November 1998.

[9] Paul B. Umbanhowar, Francisco Melo, Harry L. Swinney, and others. Localized excitations in a vertically vibrated granular layer. Nature, 382(6594):793–796, 1996.

[10] A. P. J. Breu, H.-M. Ensner, C. A. Kruelle, and I. Rehberg. Reversing the Brazil-Nut Effect: Competition between Percolation and Condensation. Physical Review Letters, 90(1):014302, January 2003.

[11] Anthony Rosato, Katherine J. Strandburg, Friedrich Prinz, and Robert H. Swendsen. Why the Brazil nuts are on top: Size segregation of particulate matter by shaking. Physical Review Letters, 58(10):1038–1040, March 1987.

[12] Daniel C. Hong, Paul V. Quinn, and Stefan Luding. Reverse Brazil Nut Problem: Competition between Percolation and Condensation. Physical Review Letters, 86(15):3423–3426, April 2001.

[13] James B. Knight, E. E. Ehrichs, Vadim Yu. Kuperman, Janna K. Flint, Heinrich M. Jaeger, and Sidney R. Nagel. Experimental study of granular convection. Physical Review E, 54(5):5726–5738, November 1996.

[14] E. L. Grossman. Effects of container geometry on granular convection. Physical Review E, 56(3):3290–3300, September 1997.

[15] James B. Knight, H. M. Jaeger, and Sidney R. Nagel. Vibration-induced size separation in granular media: The convection connection. Physical Review Letters, 70(24):3728–3731, June 1993.

[16] Troy Shinbrot. Granular chaos and mixing: Whirled in a grain of sand. Chaos: An Interdisciplinary Journal of Nonlinear Science, 25(9):097622, September 2015.

[17] Thorsten Pöschel and Thomas Schwager. Computational Granular Dynamics. Springer-Verlag, Berlin/Heidelberg, 2005.

[18] G. William Baxter and R. P. Behringer. Cellular automata models for the flow of granular materials. Physica D: Nonlinear Phenomena, 51(1–3):465–471, August 1991.

[19] M. Jean. The non-smooth contact dynamics method. Computer Methods in Applied Mechanics and Engineering, 177(3–4):235–257, July 1999.

[20] J. Shäfer, S. Dippel, and D. E. Wolf. Force Schemes in Simulations of Granular Materials. Journal de Physique I, 6(1):16, 1996.

[21] H. Kruggel-Emden, E. Simsek, S. Rickelt, S. Wirtz, and V. Scherer. Review and extension of normal force models for the Discrete Element Method. Powder Technology, 171(3):157–173, February 2007.

[22] P. A. Cundall and O. D. L. Strack. A discrete numerical model for granular assemblies. Géotechnique, 29(1):47–65, March 1979.

[23] M. Paulick, M. Morgeneyer, and A. Kwade. Review on the influence of elastic particle properties on DEM simulation results. Powder Technology, 283:66–76, October 2015.

[24] Boris D Lubachevsky. How to simulate billiards and similar systems. Journal of Computational Physics, 94(2):255–283, June 1991. arxiv:http://arxiv.org/abs/cond-mat/0503627.

[25] Sean McNamara and W. R. Young. Inelastic collapse in two dimensions. Physical Review E, 50(1):R28–R31, July 1994.

[26] G. G. Peraza-Mues, Osvaldo Carvente, and Cristian F. Moukarzel. Rotation in a gravitational billiard. International Journal of Modern Physics C, page 1750021, September 2016.

[27] Y. T. Feng, K. Han, and D. R. J. Owen. Filling domains with disks: an advancing front approach. International Journal for Numerical Methods in Engineering, 56(5):699–713, February 2003.

[28] Daan Frenkel and Berend Smit. Understanding Molecular Simulation: From Algorithms to Applications. Academic Press, edición: 2 edition, October 2001.

[29] C. William Gear. The automatic integration of ordinary differential equations. Communications of the ACM, 14(3):176–179, 1971.

[30] David Goldberg. What Every Computer Scientist Should Know About Floating-point Arithmetic. ACM Comput. Surv., 23(1):5–48, March 1991.

[31] Johannes Schindelin, Ignacio Arganda-Carreras, Erwin Frise, Verena Kaynig, Mark Longair, Tobias Pietzsch, Stephan Preibisch, Curtis Rueden, Stephan Saalfeld, Benjamin Schmid, Jean-Yves Tinevez, Daniel James White, Volker Hartenstein, Kevin Eliceiri, Pavel Tomancak, and Albert Cardona. Fiji: an open-source platform for biological-image analysis. Nature Methods, 9(7):676–682, July 2012.

[32] N. S. Altman. An Introduction to Kernel and Nearest-Neighbor Nonparametric Regression. The American Statistician, 46(3):175–185, August 1992.

[33] Peter Eshuis, Ko van der Weele, Devaraj van der Meer, Robert Bos, and Detlef Lohse. Phase diagram of vertically shaken granular matter. Physics of Fluids, 19(12):123301, December 2007.

[34] J. M. Luck and Anita Mehta. Bouncing ball with a finite restitution: Chattering, locking, and chaos. Physical Review E, 48(5):3988–3997, November 1993.

[35] M. Hubert, F. Ludewig, S. Dorbolo, and N. Vandewalle. Bouncing dynamics of a spring. Physica D: Nonlinear Phenomena, 272(Supplement C):1–7, April 2014.

[36] Gabriel Pérez. Numerical simulations in granular matter: The discharge of a 2d silo. Pramana, 70(6):989–1007, June 2008.

[37] Sean McNamara, Ramón García-Rojo, and Hans Herrmann. Indeterminacy and the onset of motion in a simple granular packing. Physical Review E, 72(2):021304, August 2005.

[38] Alberto Di Renzo and Francesco Paolo Di Maio. Comparison of contact-force models for the simulation of collisions in DEM-based granular flow codes. Chemical Engineering Science, 59(3):525–541, February 2004.

[39] H. Kruggel-Emden, S. Wirtz, and V. Scherer. A study on tangential force laws applicable to the discrete element method (DEM) for materials with viscoelastic or plastic behavior. Chemical Engineering Science, 63(6):1523–1541, March 2008.

[40] H. Kruggel-Emden, S. Wirtz, and V. Scherer. Applicable contact force models for the discrete element method: the single particle perspective. Journal of Pressure Vessel Technology, 131(2):024001, 2009.

[41] A. Z. Gorski and T. Srokowski. Chaotic and Regular Motion in Dissipative Gravitational Billiards. Acta Physica Polonica B, 37:2561, September 2006.

[42] Alexandre E. Hartl, Bruce N. Miller, and Andre P. Mazzoleni. Dynamics of a dissipative, inelastic gravitational billiard. Physical Review E, 87(3):032901, March 2013.

[43] Leonardo E. Silbert, Deniz Ertaş, Gary S. Grest, Thomas C. Halsey, and Dov Levine. Geometry of frictionless and frictional sphere packings. Physical Review E, 65(3):031304, 2002.

[44] Thomas Schwager and Thorsten Pöschel. Coefficient of restitution and linear–dashpot model revisited. Granular Matter, 9(6):465–469, October 2007.

[45] Volker Becker, Thomas Schwager, and Thorsten Pöschel. Coefficient of tangential restitution for the linear dashpot model. Physical Review E, 77(1):011304, January 2008.

[46] S. Chandrasekhar. Stochastic Problems in Physics and Astronomy. Reviews of Modern Physics, 15(1):1–89, January 1943.

[47] H. E. Lehtihet and B. N. Miller. Numerical study of a billiard in a gravitational field. Physica D: Nonlinear Phenomena, 21(1):93–104, August 1986.

[48] P. H. Richter, H.-J. Scholz, and A. Wittek. A breathing chaos. Nonlinearity, 3(1):45, 1990.

[49] V. Milner, J. L. Hanssen, W. C. Campbell, and M. G. Raizen. Optical Billiards for Atoms. Physical Review Letters, 86(8):1514–1517, February 2001.

[50] S. Feldt and J. S. Olafsen. Inelastic Gravitational Billiards. Physical Review Letters, 94(22):224102, June 2005.

[51] Dean Karnopp and Terry D. Scharton. Plastic Deformation in Random Vibration. The Journal of the Acoustical Society of America, 39(6):1154–1161, June 1966.

[52] R. L. Grossmayer. Elastic-plastic oscillators under random excitation. Journal of Sound and Vibration, 65(3):353–379, August 1979.

[53] Ove Ditlevsen and László Bognár. Plastic displacement distributions of the Gaussian white noise excited elasto-plastic oscillator. Probabilistic Engineering Mechanics, 8(3):209–231, January 1993.

[54] Robert Bouc and Djaffar Boussaa. Ratcheting response of elastic perfectly plastic oscillators under random load with non-zero mean. Comptes Rendus de l'Académie des Sciences - Series IIB - Mechanics-Physics-Astronomy, 326(8):475–482, August 1998.